

# New constraints on cosmological modified gravity theories from anisotropic three-point correlation functions of BOSS DR12 galaxies

Naonori S. Sugiyama<sup>1\*</sup>

<sup>1</sup> *National Astronomical Observatory of Japan, Mitaka, Tokyo 181-8588, Japan*

Daisuke Yamauchi<sup>2</sup>, Tsutomu Kobayashi<sup>3</sup>, Tomohiro Fujita<sup>4,5</sup>, Shun Arai<sup>6</sup>, and Shin’ichi Hirano<sup>7</sup>

<sup>2</sup> *Faculty of Engineering, Kanagawa University, Kanagawa, 221-8686, Japan*

<sup>3</sup> *Department of Physics, Rikkyo University, Toshima, Tokyo 171-8501, Japan*

<sup>4</sup> *Waseda Institute for Advanced Study, Shinjuku, Tokyo 169-8050, Japan*

<sup>5</sup> *Research Center for the Early Universe, The University of Tokyo, Bunkyo, Tokyo 113-0033, Japan*

<sup>6</sup> *Kobayashi-Maskawa Institute, Nagoya University, Nagoya 464-8602, Japan*

<sup>7</sup> *Department of Physics, Tokyo Institute of Technology, 2-12-1 Ookayama, Meguro-ku, Tokyo 152-8551, Japan*

Shun Saito<sup>8,9</sup>, Florian Beutler<sup>10</sup>, and Hee-Jong Seo<sup>11,12,13</sup>

<sup>8</sup> *Institute for Multi-messenger Astrophysics and Cosmology, Department of Physics, Missouri University of Science and Technology, 1315 N. Pine St., Rolla MO 65409, USA*

<sup>9</sup> *Kavli Institute for the Physics and Mathematics of the Universe (WPI),*

*Todai Institutes for Advanced Study, The University of Tokyo, Chiba 277-8582, Japan*

<sup>10</sup> *Institute for Astronomy, University of Edinburgh, Royal Observatory, Blackford Hill, Edinburgh EH9 3HJ, UK*

<sup>11</sup> *Department of Physics and Astronomy, Ohio University, Clippinger Labs, Athens, OH 45701, USA*

<sup>12</sup> *Physics Division, Lawrence Berkeley National Laboratory, 1 Cyclotron Road, Berkeley, CA 94720, USA*

<sup>13</sup> *Berkeley Center for Cosmological Physics, Department of Physics, University of California, Berkeley, CA 94720, USA*

## ABSTRACT

We report a new test of modified gravity theories using the large-scale structure of the Universe. This paper is the first attempt to (1) apply a joint analysis of the anisotropic components of galaxy two- and three-point correlation functions (2 and 3PCFs) to actual galaxy data and (2) constrain the nonlinear effects of degenerate higher-order scalar-tensor (DHOST) theories on cosmological scales. Applying this analysis to the Baryon Oscillation Spectroscopic Survey (BOSS) data release 12, we obtain the lower bounds of  $-1.655 < \xi_t$  and  $-0.504 < \xi_s$  at the 95% confidence level on the parameters characterising the time evolution of the tidal and shift terms of the second-order velocity field. These constraints are consistent with GR predictions of  $\xi_t = 15/1144$  and  $\xi_s = 0$ . Moreover, they represent a 35-fold and 20-fold improvement, respectively, over the joint analysis with only the isotropic 3PCF. We ensure the validity of our results by investigating various quantities, including theoretical models of the 3PCF, window function corrections, cumulative S/N, Fisher matrices, and statistical scattering effects of mock simulation data. We also find statistically significant discrepancies between the BOSS data and the Patchy mocks for the 3PCF measurement. Finally, we package all of our 3PCF analysis codes under the name HITOMI and make them publicly available so that readers can reproduce all the results of this paper and easily apply them to ongoing future galaxy surveys.

**Key words:** cosmology: large-scale structure of Universe – cosmology: dark matter – cosmology: observations – cosmology: theory

## 1 INTRODUCTION

### 1.1 Outline and summary

This paper presents a comprehensive study of the joint analysis of galaxy two- and three-point correlation functions (2 and 3PCFs) with isotropic and anisotropic components to constrain the non-linear effects of modified gravity theories on a cosmological scale. Section 1

outlines the theoretical development and the present constraints for scalar-tensor theories. We also outline the development of the measurement and analysis of the three-point correlation function of galaxies. We organize this paper such that readers unfamiliar with both or one of the two areas follow the recent developments and understand how they fit together.

Readers interested in the theoretical aspects may read Sections 2, 3, and 7. Section 2 reviews the non-linear evolution of the large-scale structure of the Universe in scalar-tensor theories. Section 3

\* E-mail: nao.s.sugiyama@gmail.com

presents detailed calculations of the theoretical model of the 3PCF and, in particular, investigates the dependence of the parameters that characterise the effect of scalar-tensor theories on the 3PCF model. Finally, Section 7 discusses the extent to which the 3PCF contains information on the non-linear effects of scalar-tensor theories through Fisher analysis.

Readers interested in the analysis method of the 3PCF may read Sections 4, 5, 6, and 8. Section 4 reviews how to measure the 3PCF from galaxy data and examines the effect of the window function on the measured 3PCFs. Section 5 presents the results of the 2PCF and 3PCF covariance matrices computed from mock simulations. Section 6 describes the setup for the data analysis in this paper. Finally, Section 8 discusses in detail whether the 3PCFs measured from the galaxy data in this paper can be fitted using the corresponding theoretical model in terms of  $p$ -values.

For readers familiar with the two areas in the literature and interested in the final results, we suggest they jump directly to Section 9. The novel aspect of this paper is to focus on observationally constraining the second-order velocity field, which is a key to seeking a deviation from GR in scalar-tensor theories. We also show that the second-order velocity field imprints a unique signature in the anisotropic 3PCF on large scales. Following Yamauchi & Sugiyama (2022) and Section 3.4, we then parameterise the effects of scalar-tensor theories in the time evolution of the shift and tidal terms of the second-order velocity field using parameters  $\xi_s$  and  $\xi_t$  defined in Eq. (3.27). Constraining these parameters using Baryon Oscillation Spectroscopic Survey Data Release 12 galaxies (Eisenstein et al. 2011; Bolton et al. 2012; Dawson et al. 2013; Alam et al. 2015), we obtain the following lower bounds given in Eqs. (9.8) and (9.10):

$$-1.655 < \xi_t \text{ and } -0.504 < \xi_s \text{ (95\%CL)}.$$

Since  $\xi_t = 15/1144$  and  $\xi_s = 0$  in GR, these results are consistent with GR. Finally, we summarise the final results and the various findings leading up to them in Section 10, which concludes this paper.

We package all the code used to complete this paper under the name HITOMI<sup>1</sup> and make it publicly available. Appendix A summarises the structure and usage of HITOMI.

## 1.2 General motivation

The greatest mystery in current cosmology is the cause of the accelerated expansions that have presumably occurred twice in the cosmic expansion history: i.e., inflation and late-time acceleration.

Scalar-tensor theories, modified gravity theories that add a single scalar field degree of freedom to General Relativity (GR), have been actively studied as a promising candidate to explain these accelerated expansions (for reviews, see Langlois 2019; Kase & Tsujikawa 2019; Kobayashi 2019; Amendola et al. 2020; Frusciante & Perenon 2020)<sup>2</sup>.

The accelerated expansion in the very early Universe, called inflation (Starobinsky 1980; Guth 1981; Sato 1981; Linde 1982; Albrecht & Steinhardt 1982), is thought to be caused by a single scalar field in the simplest model, generating the seeds of the cosmic fluctuations currently observed. Furthermore, the statistical properties of these fluctuations are in excellent agreement with

current observations of the cosmic microwave background (CMB; Aghanim et al. 2020) and the large-scale structure (LSS; Alam et al. 2021a). On the other hand, the cosmological constant may explain the late-time accelerated expansion (Riess et al. 1998; Perlmutter et al. 1999). However, its smallness implies a serious fine-tuning problem in fundamental physics (Weinberg 1989; Martin 2012), and in order to avoid this problem, it is preferable to adopt a scalar field that varies with time.

In order to test scalar-tensor theories in the late-time Universe, it is crucial to follow the time evolution of the large-scale structure in detail. Examples of already completed galaxy surveys are the Baryon Oscillation Spectroscopic Survey (BOSS Eisenstein et al. 2011; Bolton et al. 2012; Dawson et al. 2013; Alam et al. 2015)<sup>3</sup> and the Extended BOSS (eBOSS; Dawson et al. 2016; Alam et al. 2021a)<sup>4</sup>. Furthermore, The next-generation galaxy surveys, such as the Dark Energy Spectroscopic Instrument (DESI; DESI Collaboration et al. 2016)<sup>5</sup>, Euclid (Laureijs et al. 2011)<sup>6</sup>, and the Subaru Prime Focus Spectrograph (PFS; Takada et al. 2014)<sup>7</sup>, will provide unprecedented accuracy in testing scalar-tensor theories.

## 1.3 DHOST theories and their constraints

In this paper, we pay particular attention to the behaviour in the late-time Universe of Degenerate Higher-Order Scalar-Tensor (DHOST) theory (for reviews, see Langlois 2019; Kobayashi 2019), which are a quite general theoretical framework of scalar-tensor theories that can evade the Ostrogradsky instability (Ostrogradsky 1850; Woodard 2015; Ganz & Noui 2020). Scalar-tensor theories have been developing rapidly over the last decade. In 2011, Deffayet et al. (2011); Kobayashi et al. (2011) rediscovered the most general theory with second-order equations of motion for metric tensor and scalar fields, Horndeski theories (Horndeski 1974). To go beyond Horndeski theories, Gleyzes et al. (2015a,b) found a class of healthy theories having higher-order field equations that reduce to a second-order system by combining different components (see also Zumalacárregui & García-Bellido 2014, for examples beyond Horndeski). This discovery results from a degeneracy between the kinetic terms of the scalar field and the metric. This class of theories has been extended to reach DHOST theories (Langlois & Noui 2016; Crisostomi et al. 2016; Ben Achour et al. 2016a,b; Langlois 2017; Langlois et al. 2020), encompassing Horndeski and Beyond Horndeski theories<sup>8</sup>. So far, DHOST theories have been constrained primarily by three observations<sup>9</sup>: gravitational waves (GW), celestial objects, and cosmological data that is the subject of this paper.

Since GW170817 was observed by LIGO and Virgo (Abbott et al. 2017a), the situation surrounding the observational constraints of modified gravity has changed dramatically. The simultaneous observation of GRB170817 (Abbott et al. 2017b), a Gamma

<sup>3</sup> [https://www.sdss3.org/science/boss\\_publications.php](https://www.sdss3.org/science/boss_publications.php)

<sup>4</sup> <https://www.sdss.org/surveys/eboss/>

<sup>5</sup> <http://desi.lbl.gov/>

<sup>6</sup> [www.euclid-ec.org](http://www.euclid-ec.org)

<sup>7</sup> <https://pfs.ipmu.jp/index.html>

<sup>8</sup> Hereafter, we do not distinguish between Beyond Horndeski theories and DHOST theories.

<sup>9</sup> As other probes of DHOST theories, for example, Babichev & Lehébel (2018) shows that the scalar field in DHOST theories can significantly modify the speed of sound in the atmosphere of the Earth; Beltran Jimenez et al. (2016); Dima & Vernizzi (2018) strongly constrain DHOST models using Hulse-Taylor pulsar observations; Saltas & Lopes (2019) proposes helioseismology as a precise way to test DHOST theories on astrophysical scales.

<sup>1</sup> <https://github.com/naonori/hitomi.git>

<sup>2</sup> For reviews of modified gravity theories, including other theories than scalar-tensor theories, see Nojiri & Odintsov 2011; Sebastiani et al. 2017; Nojiri et al. 2017; Cataneo & Rapetti 2018; Ishak 2019; Ferreira 2019; Baker et al. 2021; Arai et al. 2022.

Ray burst, confirmed that the speed of GWs matches the speed of electromagnetic waves with high accuracy, ruling out various scalar-tensor theories that change the speed of GWs at low redshifts (Lombriser & Taylor 2016; Lombriser & Lima 2017; Creminelli & Vernizzi 2017; Sakstein & Jain 2017; Ezquiaga & Zumalacárregui 2017; Baker et al. 2017; Langlois et al. 2018). Creminelli et al. (2018, 2019) pointed out that a subset of DHOST theories leads to the decay of gravitational waves, resulting in further tight constraints on DHOST theories. However, the theory of gravity considered in that paper, the class I DHOST theory (Langlois & Noui 2016; Crisostomi et al. 2016; Ben Achour et al. 2016b), still survives and can modify gravity in cosmology without pathological instability (de Rham & Matas 2016; Langlois et al. 2017; Amendola et al. 2018). Furthermore, de Rham & Melville (2018) showed that such cosmological scalar-tensor theories, which predict the speed of GWs to be different from the speed of light, break down on high energy scales ( $\sim 10^2$  Hz) seen in neutron star mergers, indicating that the constraints from GW observations may not necessarily apply to cosmological scales. Therefore, it is essential to test modified gravity theories independently at various energy scales, such as the GW and cosmological scales.

DHOST theories generally have characteristic non-linear effects that violate the Vainshtein screening mechanism inside any gravitational source (Kobayashi et al. 2015; Koyama & Sakstein 2015; Crisostomi & Koyama 2018; Langlois et al. 2018; Dima & Vernizzi 2018; Hirano et al. 2019b; Crisostomi et al. 2019). As an alternative to the cosmological constant, scalar-tensor theories must give an  $\mathcal{O}(1)$  modification from GR at cosmological scales, but at small scales, they must satisfy tests in weakly gravitational regions such as the solar system. The Vainshtein screening mechanism (for a review, Babichev & Deffayet 2013), universally found in scalar-tensor theories, is a typical mechanism that satisfies these requirements, suppressing scalar interactions and restoring standard gravity through non-linear effects. While Horndeski theories allow for a natural implementation of the Vainshtein mechanism (Kimura et al. 2012; Narikawa et al. 2013; Koyama 2016), DHOST theories partially violate it, allowing one to test DHOST theories by examining the internal structure of objects such as Newtonian stars (Saito et al. 2015; Sakstein 2015a,b; Jain et al. 2016; Sakstein et al. 2017a; Saltas et al. 2018; Saltas & Christensen-Dalsgaard 2022), Neutron stars (Babichev et al. 2016; Sakstein et al. 2017b), and galaxy clusters (Sakstein et al. 2016; Salzano et al. 2017). The Vainshtein radius, the maximum scale at which the Vainshtein mechanism works, is estimated to be  $\mathcal{O}(100)$  pc for the Sun and  $\mathcal{O}(1)$  Mpc for a galaxy cluster.

DHOST theories predict a characteristic gravitational non-linear effect on even cosmological scales exceeding tens of Mpc. That is, DHOST theories violate the consistency relation for LSS (Crisostomi et al. 2020; Lewandowski 2020) (see also Hirano et al. 2018). The LSS consistency relation (Peloso & Pietroni 2013; Kehagias & Riotto 2013; Creminelli et al. 2013) is an analogue of the consistency relation originally proposed for single-field inflation models (Maldacena 2003; Creminelli & Zaldarriaga 2004), which relates  $n$ -point statistics of cosmological fluctuations to  $(n-1)$ -point statistics in a non-perturbative matter. It is valid in the limit where the wavenumber of one of the  $n$ -points is hugely smaller than the others. This consistency relation is because the equations that the fluctuations obey are invariant under a Galilean transformation (Scoccimarro & Frieman 1996; Creminelli et al. 2013). In particular, in the so-called equal-time consistency relation, the Galilean transformation eliminates the large-scale flow of matter

and thus cancels all non-linear contributions when calculating the  $n$ -point statistics. This behavior is also known as infrared (IR) cancellation (Jain & Bertschinger 1996; Scoccimarro & Frieman 1996; Kehagias & Riotto 2013; Peloso & Pietroni 2013; Sugiyama & Futamase 2013; Sugiyama & Spergel 2014; Blas et al. 2013, 2016b; Lewandowski & Senatore 2017). On the other hand, the LSS consistency relation breaks down when considering multiple fluids (Tseliakhovich & Hirata 2010; Yoo et al. 2011; Bernardeau et al. 2012, 2013; Peloso & Pietroni 2014; Creminelli et al. 2014a; Lewandowski et al. 2015; Slepian & Eisenstein 2017) or primordial non-Gaussianities (Berezhiani & Houry 2014; Valageas et al. 2017; Esposito et al. 2019; Goldstein et al. 2022), or when the equivalence principle breaks (Creminelli et al. 2014b). DHOST theories have a structure similar to that of multiple fluids, and on large scales, the Galilean transformation cannot make the relative velocity between the scalar field and matter vanish (for details, see Crisostomi et al. 2020; Lewandowski 2020). As a result, DHOST theories violate the LSS consistency relation.

Our interest in this paper is to constrain DHOST theories on cosmological scales, i.e.,  $\mathcal{O}(10-100)$  Mpc scales. However, studies using cosmological data to constrain DHOST theories are still limited (Hirano et al. 2019a; Traykova et al. 2019; Peirone et al. 2019; Hiramatsu 2022). On the other hand, many papers on Horndeski theories have used cosmological data to constrain the model (Okada et al. 2013; Barreira et al. 2014; Bellini et al. 2016; Mueller et al. 2018; Kreisch & Komatsu 2018; Arai & Nishizawa 2018; Noller & Nicola 2020, 2019; Raveri 2020; Melville & Noller 2020; Perenon et al. 2019; Noller 2020). Therefore, exploring new cosmological methods for constraining DHOST theories is of great significance.

#### 1.4 Constraints on modified gravity theories using galaxy two-point statistics

The logarithmic growth rate function  $f$  of dark matter fluctuations, measured using redshift-space distortions (RSD; Kaiser 1987), plays an important role in constraining modified gravity theories in the late-time Universe. In the power spectrum analysis, we cannot measure the growth rate function by itself, but usually, by the combination  $f\sigma_8 = d \ln \sigma_8 / d \ln a$  (Song & Percival 2009; Percival & White 2009) using  $\sigma_8$  representing the rms of matter fluctuations on the  $8 h^{-1}$  Mpc scale. For example, the most recent observations, BOSS and eBOSS, measured  $f\sigma_8$  with a precision of  $\sim 5\%$  in the redshift range  $0.2 < z < 1.0$  (Alam et al. 2021a).

One concern is to test modified gravity theories directly using existing  $f\sigma_8$  measurements. The standard practice is constructing a model of the non-linear galaxy power spectrum assuming GR, then using that model to measure  $f\sigma_8$  from data up to the mildly non-linear region ( $k \sim 0.2 h \text{ Mpc}^{-1}$ ) (for recent studies, e.g., d’Amico et al. 2020; Ivanov et al. 2020; Lange et al. 2022; Kobayashi et al. 2022; Yuan et al. 2022). Therefore, it is worth noting that many existing analysis results using galaxy data up to the non-linear region only verify the consistency of GR. Thus, to test the gravity theory by consistently considering both linear and non-linear effects, a power spectrum model that considers non-linear effects specific to the modified gravity theory of interest is necessary. Several studies have been done on this for various modified gravity theories (Koyama et al. 2009; Taruya et al. 2014a,b; Takushima et al. 2015; Bellini & Zumalacárregui 2015; Taruya 2016; Barreira et al. 2016; Bose & Koyama 2016; Cusin et al. 2018a,b; Bose et al. 2017, 2018; Aviles et al. 2018; Hernández-Aguayo et al. 2019; Cataneo et al. 2019; Valogiannis et al. 2020; Valogiannis & Bean 2019; Bose et al. 2020b). However, only one study constrained the



theory from actual galaxy data using a galaxy power spectrum model that consistently includes the non-linear effects arising from modified gravity (Song et al. 2015a), where the authors focused on  $f(R)$  gravity (Hu & Sawicki 2007).

In particular, Hirano et al. (2020) pointed out that in DHOST theories, even the next-order solutions of the power spectrum in perturbation theory, the so-called one-loop solutions, are challenging to perform physically meaningful theoretical calculations due to the divergence of the wavenumber integral in the ultraviolet (UV) region. Therefore, the modelling of non-linear power spectra in DHOST theories is still highly uncertain.

### 1.5 Developments in the study of galaxy three-point statistics

A more straightforward way to investigate the non-linearity of scalar-tensor theories is to use three-point statistics of cosmological fluctuations, i.e., the 3PCF or the bispectrum. The reason is that, on large scales, the three-point statistics consist of a combination of second-order and linear-order dark matter fluctuations. The second-order fluctuations depend on two wave vectors in Fourier space and can be decomposed into three components using the angle between the two wave vectors: monopole (growth), dipole (shift), and quadrupole (tidal force) (Schmittfull et al. 2015). For example, Horndeski theories deviate only the coefficient of the tidal term from GR while keeping the shift term among these three components (Bernardeau & Brax 2011; Takushima et al. 2014; Bartolo et al. 2013; Bellini et al. 2015; Burrage et al. 2019). On the other hand, DHOST theories change both the shift and tidal terms (Hirano et al. 2018; Crisostomi et al. 2020; Lewandowski 2020), and this change in the shift term leads to a violation of the LSS consistency relation (Crisostomi et al. 2020; Lewandowski 2020). In addition to scalar-tensor theories, there has been much research on higher-order statistics in, for example,  $f(R)$  gravity theory (Gil-Marín et al. 2011; Borisov & Jain 2009; Hellwing et al. 2013; Bose & Taruya 2018; Bose et al. 2020a). Several observational proposals have been made to test modified gravity theories using cosmological three-point statistics, such as galaxy clustering (Yamauchi et al. 2017b; Yamauchi & Sugiyama 2022), weak lensing (Dinda 2018; Munshi et al. 2020b,a; Munshi & McEwen 2020), and CMB lensing (Namikawa et al. 2018, 2019), but none have been applied to actual observational data yet.

In the context of the galaxy three-point statistics, 3PCF resolves the degeneracy between the linear bias  $b_1$  and  $\sigma_8$  and allows us to directly study the evolution of dark matter density fluctuations apart from the RSD effect (Fry 1994; Frieman & Gaztanaga 1994; Matarrese et al. 1997; Verde et al. 1998; Gaztañaga & Scoccimarro 2005; Sefusatti et al. 2006; Greig et al. 2013; Hoffmann et al. 2015; Samushia et al. 2021). Furthermore, many previous studies have proposed to constrain primordial non-Gaussianities from the galaxy three-point statistics (Fry & Scherrer 1994; Verde et al. 2000; Scoccimarro et al. 2004; Sefusatti & Komatsu 2007; Sefusatti 2009; Sefusatti et al. 2010; Liguori et al. 2010; Desjacques & Seljak 2010; Sefusatti et al. 2012; Scoccimarro et al. 2012; Alvarez et al. 2014; Tellarini et al. 2015, 2016; Welling et al. 2016; Yamauchi et al. 2017a; Karagiannis et al. 2018; Bharadwaj et al. 2020; Moradinezhad Dizgah et al. 2021; Shirasaki et al. 2021; Coulton et al. 2023; Karagiannis et al. 2022). Recently, as in the case of the galaxy two-point statistics (e.g., Matsubara 2004; Taruya et al. 2011), the anisotropic component of the galaxy three-point statistics induced by the RSD effect and the Alcock-Paczyński (AP) effect (Alcock & Paczyński 1979) has attracted much attention, and its cosmological utility has been actively studied (Song et al.

2015b; Gagrani & Samushia 2017; Yankelevich & Porciani 2019; Gualdi & Verde 2020; Mazumdar et al. 2020; Sugiyama et al. 2021; Agarwal et al. 2021; Rizzo et al. 2023; Tsedrik et al. 2023).

Based on standard perturbation theory (SPT), many theoretical studies of the galaxy three-point statistics have been conducted to calculate higher-order non-linearities, redshift-space distortions, and bias effects, and the results of these calculations have been tested for validity by comparing them with measurements from N-body simulations (Peebles 1980; Fry 1984; Goroff et al. 1986; Hivon et al. 1995; Scoccimarro 1997; Scoccimarro et al. 1998; Jing & Boerner 1997; Scoccimarro et al. 1999; Scoccimarro 2000; Barriga & Gaztanaga 2002; Barriga & Gaztañaga 2002; Gaztañaga & Scoccimarro 2005; Pan et al. 2007; Marín et al. 2008; Guo & Jing 2009; Pollack et al. 2012; Lazanu et al. 2016; McCullagh et al. 2016; Lazanu et al. 2016; Lazanu & Liguori 2018; Hoffmann et al. 2018; Desjacques et al. 2018c; Child et al. 2018; Eggemeier et al. 2019; Oddo et al. 2020; Eggemeier et al. 2021; Oddo et al. 2021; Philcox et al. 2022). Other approaches have been widely used in research, such as the halo models (Ma & Fry 2000; Scoccimarro et al. 2001b; Takada & Jain 2003; Fosalba et al. 2005; Smith et al. 2008; Yamamoto et al. 2017; Nan et al. 2018) and fitting formulas (Scoccimarro & Frieman 1999; Scoccimarro & Couchman 2001; Gil-Marín et al. 2012, 2014; Takahashi et al. 2020). Beyond SPT, several improved perturbation theories have been proposed. Rampf & Wong (2012) used a resummation method based on Lagrangian perturbation theory. Baldauf et al. (2015b); Munshi & Regan (2017); Ivanov et al. (2022) discussed some correction terms for SPT based on the effective field theory of large-scale structure. Hashimoto et al. (2017) applied a resummation method similar to the TNS model of the power spectrum (Taruya et al. 2010). Kuruvilla & Porciani (2020) generalised the so-called streaming model to higher-order statistics. Blas et al. (2016a); Ivanov & Sibiryakov (2018) developed the time-sliced perturbation theory (TSPT) to resum the IR modes of the bulk flow and describe the non-linear damping of Baryon Acoustic Oscillations (BAOs; Peebles & Yu 1970; Sunyaev & Zeldovich 1970). Sugiyama et al. (2021) constructed a new IR-resummed bispectrum model by adding a term to the model proposed by TSPT.

The measurement of three-point statistics for galaxies, galaxy clusters, and quasars has a long history. As a simple method, two-dimensional three-point angular statistics have been observed from the dawn of the study of cosmological three-point statistics to the present (Peebles & Groth 1975; Peebles 1975; Groth & Peebles 1977; Fry & Peebles 1980; Fry & Seldner 1982; Sharp et al. 1984; Jing & Zhang 1989; Jing et al. 1991; Toth et al. 1989; Frieman & Gaztañaga 1999; Szapudi et al. 2001; de Carvalho et al. 2020). Eventually, with the development of spectroscopic observations of galaxies, three-dimensional three-point statistics have become the primary targets observed in configuration space (Bean et al. 1983; Efstathiou & Jedrzejewski 1994; Hale-Sutton et al. 1989; Gott et al. 1991; Jing & Börner 1998; Jing & Börner 2004; Kayo et al. 2004; Wang et al. 2004; Gaztañaga et al. 2005; Pan & Szapudi 2005; Nichol et al. 2006; Kulkarni et al. 2007; Gaztañaga et al. 2009; Marin 2011; McBride et al. 2011a,b; Marin et al. 2013; Guo et al. 2014; Moresco et al. 2017a; Slepian et al. 2017a; Slepian et al. 2017b; Moresco et al. 2017b, 2021) or in Fourier space (Baumgart & Fry 1991; Scoccimarro et al. 2001a; Feldman et al. 2001; Verde et al. 2002; Nishimichi et al. 2007; Gil-Marín et al. 2015a,b, 2017a; Pearson & Samushia 2018; Sugiyama et al. 2019; Philcox & Ivanov 2022; Cabass et al. 2022b; D’Amico et al. 2022a; Cabass et al. 2022a; D’Amico et al. 2022b). As another approach, Chiang et al. (2015) measured the squeezed limit bispectrum by splitting the observing region and measuring the

position-dependent power spectrum. Since the first measurement of the galaxy three-point statistics by Peebles & Groth (1975), the three-point statistic measurement has long been limited to measuring only certain scale-dependence of the three-point statistics. However, it is now possible to perform cosmological analysis using the information on the full shape of galaxy three-point statistics at cosmological scales ( $\sim 100 h^{-1} \text{Mpc}$ ).

In recent years, cosmological analysis of the three-point statistics of galaxies has made remarkable progress, mostly focusing on the isotropic component, i.e., *monopole*, of the three-point statistics. Slepian et al. (2017b) and Pearson & Samushia (2018) reported the detection of the BAO signal through the monopole 3PCF and the monopole bispectrum, respectively. Gil-Marín et al. (2017a); d’Amico et al. (2020); Philcox & Ivanov (2022) performed a joint analysis of the monopole and quadrupole power spectra and the monopole bispectrum to constrain the cosmological parameters of interest. Cabass et al. (2022b); D’Amico et al. (2022a); Cabass et al. (2022a) constrained primordial non-Gaussianities using the monopole bispectrum.

The anisotropic components, i.e., *quadrupole* and *hexadecapole*, of the galaxy three-point statistics have been the subject of pretty limited studies of measurements and cosmological analyses from actual galaxy data. Sugiyama et al. (2019) reported the first detection of the quadrupole bispectrum signal at the  $14\sigma$  level from the BOSS DR12 galaxies. Sugiyama et al. (2021) performed an anisotropic BAO analysis using the monopole and quadrupole components of the 2PCF and 3PCF for the MultiDark-Patchy mock catalogues (Patchy mocks; Kitaura et al. 2016) reproducing the BOSS galaxy distribution, showing the improvement of the Hubble parameter constraint by  $\sim 30\%$  compared to the 2PCF-only analysis result. D’Amico et al. (2022b) performed the first joint analysis of the monopole and quadrupole components of the power and bispectra measured from the BOSS DR12 galaxy data. More recently, Ivanov et al. (2023) presented the results of an anisotropic bispectrum analysis including quadrupole and hexadecapole components measured from the BOSS DR12 data.

## 1.6 Goal of this paper

The primary goal of this paper is to use the 3PCF of galaxies to perform a consistent cosmological analysis that constrains DHOST theories and their subclass, Horndeski theories, while accounting for linear and non-linear effects. To this end, Yamauchi & Sugiyama (2022) pointed out that the parameters characterising non-linear density fluctuations in DHOST theories degenerate with the non-linear bias parameter, so measuring the non-linear velocity field due to the RSD effect is essential. In addition, the authors proposed a simple parameterisation scheme that characterises the time evolution of the scale dependence of the non-linear velocity field to facilitate the combined analysis of galaxy samples at different redshifts. Specifically, the time evolution of the shift and tidal terms of the second-order velocity field is represented by  $\xi_s$  and  $\xi_t$ , respectively, where  $\xi_s = 0$  and  $\xi_t = 15/1144$  in GR. Following the suggestion of Yamauchi & Sugiyama (2022), we apply the joint analysis method of the anisotropic 2PCF and 3PCF of galaxies established by Sugiyama et al. (2021) to BOSS Data Release 12 galaxies (Eisenstein et al. 2011; Bolton et al. 2012; Dawson et al. 2013; Alam et al. 2015) to constrain these  $\xi_s$  and  $\xi_t$  parameters.

When we need to use values of fiducial cosmology parameters in our analysis, we adopt a flat  $\Lambda$ CDM model with the following parameters: matter density  $\Omega_{m0} = 0.31$ , Hubble constant  $h \equiv H_0/(100 \text{ km s}^{-1} \text{ Mpc}^{-1}) = 0.676$ , baryon density  $\Omega_{b0} h^2 = 0.022$ , and spectral tilt  $n_s = 0.97$ , which are the

same as those used in the final cosmological analysis in the BOSS project (Alam et al. 2017) and consistent with the best-fit values in Planck 2018 (Aghanim et al. 2020). We adopt a value for the total neutrino mass of  $\sum m_\nu = 0.06 \text{ eV}$  close to the minimum allowed by neutrino oscillation experiments. We use these fiducial parameters to estimate the distance to galaxies from the observed redshift of each galaxy and to calculate the shape of the linear matter power spectrum at the redshifts of interest with CLASS (Blas et al. 2011).

## 2 DHOST THEORIES

In this section, we briefly review the analytic expressions of DHOST theories. Section 2.1 introduces the class I DHOST theory and the perturbative solutions of the density and velocity fields of dark matter and galaxies solved up to the second-order in that theory. In Eqs. (2.1)-(2.14) of this subsection, we adopt the expressions and notations given by Hirano et al. (2018). Section 2.2 discusses the limitation of the assumptions adopted to derive the perturbative solutions used in this paper.

### 2.1 Density and velocity fluctuations in DHOST theories

We begin by summarising the theoretical models we will investigate in this paper and the assumptions used to derive those models.

(i) Gravity theory is a subclass of quadratic DHOST theories, the class I DHOST theory (Crisostomi et al. 2016), which encompasses Horndeski and Beyond Horndeski theories and is free from the instabilities of a cosmological background (de Rham & Matas 2016; Langlois et al. 2017).

(ii) Matter is cold dark matter (CDM) that can be described as a pressureless perfect fluid without vorticity (Bernardeau et al. 2002).

(iii) Matter is minimally coupled to gravity, and the effects of the DHOST gravity appear only through the gravitational potential.

(iv) When solving the equations of motion of metric tensor and scalar fields in DHOST theories, the quasi-static approximation (e.g., Pace et al. 2021) is used. Then, the gravitational potential is determined by a modified Poisson equation (Hirano et al. 2018; Crisostomi et al. 2020; Lewandowski 2020; Hirano et al. 2020).

(v) Statistical properties of the CDM fluctuations are those derived in the standard theory of inflation, which satisfy the following properties: adiabaticity, negligibly weak non-Gaussianity, nearly scale-free, statistical homogeneity, statistical isotropy, and statistical parity symmetry.

(vi) Galaxy biases are assumed to be present only in the density field, and three biases are considered: linear bias  $b_1$ , second-order local bias  $b_2$ , and second-order non-local bias (tidal bias)  $b_{s2}$  (for a review, see e.g., Saito et al. 2014; Desjacques et al. 2018b). Any bias effects related to higher-order derivatives and the velocity field of the galaxy are ignored.

The action of quadratic DHOST theories is given by (Langlois & Noui 2016; Crisostomi et al. 2016)

$$\begin{aligned}
 S_{\text{DHOST}} = \int d^4x \sqrt{-g} & \left[ \mathcal{G}_2(\phi, X) - \mathcal{G}_3(\phi, X) \square \phi + \mathcal{F}(\phi, X) R \right. \\
 & + a_1 \phi_{\mu\nu} \phi^{\mu\nu} + a_2 (\square \phi)^2 + a_3 (\square \phi) \phi^\mu \phi_{\mu\nu} \phi^\nu \\
 & \left. + a_4 \phi^\mu \phi_{\mu\rho} \phi^{\rho\nu} \phi_\nu + a_5 (\phi^\mu \phi_{\mu\nu} \phi^\nu)^2 \right], \quad (2.1)
 \end{aligned}$$

where  $\phi_\mu = \nabla_\mu \phi$ ,  $\phi_{\mu\nu} = \nabla_\mu \nabla_\nu \phi$ ,  $X = -\phi_\mu \phi^\mu / 2$ , and  $a_i = a_i(\phi, X)$  for  $i = 1, \dots, 5$ . The functions  $a_i$  ( $i = 1, \dots, 5$ ) satisfy the degeneracy condition given by (Crisostomi et al. 2016) to avoid the Ostrogradsky ghost (Ostrogradsky 1850; Woodard 2015).

The density perturbation  $\delta$  and velocity field  $\mathbf{v}$  of dark matter follow the equations of a pressureless perfect fluid without vorticity:

$$\begin{aligned} \dot{\delta}(\mathbf{x}) + a^{-1} \partial_i \left( (1 + \delta(\mathbf{x})) v^i(\mathbf{x}) \right) &= 0, \\ \dot{\theta}(\mathbf{x}) + H\theta(\mathbf{x}) + a^{-1} \partial_i \left( v^j(\mathbf{x}) \partial_j v^i(\mathbf{x}) \right) &= -a^{-1} \partial^2 \Phi(\mathbf{x}) \end{aligned} \quad (2.2)$$

where  $a$  and  $H = \dot{a}/a$  respectively denote the scale factor and the Hubble parameter, and  $\theta = \partial_i v^i$  is the divergence of the velocity field. Because of no vorticity, the velocity field is represented as  $v^i = (\partial_i / \partial^2) \theta$ . The gravitational potential  $\Phi$  is determined by the following modified Poisson equation (Hirano et al. 2018):

$$\frac{\partial^2 \Phi(\mathbf{x})}{a^2 H^2} = \kappa \delta(\mathbf{x}) + \nu \frac{\dot{\delta}(\mathbf{x})}{H} + \mu \frac{\ddot{\delta}(\mathbf{x})}{H^2} + \frac{\partial^2 S_\Phi^{\text{NL}}(\mathbf{x})}{a^2 H^2}, \quad (2.3)$$

where  $\kappa$ ,  $\nu$ , and  $\mu$  are functions that depend only on time, and  $S_\Phi^{\text{NL}}$  is a non-linear source term obtained from the equation of motion of the scalar field.

To solve the above equations, we expand all the fluctuations as follows:  $X = \sum_n X_n$ , where  $X = \{\delta, \theta, \Phi, S_\Phi^{\text{NL}}\}$ , and  $X_n = \mathcal{O}(\delta_1^n)$ . Then, the non-linear source  $S_\Phi^{\text{NL}}$  up to the second-order is given by

$$\begin{aligned} \frac{\partial^2 S_{\Phi,1}^{\text{NL}}(\mathbf{x})}{a^2 H^2} &= 0, \\ \frac{\partial^2 S_{\Phi,2}^{\text{NL}}(\mathbf{x})}{a^2 H^2} &= \tau_\alpha W_\alpha(\mathbf{x}) - \tau_\gamma W_\gamma(\mathbf{x}), \end{aligned} \quad (2.4)$$

where

$$\begin{aligned} W_\alpha(\mathbf{x}) &= [\delta_1(\mathbf{x})]^2 + \left[ \frac{\partial_i}{\partial^2} \delta_1(\mathbf{x}) \right] [\partial_i \delta_1(\mathbf{x})], \\ W_\gamma(\mathbf{x}) &= [\delta_1(\mathbf{x})]^2 - \left[ \frac{\partial_i \partial_j}{\partial^2} \delta_1(\mathbf{x}) \right]^2. \end{aligned} \quad (2.5)$$

The evolution of the density perturbation follows

$$\ddot{\delta}(\mathbf{x}) + (2 + \varsigma) H \dot{\delta}(\mathbf{x}) - \frac{3}{2} \Omega_m \Xi H^2 \delta(\mathbf{x}) = H^2 S_\delta^{\text{NL}}(\mathbf{x}), \quad (2.6)$$

where  $\varsigma = (2\mu - \nu)/(1 - \mu)$ ,  $(3/2)\Omega_m \Xi = \kappa/(1 - \mu)$ , and  $S_\delta^{\text{NL}}$  is a non-linear source of the density perturbation, vanishing at linear order and given at second-order by

$$S_{\delta,2}^{\text{NL}} = S_\alpha W_\alpha(\mathbf{x}) - S_\gamma W_\gamma(\mathbf{x}) \quad (2.7)$$

with

$$\begin{aligned} (1 - \mu) S_\alpha &= 2f^2 + \frac{3}{2} \Omega_m \Xi - \varsigma f + \tau_\alpha, \\ (1 - \mu) S_\gamma &= f^2 + \tau_\gamma. \end{aligned} \quad (2.8)$$

Once the solution of  $\delta$  is obtained, the solution of  $\theta$  is also derived from the continuity equation in Eq. (2.2). In Fourier space<sup>10</sup>, Eqs. (2.2) and (2.3) determine  $\delta_n(\mathbf{k})$  and  $\theta_n(\mathbf{k})$  in terms of the linear

density fluctuations to be:

$$\begin{aligned} \tilde{\delta}_n(\mathbf{k}) &= \int \frac{d^3 p_1}{(2\pi)^3} \cdots \int \frac{d^3 p_n}{(2\pi)^3} (2\pi)^3 \delta_{\text{D}}(\mathbf{k} - \mathbf{p}_{[1n]}) \\ &\quad \times F_n^{(m)}(\mathbf{p}_1, \dots, \mathbf{p}_2) \delta_1(\mathbf{p}_1) \cdots \delta_1(\mathbf{p}_n), \\ \tilde{\theta}_n(\mathbf{k}) &= -aHf \int \frac{d^3 p_1}{(2\pi)^3} \cdots \int \frac{d^3 p_n}{(2\pi)^3} (2\pi)^3 \delta_{\text{D}}(\mathbf{k} - \mathbf{p}_{[1n]}) \\ &\quad \times G_n^{(m)}(\mathbf{p}_1, \dots, \mathbf{p}_2) \delta_1(\mathbf{p}_1) \cdots \delta_1(\mathbf{p}_n), \end{aligned} \quad (2.9)$$

where  $\mathbf{p}_{[1n]} = \mathbf{p}_1 + \cdots + \mathbf{p}_n$ , and  $\delta_{\text{D}}$  is the delta function. The functions  $F_2^{(m)}$  and  $G_2^{(m)}$  are kernel functions that characterise the gravitational non-linear effects, and the superscript (m) stands for ‘‘matter’’. In the second-order,  $F_2^{(m)}$  and  $G_2^{(m)}$  are given by

$$\begin{aligned} F_2^{(m)}(\mathbf{p}_1, \mathbf{p}_2) &= \kappa_\delta \alpha_s(\mathbf{p}_1, \mathbf{p}_2) - \frac{2}{7} \lambda_\delta \gamma(\mathbf{k}_1, \mathbf{k}_2) \\ G_2^{(m)}(\mathbf{p}_1, \mathbf{p}_2) &= \kappa_\theta \alpha_s(\mathbf{p}_1, \mathbf{p}_2) - \frac{4}{7} \lambda_\theta \gamma(\mathbf{k}_1, \mathbf{k}_2), \end{aligned} \quad (2.10)$$

where

$$\begin{aligned} \alpha_s(\mathbf{k}_1, \mathbf{k}_2) &= 1 + (\hat{k}_1 \cdot \hat{k}_2) \frac{(k_1^2 + k_2^2)}{2k_1 k_2}, \\ \gamma(\mathbf{k}_1, \mathbf{k}_2) &= 1 - (\hat{k}_1 \cdot \hat{k}_2)^2, \end{aligned} \quad (2.11)$$

and

$$\begin{aligned} \kappa_\theta &= 2\kappa_\delta \left[ 1 + \frac{1}{2f} \frac{d \ln \kappa_\delta}{d \ln a} \right] - 1, \\ \lambda_\theta &= \lambda_\delta \left[ 1 + \frac{1}{2f} \frac{d \ln \lambda_\delta}{d \ln a} \right]. \end{aligned} \quad (2.12)$$

The evolutions of  $\kappa_\delta$  and  $\lambda_\delta$  follow

$$\begin{aligned} \ddot{\kappa}_\delta + [4f + (2 + \varsigma)] H \dot{\kappa}_\delta + H^2 \left( 2f^2 + \frac{3}{2} \Omega_m \Xi \right) \kappa_\delta \\ = H^2 S_\alpha, \end{aligned} \quad (2.13)$$

$$\begin{aligned} \ddot{\lambda}_\delta + [4f + (2 + \varsigma)] H \dot{\lambda}_\delta + H^2 \left( 2f^2 + \frac{3}{2} \Omega_m \Xi \right) \lambda_\delta \\ = \frac{7}{2} H^2 S_\gamma. \end{aligned} \quad (2.14)$$

Since the galaxy density field is a biased quantity, we assume the linear bias  $b_1$ , the second-order local bias  $b_2$ , and the second-order tidal bias  $b_{s,2}$  as the bias parameters that describe the galaxy density fluctuation up to second order (e.g., Desjacques et al. 2018b):

$$\delta^{(g)}(\mathbf{x}) = b_1 \delta(\mathbf{x}) + \frac{b_2}{2} [\delta(\mathbf{x})]^2 + b_{s,2} [s_{ij}]^2, \quad (2.15)$$

where the superscript (g) stands for ‘‘galaxy’’, and  $[s_{ij}]^2$  is given by

$$[s_{ij}]^2 = \left[ \frac{\partial_i \partial_j}{\partial^2} \delta(\mathbf{x}) \right]^2 - \frac{1}{3} [\delta(\mathbf{x})]^2. \quad (2.16)$$

Then, the second-order kernel functions for galaxies are given by

$$\begin{aligned} F_2^{(g)} &= b_1 F_2^{(m)}(\mathbf{p}_1, \mathbf{p}_2) + \frac{1}{2} b_2 + b_{s,2} \left[ (\hat{p}_1 \cdot \hat{p}_2)^2 - \frac{1}{3} \right], \\ G_2^{(g)} &= G_2^{(m)}(\mathbf{p}_1, \mathbf{p}_2). \end{aligned} \quad (2.17)$$

The RSD effect shifts the observed position of galaxies  $\mathbf{x}_{\text{red}}$  from their real-space position  $\mathbf{x}'$  due to the peculiar velocity of galaxies along the line-of-sight (LOS) direction:

$$\mathbf{x}_{\text{red}}(\mathbf{x}') = \mathbf{x}' + \frac{\mathbf{v}(\mathbf{x}') \cdot \hat{n}}{aH} \hat{n}, \quad (2.18)$$

where  $\hat{n}$  is a unit vector pointing to the galaxy from the origin. The

<sup>10</sup> Our convention for the Fourier transform is

$$\tilde{f}(\mathbf{k}) = \int d^3 x e^{-i\mathbf{k} \cdot \mathbf{x}} f(\mathbf{x}).$$



observed galaxy density fluctuation is then distorted along the LOS direction as follows:

$$\delta_s^{(g)}(\mathbf{x}) = \int d^3x' \left(1 + \delta^{(g)}(\mathbf{x}')\right) \delta_D(\mathbf{x} - \mathbf{x}_{\text{red}}(\mathbf{x}')) - 1. \quad (2.19)$$

In Fourier space, the  $n$ -th order solution of  $\delta_s^{(g)}$  is represented as

$$\begin{aligned} \tilde{\delta}_{s,n}^{(g)}(\mathbf{k}) &= \int \frac{d^3p_1}{(2\pi)^3} \cdots \int \frac{d^3p_n}{(2\pi)^3} (2\pi)^3 \delta_D(\mathbf{k} - \mathbf{p}_{[1n]}) \\ &\times Z_n(\mathbf{p}_1, \dots, \mathbf{p}_2) \delta_1(\mathbf{p}_1) \cdots \delta_1(\mathbf{p}_n). \end{aligned} \quad (2.20)$$

The first and second-order kernel functions are given by (Scoccimarro et al. 1999)

$$\begin{aligned} Z_1 &= b_1 + f(\hat{p} \cdot \hat{n})^2, \\ Z_2 &= F_2^{(g)}(\mathbf{p}_1, \mathbf{p}_2) + f(\hat{k} \cdot \hat{n})^2 G_2^{(g)}(\mathbf{p}_1, \mathbf{p}_2) \\ &+ \frac{f(\mathbf{k} \cdot \hat{n})}{2} \left[ \frac{(\hat{p}_1 \cdot \hat{n})}{p_1} Z_1(\mathbf{p}_2) + \frac{(\hat{p}_2 \cdot \hat{n})}{p_2} Z_1(\mathbf{p}_1) \right], \end{aligned} \quad (2.21)$$

where  $\mathbf{k} = \mathbf{p}_1 + \mathbf{p}_2$ . In the rest of this paper, we focus only on the galaxy density fluctuation with RSDs, so for simplicity of notation, we refer to it simply as  $\delta$  instead of  $\delta_s^{(g)}$ . We also omit the angle-dependence  $\hat{n}$  of any function that includes RSDs.

At the leading-order in perturbation theory, the redshift-space power spectrum and bispectrum are represented as

$$\begin{aligned} P(\mathbf{k}) &= [Z_1(\mathbf{k})]^2 P_{\text{lin}}(k), \\ B(\mathbf{k}_1, \mathbf{k}_2, \mathbf{k}_3) &= 2Z_2(\mathbf{k}_1, \mathbf{k}_2) Z_1(\mathbf{k}_1) Z_1(\mathbf{k}_2) P_{\text{lin}}(k_1) P_{\text{lin}}(k_2) \\ &+ 2 \text{ perms.}, \end{aligned} \quad (2.22)$$

where  $\mathbf{k}_1 + \mathbf{k}_2 + \mathbf{k}_3 = 0$ , and  $P_{\text{lin}}$  is the linear matter power spectrum. In what follows, we omit the  $\mathbf{k}_3$ -dependence of the bispectrum for notational simplicity:  $B(\mathbf{k}_1, \mathbf{k}_2) = B(\mathbf{k}_1, \mathbf{k}_2, \mathbf{k}_3 = -\mathbf{k}_1 - \mathbf{k}_2)$ .

Finally, we conclude this subsection by summarising the key points about galaxy fluctuations from a theoretical point of view. First, in the case of  $\nu = \mu = \tau_\alpha = 0$  in Eqs. (2.3) and (2.4), Horndeski theories are recovered; a  $\Lambda$ CDM model additionally has  $\kappa = (3/2)\Omega_m(z)$  and  $\tau_\gamma = 0$ ; in both Horndeski theories and  $\Lambda$ CDM,  $\kappa_\delta = \kappa_\theta = 1$  from Eq. (2.13), and  $\lambda_\delta$  and  $\lambda_\theta$  are still time-dependent from Eq. (2.14); for the approximation  $f^2 = \Omega_m$  in  $\Lambda$ CDM,  $\lambda_\delta = \lambda_\theta = 1$ . Second, since the linear equation of the density fluctuation (2.6) omits space-dependence as in the  $\Lambda$ CDM case, under the assumption that the scalar field becomes to prevail during the accelerated Universe, the shape of the linear matter power spectrum can be the usual  $\Lambda$ CDM one determined in the matter-dominant era. In other words, the characteristic scale-dependences in  $\delta$  and  $v$  due to scalar-tensor theories appear only through the non-linear kernel functions  $F_{n \geq 2}^{(m)}$  and  $G_{n \geq 2}^{(m)}$ . Third, the non-linear terms that appear in the fluid equation in Eq. (2.2) and the Poisson equation in Eq. (2.3), such as  $\partial_i(\delta v^i)$ ,  $\partial_i(v^j \partial_j v^i)$ ,  $W_\alpha$  and  $W_\gamma$ , become zero when the volume average or ensemble average is calculated. Therefore, the resulting non-linear solutions satisfy  $\int d^3x \delta_n = \langle \delta_n \rangle = 0$  and  $\int d^3x \theta_n = \langle \theta_n \rangle = 0$  for  $n \geq 2$ , and the corresponding kernel functions satisfy  $F_{n \geq 2}^{(m)} = G_{n \geq 2}^{(m)} = 0$  when  $\mathbf{p}_1 + \cdots + \mathbf{p}_n = 0$  as known in the case of  $\Lambda$ CDM. This condition partially breaks when the non-linear bias effect is taken into account, resulting in  $F_2^{(g)}(\mathbf{p}, -\mathbf{p}) \neq 0$  and  $G_2^{(g)}(\mathbf{p}, -\mathbf{p}) = 0$  (see Eq. (2.17)).

## 2.2 Limitation of our assumptions

This subsection discusses the possible cases where the assumptions adopted in building the theoretical model in the previous subsection are violated, introducing some previous studies. The following bullet labels correspond to those in Section 2.1.

(i) Besides scalar-tensor theories, two other examples of modified gravity theories have been widely studied in cosmology: the Hu-Sawicki model (Hu & Sawicki 2007) of  $f(R)$  gravity (see Capozziello & Francaviglia 2008; Sotiriou & Faraoni 2010, for reviews) and the normal branch of the 5D brane-world Dvali-Gabadadze-Porrati model (nDGP; Dvali et al. 2000). These two models have been investigated in detail by Alam et al. (2021b) as representative targets in DESI. Focusing on the non-linear effects, the nDGP model generates a scale dependence of the same form as Horndeski theories, characterised by the function  $\gamma(\mathbf{p}_1, \mathbf{p}_2)$  (2.11). On the other hand, the Hu-Sawicki  $f(R)$  model produces a kernel function different from the one predicted by scalar-tensor theories. Specifically, in the modified Poisson equation of Eq. (2.3),  $\kappa$  is scale-dependent, resulting in the linear growth function that depends on the wavenumber. In addition, the non-linear source  $S_\Phi^{\text{NL}}$  for the Hu-Sawicki model also appears as a form that cannot be described by  $W_\alpha$  and  $W_\gamma$ , unlike Eq. (2.4). Such non-linearities in the density field specific to the Hu-Sawicki model have been studied by (Koyama et al. 2009; Taruya 2016) in the context of perturbation theory, and the model has been tested by applying the theory to BOSS galaxy data (Song et al. 2015a).

(ii) The effect of the relative velocity of baryons and CDM enters the galaxy density fluctuation quadratically together with the corresponding bias parameter (Dalal et al. 2010), thus modifying the shape of the measured bispectrum. In particular, as in the case of the  $\kappa_\delta$  parameter in DHOST theories, it corrects the term in  $F_2^{(g)}(\mathbf{p}_1, \mathbf{p}_2)$  that depends on  $(\hat{p}_1 \cdot \hat{p}_2)$  called the shift term (Yoo et al. 2011). The relative velocity effect on galaxy clustering has been measured using the galaxy power spectrum (Yoo & Seljak 2013; Beutler et al. 2016) and 3PCF (Slepian et al. 2018), but any signature has not yet been detected.

Although massive neutrinos can also change the shape of the bispectrum, the results of simulations performed by Ruggeri et al. (2018) confirm that the CDM component in the bispectrum is dominant; Interestingly, Kamalinejad & Slepian (2020) has shown that the effect of neutrino corrections appears in the shift term as well as the growth and tidal terms in the second-order velocity field (3.16). Hence, the anisotropic 3PCF (or bispectrum) may help to constrain the neutrino masses (see e.g., Saito et al. 2009; Levi & Vlah 2016; Yoshikawa et al. 2020).

(iii) The case of non-minimally coupled scalar fields with CDM has already been the subject of several studies in the context of cosmology (Kimura et al. 2018; Chibana et al. 2019; Kase & Tsujikawa 2020b; Chiba et al. 2020; Kase & Tsujikawa 2020a). For example, Kimura et al. (2018); Chibana et al. (2019) have shown that in this case, the continuity equation (2.2) is modified, and thus the relation between the density fluctuations in real and redshift spaces, i.e. the Kaiser formula in linear theory (Kaiser 1987), is also modified.

(iv) The quasi-static approximation breaks when the scale of interest is close to the sound horizon scale. Even in GR, it is known that there are relativistic corrections to  $F_2^{(g)}$  when approaching the horizon size (Tram et al. 2016; Jolicoeur et al. 2017, 2018; Koyama et al. 2018; Castiblanco et al. 2019; Umeh et al. 2019; Calles et al. 2020; de Weerd et al. 2020).

(v) Various possibilities have been proposed for how the initial conditions of cosmic fluctuations predicted by inflation theory could affect observables. One of the most critical examples relevant to this paper is the existence of primordial non-Gaussianity, which

breaks the LSS consistency relation (Berezhiani & Khoury 2014; Valageas et al. 2017; Esposito et al. 2019).

(vi) Fujita & Vlah (2020) proposed a bias expansion formalism dubbed “Monkey bias” based on the LSS consistency relation and showed that it is equivalent to the existing bias expansion framework. In other words, in DHOST theories, which violate the LSS consistency relation, the existing bias expansion we adopted (2.15) may not be valid, and a new bias in the shift term of non-linear galaxy density fluctuations, i.e., the shift bias parameter, may appear. Moreover, the shift bias may also induce velocity bias effects.

In Section 9.12, we will discuss and clarify which parts of theories can be tested with the anisotropic 3PCF, even in the presence of the shift and velocity biases.

### 3 THEORETICAL MODELS

This section describes how to calculate the theoretical models of multipole 2PCFs and 3PCFs. Section 3.1 summarises the decomposition formalism for the anisotropic three-point statistics (bispectra and 3PCFs). Section 3.2 introduces the power and bispectrum models used to compute the 2PCF and 3PCF. Section 3.3 discusses what parameters should be varied to perform the cosmological analysis and shows the specific parameter dependence of the bispectrum model we use. Section 3.4 reviews new parameters helpful in testing DHOST theories proposed by Yamauchi & Sugiyama (2022) and their time evolution. Section 3.5 discusses the limits of applying our theoretical models of the 2PCF and 3PCF to the data analysis.

#### 3.1 Decomposition formalisms of the 2PCF and 3PCF

We follow the decomposition formalism of redshift-space bispectra proposed by Sugiyama et al. (2019) using the tri-polar spherical harmonics (TripoSH) as a basis function. In that formalism, under statistical homogeneity, isotropy, and parity-symmetry assumptions, we define the base function to expand the bispectrum using three spherical harmonics  $Y_{\ell m}$  as

$$\mathcal{S}_{\ell_1 \ell_2 \ell}(\hat{\mathbf{k}}_1, \hat{\mathbf{k}}_2, \hat{\mathbf{n}}) = \frac{4\pi}{h_{\ell_1 \ell_2 \ell}} \sum_{m_1 m_2 m} \begin{pmatrix} \ell_1 & \ell_2 & \ell \\ m_1 & m_2 & m \end{pmatrix} \times Y_{\ell_1 m_1}(\hat{\mathbf{k}}_1) Y_{\ell_2 m_2}(\hat{\mathbf{k}}_2) Y_{\ell m}(\hat{\mathbf{n}}), \quad (3.1)$$

where

$$h_{\ell_1 \ell_2 \ell} = \sqrt{\frac{(2\ell_1 + 1)(2\ell_2 + 1)(2\ell + 1)}{4\pi}} \begin{pmatrix} \ell_1 & \ell_2 & \ell \\ 0 & 0 & 0 \end{pmatrix}, \quad (3.2)$$

and the circle bracket with 6 multipole indices,  $(\dots)$ , denotes the Wigner-3j symbol. The bispectrum is then expanded as

$$B(\mathbf{k}_1, \mathbf{k}_2, \hat{\mathbf{n}}) = \sum_{\ell_1 + \ell_2 + \ell = \text{even}} B_{\ell_1 \ell_2 \ell}(k_1, k_2) \mathcal{S}_{\ell_1 \ell_2 \ell}(\hat{\mathbf{k}}_1, \hat{\mathbf{k}}_2, \hat{\mathbf{n}}), \quad (3.3)$$

and the corresponding multipole components are given by

$$B_{\ell_1 \ell_2 \ell}(k_1, k_2) = 4\pi h_{\ell_1 \ell_2 \ell}^2 \int \frac{d^2 \hat{\mathbf{k}}_1}{4\pi} \int \frac{d^2 \hat{\mathbf{k}}_2}{4\pi} \int \frac{d^2 \hat{\mathbf{n}}}{4\pi} \times \mathcal{S}_{\ell_1 \ell_2 \ell}^*(\hat{\mathbf{k}}_1, \hat{\mathbf{k}}_2) B(\mathbf{k}_1, \mathbf{k}_2). \quad (3.4)$$

Since the bispectrum multipoles defined here are independent of the coordinate system in which they are calculated, it is possible to compare theoretical calculations with observations in different

coordinate systems. Specifically, we use the following coordinate system with  $k_1$  as the  $z$ -axis for theoretical calculations:

$$\begin{aligned} \hat{\mathbf{k}}_1 &= \{0, 0, 1\} \\ \hat{\mathbf{k}}_2 &= \{\sin \theta_{k_2}, 0, \cos \theta_{k_2}\} \\ \hat{\mathbf{n}} &= \{\sin \theta \cos \varphi, \sin \theta \sin \varphi, \cos \theta\}. \end{aligned} \quad (3.5)$$

On the other hand, when measuring the bispectrum from galaxy data, we use the Cartesian coordinate and take the north pole as our  $z$ -axis (see Section 4.2).

We perform the expansion of the 3PCF in the same way as for the bispectrum. The resulting 3PCF multipoles are related to  $B_{\ell_1 \ell_2 \ell}$  through a two-dimensional Hankel transform:

$$\zeta_{\ell_1 \ell_2 \ell}(r_1, r_2) = i^{\ell_1 + \ell_2} \int \frac{dk_1 k_1^2}{2\pi^2} \int \frac{dk_2 k_2^2}{2\pi^2} \times j_{\ell_1}(r_1 k_1) j_{\ell_2}(r_2 k_2) B_{\ell_1 \ell_2 \ell}(k_1, k_2), \quad (3.6)$$

where  $j_\ell$  is the spherical Bessel function at the  $\ell$ -th order. This relation means that  $\zeta_{\ell_1 \ell_2 \ell}$  have in principle the same information as  $B_{\ell_1 \ell_2 \ell}$ , facilitating the comparison of the configuration-space and Fourier-space analyses.

Note that  $B_{\ell_1 \ell_2 \ell}(k_1, k_2) = B_{\ell_2 \ell_1 \ell}(k_2, k_1)$  and  $\zeta_{\ell_1 \ell_2 \ell}(r_1, r_2) = \zeta_{\ell_2 \ell_1 \ell}(r_2, r_1)$ . From this relation, when  $\ell_1 = \ell_2$ , only  $k_1 \geq k_2$  and  $r_1 \geq r_2$  need to be computed for the bispectrum and 3PCF, respectively. Also, when  $\ell > 0$ , only  $\ell_1 \geq \ell_2$  should be considered.

In the case of the power spectrum, it is common to expand the power spectrum using Legendre polynomial functions  $\mathcal{L}_\ell$  (e.g., Hamilton 1997):

$$P(\mathbf{k}) = \sum_\ell P_\ell(k) \mathcal{L}_\ell(\hat{\mathbf{k}} \cdot \hat{\mathbf{n}}), \quad (3.7)$$

and the corresponding multipole components of the 2PCF are given by

$$\xi_\ell(r) = i^\ell \int \frac{dk k^2}{2\pi^2} j_\ell(rk) P_\ell(k). \quad (3.8)$$

This paper tests DHOST theories by measuring  $\xi_\ell$  and  $\zeta_{\ell_1 \ell_2 \ell}$  from the BOSS galaxy data and comparing them with the corresponding theoretical models. The index  $\ell$  that is common for both  $\xi_\ell$  and  $\zeta_{\ell_1 \ell_2 \ell}$  represents the decomposition related to the RSD or AP effect, where  $\ell = 0$  means monopole,  $\ell = 2$  quadrupole, and  $\ell = 4$  hexadecapole. Relativistic effects can generate  $\ell = \text{odd}$  components (e.g., McDonald 2009; Desjacques et al. 2018a; Clarkson et al. 2019), but we ignore them here. Furthermore, we also ignore the  $\ell = 4$  modes; although the signal of the  $\ell = 4$  modes is too small to be detected in the BOSS data, it should be taken into account in the future as it helps to improve the constraints on the cosmological parameters (Beutler et al. 2017; Sugiyama et al. 2019). Therefore, in this paper, we focus on only two modes,  $\ell = 0$  and  $\ell = 2$ . In particular, for the 3PCF, we consider the first two terms of the monopole ( $\zeta_{000}$  and  $\zeta_{110}$ ) and the first two terms of the quadrupole ( $\zeta_{202}$  and  $\zeta_{112}$ ).

Finally, we discuss the relation with the widely used decomposition formalism of the bispectrum proposed by Scoccimarro et al. (1999). As in Eq. (3.5), this formalism decomposes the bispectrum by choosing the coordinate system with  $k_1$  as the  $z$ -axis and using the spherical harmonic function for the LOS direction:  $B(\mathbf{k}_1, \mathbf{k}_2, \hat{\mathbf{n}}) = \sum_{LM} B_{LM}(\mathbf{k}_1, \mathbf{k}_2) Y_{LM}(\hat{\mathbf{n}})$ . The relation between Scoccimarro et al. (1999)’s decomposition formalism and our TripoSH decomposition has already been shown in Eq. (25) of Sugiyama et al. (2019). According to the relation,  $\zeta_{202}$  contains only  $M = 0$  mode in Scoccimarro et al. (1999)’s formalism, while  $\zeta_{112}$  further contains the  $M \neq 0$  modes in addition to the  $M = 0$  mode.



The ability to handle the  $M \neq 0$  modes, including window function corrections (see Section 4.3), is one advantage of our TripoSH decomposition formalism. For example, studies of the quadrupole bispectrum using Scoccimarro et al. (1999)'s method have mainly dealt only with the  $M = 0$  mode (D'Amico et al. 2022b). One reason is that the correction formula for the window function effect is only given for the  $M = 0$  case (Pardede et al. 2022). Moreover, we show in Section 7 that  $\zeta_{112}$  gives additional cosmological information to  $\zeta_{202}$ , pointing out the importance of the  $M \neq 0$  modes.

### 3.2 IR-resummed power spectrum and bispectrum models

In this paper, we focus on the 2PCF and 3PCF at scales above  $80 h^{-1}$  Mpc (Section 9), where we can ignore loop corrections arising from higher-order non-linear effects. The power spectrum and bispectrum shapes can be described at those scales by their leading solutions, the so-called tree-level solutions (2.22). However, we need to consider the non-linear damping effect of BAOs due to the linear gravity that shifts the position of galaxies.

The non-linear damping of BAO can be described by a large-scale bulk flow that is position-independent in a given observed region (Eisenstein et al. 2007a; Crocce & Scoccimarro 2008; Matsubara 2008; Sugiyama & Spergel 2014; Baldauf et al. 2015a), called the infra-red (IR) flow. In the limit where the IR flow does not correlate with small-scale density fluctuations, based on the Galilean invariance of the system of equations in the IR limit, all the effects of the IR flow are cancelled out in equal-time  $n$ -point statistics (Jain & Bertschinger 1996; Scoccimarro & Frieman 1996; Kehagias & Riotto 2013; Peloso & Pietroni 2013; Sugiyama & Futamase 2013; Sugiyama & Spergel 2014; Blas et al. 2013, 2016b; Lewandowski & Senatore 2017). However, when we deviate from such an extreme situation, we find a correlation between the IR flow and the small-scale density field. By extracting this correlation in the full perturbative order only for the BAO signal, it becomes possible to describe the non-linear effects of BAOs. This kind of construction of  $n$ -point statistics models is called the IR resummation method (Crocce & Scoccimarro 2008; Matsubara 2008; Sugiyama & Spergel 2014; Senatore & Zaldarriaga 2015; Baldauf et al. 2015a; Blas et al. 2016a; Senatore & Trevisan 2018; Ivanov & Sibiryakov 2018; Lewandowski & Senatore 2020; Sugiyama et al. 2021). In this paper, we will use the IR resummed power and bispectrum models given in Eqs. (3.9) and (3.12), even in DHOST theories that break the IR cancellation, but we will mention the issues that may arise in this case in Section 3.5.

For the power spectrum, we adopt the following IR-resummed model:

$$P(\mathbf{k}) = [Z_1(\mathbf{k})]^2 [\mathcal{D}^2(\mathbf{k})P_w(k) + P_{\text{nw}}(k)], \quad (3.9)$$

where  $P_{\text{lin}}$  is decomposed into two parts: the "no-wiggle (nw)" part  $P_{\text{nw}}$  that is a smooth version of  $P_{\text{lin}}$  with the baryon oscillations removed (Eisenstein & Hu 1998), and the "wiggle (w)" part defined as  $P_w = P_{\text{lin}} - P_{\text{nw}}$ . The non-linear BAO degradation is represented by the two-dimensional Gaussian damping factor derived from a differential motions of Lagrangian displacements (Eisenstein et al. 2007a; Crocce & Scoccimarro 2008; Matsubara 2008):

$$\mathcal{D}(\mathbf{k}) = \exp\left(-\frac{k^2(1-\mu^2)\sigma_\perp^2 + k^2\mu^2\sigma_\parallel^2}{2}\right), \quad (3.10)$$

where  $\mu = \hat{k} \cdot \hat{n}$ . We compute the radial and transverse components of smoothing parameters,  $\sigma_\perp$  and  $\sigma_\parallel$ , using the Zel'dovich approximation (Zel'dovich 1970; Crocce & Scoccimarro 2008; Matsubara

2008):

$$\begin{aligned} \sigma_\perp^2 &= \frac{1}{3} \int \frac{dp}{2\pi^2} P_{\text{lin}}(p), \\ \sigma_\parallel^2 &= (1+f)^2 \sigma_\perp^2. \end{aligned} \quad (3.11)$$

The power spectrum model in Eq. (3.9) was first proposed empirically by Eisenstein et al. (2007a). Subsequently, the damping factor  $\mathcal{D}^2$  in front of  $P_{\text{lin}}$  was derived in the context of perturbation theory by Crocce & Scoccimarro (2008); Matsubara (2008); an additional term to recover a smooth linear power spectrum without BAOs,  $(1 - \mathcal{D}^2)P_{\text{nw}}$ , was derived using the IR resummation method (Sugiyama & Spergel 2014; Baldauf et al. 2015a; Blas et al. 2016a; Ivanov & Sibiryakov 2018; Sugiyama et al. 2021).

For the bispectrum, we adopt the following IR-resummed model (Sugiyama et al. 2021):

$$\begin{aligned} B(\mathbf{k}_1, \mathbf{k}_2) &= 2Z_2(\mathbf{k}_1, \mathbf{k}_2)Z_1(\mathbf{k}_1)Z_1(\mathbf{k}_2) \\ &\times \left\{ \mathcal{D}(\mathbf{k}_1)\mathcal{D}(\mathbf{k}_2)\mathcal{D}(\mathbf{k}_3)P_w(k_1)P_w(k_2) \right. \\ &+ \mathcal{D}^2(\mathbf{k}_1)P_w(k_1)P_{\text{nw}}(k_2) + \mathcal{D}^2(\mathbf{k}_2)P_w(k_1)P_{\text{nw}}(k_2) \\ &\left. + P_{\text{nw}}(k_1)P_{\text{nw}}(k_2) \right\} + 2 \text{ perms.}, \end{aligned} \quad (3.12)$$

where  $\mathbf{k}_1 + \mathbf{k}_2 + \mathbf{k}_3 = 0$ . As in the case of the power spectrum, this bispectrum model restores the tree-level solution (2.22) consisting of a smooth version (without BAOs) of the linear power spectrum after degrading the BAO signature<sup>11</sup>.

### 3.3 Parameterization method for the bispectrum

The non-linear kernel functions  $F_2^{(\text{m})}$  and  $G_2^{(\text{m})}$  can be decomposed into three terms using Legendre polynomial functions  $\mathcal{L}_\ell(\hat{p}_1 \cdot \hat{p}_2)$ : i.e., monopole, dipole, and quadrupole components (Schmittfull et al. 2015). They are called the growth, shift, and tidal terms, and are understood in  $\Lambda$ CDM as follows: the growth term represents the spherical collapse of density fluctuations (Fosalba & Gaztanaga 1998); the shift term appears in the form  $\Psi_1^i \partial_i \delta_1$  or  $\Psi_1^i \partial_i \theta_1$  as a coordinate transformation of  $\delta$  or  $\theta$  by the displacement vector  $\Psi$ ; the last term represents the tidal force (2.16). Then,  $F_2^{(\text{m})}$  and  $G_2^{(\text{m})}$  (2.10) are rewritten as (e.g., Bouchet et al. 1992; Sherwin & Zaldarriaga 2012; Baldauf et al. 2012; Schmittfull et al. 2015)

$$\begin{aligned} F_2^{(\text{m})} &= \left( \kappa_\delta - \frac{4}{21} \lambda_\delta \right) + \kappa_\delta S(\mathbf{k}_1, \mathbf{k}_2) + \frac{2}{7} \lambda_\delta T(\mathbf{k}_1, \mathbf{k}_2), \\ G_2^{(\text{m})} &= \left( \kappa_\theta - \frac{8}{21} \lambda_\theta \right) + \kappa_\theta S(\mathbf{k}_1, \mathbf{k}_2) + \frac{4}{7} \lambda_\theta T(\mathbf{k}_1, \mathbf{k}_2), \end{aligned} \quad (3.13)$$

where  $S$  and  $T$  are the scale-dependent functions characterising the shift and tidal terms:

$$\begin{aligned} S(\mathbf{k}_1, \mathbf{k}_2) &= \frac{1}{2} (\hat{k}_1 \cdot \hat{k}_2) \left( \frac{k_1}{k_2} + \frac{k_2}{k_1} \right), \\ T(\mathbf{k}_1, \mathbf{k}_2) &= (\hat{k}_1 \cdot \hat{k}_2)^2 - \frac{1}{3}. \end{aligned} \quad (3.14)$$

As mentioned in Section 2.1, the coefficients of the growth, shift, and tidal terms are not independent of each other but are related to under the condition that  $F_2^{(\text{m})}(\mathbf{p}, -\mathbf{p}) = G_2^{(\text{m})}(\mathbf{p}, -\mathbf{p}) = 0$ . Therefore, the

<sup>11</sup> Blas et al. (2016a); Ivanov & Sibiryakov (2018) proposed a bispectrum model similar to Eq. (3.12). However, the authors ignore the  $\mathcal{O}(P_w^2/P_{\text{nw}}^2)$  term, so their model does not include the second line term,  $D(\mathbf{k}_1)D(\mathbf{k}_2)D(\mathbf{k}_3)P_w(k_1)P_w(k_2)$ , in Eq. (3.12). This term added by Sugiyama et al. (2021) contains the full tree-level solution.

coefficient of the growth term is determined from the coefficients of the shift and tidal terms.

Considering the linear and non-linear bias effects, that the second-order fluctuations are proportional to  $\sigma_8^2$ , and that  $G_2^{(m)}$  always appears with  $f$ , we introduce the following parameterisation,

$$F_2^{(g)}\sigma_8^2 = (b_1\sigma_8)[(F_g\sigma_8) + (F_s\sigma_8)S + (F_t\sigma_8)T],$$

$$fG_2^{(g)}\sigma_8^2 = (f\sigma_8)[(G_g\sigma_8) + (G_s\sigma_8)S + (G_t\sigma_8)T]. \quad (3.15)$$

DHOST theories have  $G_g = G_s - (2/3)G_t$  from the condition  $G_2^{(g)}(\mathbf{p}, -\mathbf{p}) = 0$ ; Horndeski theories further have  $F_s = G_s = 1$ . The specific form of each coefficient in DHOST theories is given by

$$F_g = \kappa_\delta - \frac{4}{21}\lambda_\delta + \frac{1}{2}\frac{b_2}{b_1},$$

$$F_s = \kappa_\delta,$$

$$F_t = \frac{2}{7}\lambda_\delta + \frac{b_s^2}{b_1},$$

$$G_g = \kappa_\theta - \frac{8}{21}\lambda_\theta,$$

$$G_s = \kappa_\theta,$$

$$G_t = \frac{4}{7}\lambda_\theta. \quad (3.16)$$

In Eq. (3.16),  $F_g$  and  $F_t$  do not contain any cosmological information because they are degenerate with the non-linear bias parameters, and  $G_g$  is determined from  $G_t$  and  $G_s$ . Thus, cosmologically meaningful parameters are  $F_s$ ,  $G_s$ , and  $G_t$ .

Following the method proposed by Sugiyama et al. (2021), we decompose the IR-resummed bispectrum model into

$$B(\mathbf{k}_1, \mathbf{k}_2) = \sum_{p=1}^{22} X^{(p)} B^{(p)}(\mathbf{k}_1, \mathbf{k}_2), \quad (3.17)$$

with

$$B^{(p)}(\mathbf{k}_1, \mathbf{k}_2) = 2 H^{(p)}(\mathbf{k}_1, \mathbf{k}_2)$$

$$\times \left\{ \mathcal{D}(\mathbf{k}_1)\mathcal{D}(\mathbf{k}_2)\mathcal{D}(\mathbf{k}_3)P_w^{(n)}(k_1)P_w^{(n)}(k_2) \right.$$

$$+ \mathcal{D}^2(\mathbf{k}_1)P_w^{(n)}(k_1)P_{nw}^{(n)}(k_2)$$

$$+ \mathcal{D}^2(\mathbf{k}_2)P_{nw}^{(n)}(k_1)P_w^{(n)}(k_2)$$

$$\left. + P_{nw}^{(n)}(k_1)P_{nw}^{(n)}(k_2) \right\} + 2 \text{ perms.}, \quad (3.18)$$

where  $P_w^{(n)}$  and  $P_{nw}^{(n)}$  are respectively the wiggle and no-wiggle linear matter power spectra normalized by  $\sigma_8^2$ :  $P_w^{(n)} = P_w/\sigma_8^2$  and  $P_{nw}^{(n)} = P_{nw}/\sigma_8^2$ . The functions  $X^{(p)}$  ( $p = 1 - 22$ ) represent the combinations of the parameters of interest and are given by

$$X^{(1)} = (F_g\sigma_8)(b_1\sigma_8)^3,$$

$$X^{(2)} = (F_s\sigma_8)(b_1\sigma_8)^3,$$

$$X^{(3)} = (F_t\sigma_8)(b_1\sigma_8)^3,$$

$$X^{(4)} = (F_g\sigma_8)(b_1\sigma_8)^2(f\sigma_8),$$

$$X^{(5)} = (F_s\sigma_8)(b_1\sigma_8)^2(f\sigma_8),$$

$$X^{(6)} = (F_t\sigma_8)(b_1\sigma_8)^2(f\sigma_8),$$

$$X^{(7)} = (F_g\sigma_8)(b_1\sigma_8)(f\sigma_8)^2,$$

$$X^{(8)} = (F_s\sigma_8)(b_1\sigma_8)(f\sigma_8)^2,$$

$$X^{(9)} = (F_t\sigma_8)(b_1\sigma_8)(f\sigma_8)^2,$$

$$X^{(10)} = (G_g\sigma_8)(b_1\sigma_8)^2(f\sigma_8),$$

$$X^{(11)} = (G_s\sigma_8)(b_1\sigma_8)^2(f\sigma_8),$$

$$X^{(12)} = (G_t\sigma_8)(b_1\sigma_8)^2(f\sigma_8),$$

$$X^{(13)} = (G_g\sigma_8)(b_1\sigma_8)(f\sigma_8)^2,$$

$$X^{(14)} = (G_s\sigma_8)(b_1\sigma_8)(f\sigma_8)^2,$$

$$X^{(15)} = (G_t\sigma_8)(b_1\sigma_8)(f\sigma_8)^2,$$

$$X^{(16)} = (G_g\sigma_8)(f\sigma_8)^3,$$

$$X^{(17)} = (G_s\sigma_8)(f\sigma_8)^3,$$

$$X^{(18)} = (G_t\sigma_8)(f\sigma_8)^3,$$

$$X^{(19)} = (b_1\sigma_8)^3(f\sigma_8),$$

$$X^{(20)} = (b_1\sigma_8)^2(f\sigma_8)^2,$$

$$X^{(21)} = (b_1\sigma_8)(f\sigma_8)^3,$$

$$X^{(22)} = (f\sigma_8)^4. \quad (3.19)$$

The scale-dependent functions  $H^{(p)}$  ( $p = 1 - 22$ ) are derived by decomposing the non-linear kernel functions  $Z_1 Z_1 Z_2$  in terms of the parameters, given by

$$H^{(1)} = 1,$$

$$H^{(2)} = S(\mathbf{k}_1, \mathbf{k}_2),$$

$$H^{(3)} = T(\mathbf{k}_1, \mathbf{k}_2),$$

$$H^{(4)} = (\mu_1^2 + \mu_2^2),$$

$$H^{(5)} = S(\mathbf{k}_1, \mathbf{k}_2)(\mu_1^2 + \mu_2^2),$$

$$H^{(6)} = T(\mathbf{k}_1, \mathbf{k}_2)(\mu_1^2 + \mu_2^2),$$

$$H^{(7)} = (\mu_1^2 \mu_2^2),$$

$$H^{(8)} = S(\mathbf{k}_1, \mathbf{k}_2)(\mu_1^2 \mu_2^2),$$

$$H^{(9)} = T(\mathbf{k}_1, \mathbf{k}_2)(\mu_1^2 \mu_2^2),$$

$$H^{(10)} = (\mu^2),$$

$$H^{(11)} = S(\mathbf{k}_1, \mathbf{k}_2)(\mu^2),$$

$$H^{(12)} = T(\mathbf{k}_1, \mathbf{k}_2)(\mu^2),$$

$$H^{(13)} = (\mu^2)(\mu_1^2 + \mu_2^2),$$

$$H^{(14)} = S(\mathbf{k}_1, \mathbf{k}_2)(\mu^2)(\mu_1^2 + \mu_2^2),$$

$$H^{(15)} = T(\mathbf{k}_1, \mathbf{k}_2)(\mu^2)(\mu_1^2 + \mu_2^2),$$

$$H^{(16)} = (\mu^2)(\mu_1^2 \mu_2^2),$$

$$H^{(17)} = S(\mathbf{k}_1, \mathbf{k}_2)(\mu^2)(\mu_1^2 \mu_2^2),$$

$$H^{(18)} = T(\mathbf{k}_1, \mathbf{k}_2)(\mu^2)(\mu_1^2 \mu_2^2),$$

$$H^{(19)} = DV(\mathbf{k}_1, \mathbf{k}_2),$$

$$H^{(20)} = DV(\mathbf{k}_1, \mathbf{k}_2)(\mu_1^2 + \mu_2^2) + V(\mathbf{k}_1, \mathbf{k}_2),$$

$$H^{(21)} = DV(\mathbf{k}_1, \mathbf{k}_2)(\mu_1^2 \mu_2^2) + V(\mathbf{k}_1, \mathbf{k}_2)(\mu_1^2 + \mu_2^2),$$

$$H^{(22)} = V(\mathbf{k}_1, \mathbf{k}_2)(\mu_1^2 \mu_2^2), \quad (3.20)$$

where  $\mathbf{k} = \mathbf{k}_1 + \mathbf{k}_2$ ,  $\mu = \hat{k} \cdot \hat{n}$ ,  $\mu_1 = \hat{k}_1 \cdot \hat{n}$ ,  $\mu_2 = \hat{k}_2 \cdot \hat{n}$ , and

$$V(\mathbf{k}_1, \mathbf{k}_2) = \frac{1}{2} \frac{k^2}{k_1 k_2} \mu^2 \mu_1 \mu_2,$$

$$DV(\mathbf{k}_1, \mathbf{k}_2) = \frac{1}{2} k \mu \left[ \frac{\mu_1}{k_1} + \frac{\mu_2}{k_2} \right]. \quad (3.21)$$

We pre-compute  $B^{(p)}(\mathbf{k}_1, \mathbf{k}_2)$  using the fiducial cosmology introduced in Section 1 and save the resulting data in a file. In this way, when constraining  $X^{(p)}$  from the BOSS data, we can quickly calculate the bispectrum by loading the data file containing  $B^{(p)}$  and substituting them into Eq. (3.17) along with  $X^{(p)}$ .

Here we demonstrate how the growth, shift, and tidal terms of the second-order density and velocity fields affect the multipole components of the 3PCF. To do so, we consider the following seven

bispectra:

$$\begin{aligned}
 B_{\text{FG}}(\mathbf{k}_1, \mathbf{k}_2) &= \sum_{p=1,4,7} X^{(p)} B^{(p)}(\mathbf{k}_1, \mathbf{k}_2), \\
 B_{\text{FS}}(\mathbf{k}_1, \mathbf{k}_2) &= \sum_{p=2,5,8} X^{(p)} B^{(p)}(\mathbf{k}_1, \mathbf{k}_2), \\
 B_{\text{FT}}(\mathbf{k}_1, \mathbf{k}_2) &= \sum_{p=3,6,9} X^{(p)} B^{(p)}(\mathbf{k}_1, \mathbf{k}_2), \\
 B_{\text{GG}}(\mathbf{k}_1, \mathbf{k}_2) &= \sum_{p=10,13,16} X^{(p)} B^{(p)}(\mathbf{k}_1, \mathbf{k}_2), \\
 B_{\text{GS}}(\mathbf{k}_1, \mathbf{k}_2) &= \sum_{p=11,14,17} X^{(p)} B^{(p)}(\mathbf{k}_1, \mathbf{k}_2), \\
 B_{\text{GT}}(\mathbf{k}_1, \mathbf{k}_2) &= \sum_{p=12,15,18} X^{(p)} B^{(p)}(\mathbf{k}_1, \mathbf{k}_2), \\
 B_{\text{BF}}(\mathbf{k}_1, \mathbf{k}_2) &= \sum_{p=19,20,21,22} X^{(p)} B^{(p)}(\mathbf{k}_1, \mathbf{k}_2). \quad (3.22)
 \end{aligned}$$

where  $B_{\text{FG}}$ ,  $B_{\text{FS}}$ ,  $B_{\text{FT}}$ ,  $B_{\text{GG}}$ ,  $B_{\text{GS}}$ , and  $B_{\text{GT}}$  are proportional to  $(F_g \sigma_8)$ ,  $(F_s \sigma_8)$ ,  $(F_t \sigma_8)$ ,  $(G_g \sigma_8)$ ,  $(G_s \sigma_8)$ , and  $(G_t \sigma_8)$ , respectively, and  $B_{\text{BF}}$  depends only on  $(b_1 \sigma_8)$  and  $(f \sigma_8)$ . When computing the above seven bispectra, we assume the cosmological parameters in  $\Lambda\text{CDM}$  given in Section 1, the linear bias parameter  $b_1 = 2$ , no non-linear bias, i.e.  $b_2 = b_{s2} = 0$ , and the redshift  $z = 0.61$ . Next, we decompose the seven bispectra using TripoSHs according to Section 3.1 and compute the 3PCF multipoles via the 2D Hankel transform (3.6). We plot the resulting 3PCF multipoles in Figures 1 and 2 as a function of  $r_2$  after fixing  $r_1$  to 50, 80, 90, 100, and  $130 h^{-1} \text{Mpc}$ .

As shown in Sugiyama et al. (2021), in the monopole component (Figure 1), the growth term (“FG”) is positive for scales smaller than  $\sim 130 h^{-1} \text{Mpc}$  and has a peak at  $r_1 = r_2$ , while it goes from positive to negative and behaves like a trough for scales above  $\sim 130 h^{-1} \text{Mpc}$ . On the other hand, the shift (“FS”) and tidal (“FT”) terms have troughs for any scale. Depending on the scale of interest, the shift term dominates for scales above  $\sim 30 h^{-1} \text{Mpc}$ , and the total 3PCF (“total”), which is the sum of all components, is found to have a trough. To illustrate the trough-like behavior of the 3PCF at  $r_1 = r_2$ , we have drawn vertical black lines representing  $r_1 = r_2$  in Figures 1 and 2. It can be seen that the bottom of the trough of the black curve representing the total 3PCF is always on the line  $r_1 = r_2$ . Around  $r_1 \sim 100 h^{-1} \text{Mpc}$ , the BAO peak appears and has a wavy shape as it cancels out the trough due to non-linear gravity effects (e.g., see the middle panels). At  $r_1 = 130 h^{-1} \text{Mpc}$  (the bottom panels), almost all the components have troughs, so the 3PCF has a more significant trough at  $r_1 = r_2$ .

The quadrupole component (Figure 2) of the 3PCF only shows an overall trough behaviour because the BAO signal is sufficiently non-linearly damped. The most dominant term in the quadrupole 3PCF is the “BF” term, which does not depend on any non-linear coefficients such as  $F_g$  or  $G_g$ . This “BF” term consists of two effects: first, a term expressed as the product of a linear density field and a linear velocity field, and second, a term expressed as the square of the linear velocity field. In particular, the former can be interpreted as a new shift term resulting from the coordinate transformation from real to redshift space (2.18), and it dominates the “BF” term. Therefore, it behaves similarly to the shift term in the monopole 3PCF and explains most of the trough structure in the quadrupole 3PCF. The growth (“GG”), shift (“GS”), and tidal (“GT”) terms in the non-linear velocity field contribute to the quadrupole 3PCF comparably to those in the non-linear density field, and thus we can use the quadrupole 3PCF to determine the “GG”, “GS”, and “GT” terms. In contrast to

the monopole case, the growth terms (“FG” and “GG”) are negative and behave as troughs, while the shift terms (“FS” and “GS”) are positive.

### 3.4 Time-dependences of parameters

We review the discussion by Yamauchi & Sugiyama (2022) on introducing new parameters to test DHOST theories and their time-dependences.

Note that some previous works predict that constraining  $\sigma_8$  alone from the 3PCF can break the degeneracy between  $f\sigma_8$  and  $\sigma_8$ , but this no longer happens in the framework of DHOST theories. To illustrate this fact in the context of our parameterisation, we can see from Eq. (3.15) that the coefficient of the shift term in the second-order density fluctuation in  $\Lambda\text{CDM}$  ( $F_s = 1$ ) determines  $\sigma_8$  because both the growth and tidal terms are degenerate with the non-linear bias parameters (Schmittfull et al. 2015). However, in the case of DHOST theories, there appears the parameter  $\kappa_\delta$  in the coefficient of the shift term, which makes it impossible to measure  $\sigma_8$  alone. Therefore, we introduce three new parameters that are not degenerate with  $\sigma_8$  following Yamauchi & Sugiyama (2022):

$$\begin{aligned}
 E_f &= \frac{f}{\kappa_\delta} = \frac{f\sigma_8}{F_s\sigma_8}, \\
 E_s &= \frac{\kappa_\theta}{\kappa_\delta} = \frac{G_s\sigma_8}{F_s\sigma_8}, \\
 E_t &= \frac{\lambda_\theta}{\kappa_\delta} = \frac{7}{4} \frac{G_t\sigma_8}{F_s\sigma_8}. \quad (3.23)
 \end{aligned}$$

In GR or Horndeski theories,  $E_f = f$ ,  $E_s = 1$  and  $E_t = \lambda_\theta$ , because  $\kappa_\delta = \kappa_\theta = 1$ . Horndeski theories differ from  $\Lambda\text{CDM}$  only in  $f$  and  $E_t$  while keeping  $E_s = 1$ . If  $E_s \neq 1$ , then the signal is specific to DHOST theories;  $E_s \neq 1$  is a sufficient condition for detecting DHOST theories because there can be DHOST theories satisfying  $E_s = 1$ .

It has been known for a long time that the coefficient of the tidal term in the non-linear density field,  $\lambda_\delta$ , is time-dependent in GR (e.g., Bouchet et al. 1992), and in the case of  $\Lambda\text{CDM}$ , the following approximation holds well with an precision better than 0.6% (Bouchet et al. 1995; Yamauchi et al. 2017b)<sup>12</sup>:

$$\lambda_\delta \sim \Omega_m^{3/572}. \quad (3.25)$$

Through Eq. (2.12), the coefficient of the tidal term in the non-linear velocity field,  $\lambda_\theta$ , is also given by (Yamauchi & Sugiyama 2022)

$$\lambda_\theta \sim \Omega_m^{15/1144}. \quad (3.26)$$

Yamauchi et al. (2017b) extended the above discussion to Horndeski theories and showed that  $\lambda_\delta$  is parameterised as a power of  $\Omega_m$  in Horndeski theories. In addition, Yamauchi & Sugiyama (2022) performed similar calculations for DHOST theories and showed that the coefficient of the shift term,  $\kappa_\delta$ , is also described by a power of  $\Omega_m$ . The coefficients of the shift and tidal terms in the non-linear velocity field can be calculated through Eq. (2.12), and they also

<sup>12</sup> The original derivation of the equation was calculated in the Lagrangian picture and is given in the form (Bouchet et al. 1995)

$$\frac{2}{7} \lambda_\delta = \frac{1}{2} \left[ 1 - \frac{3}{7} \Omega_m^{-1/143} \right]. \quad (3.24)$$

This equation can be rewritten to Eq. (3.25) under the condition  $(1 - \Omega_m) \ll 1$ .

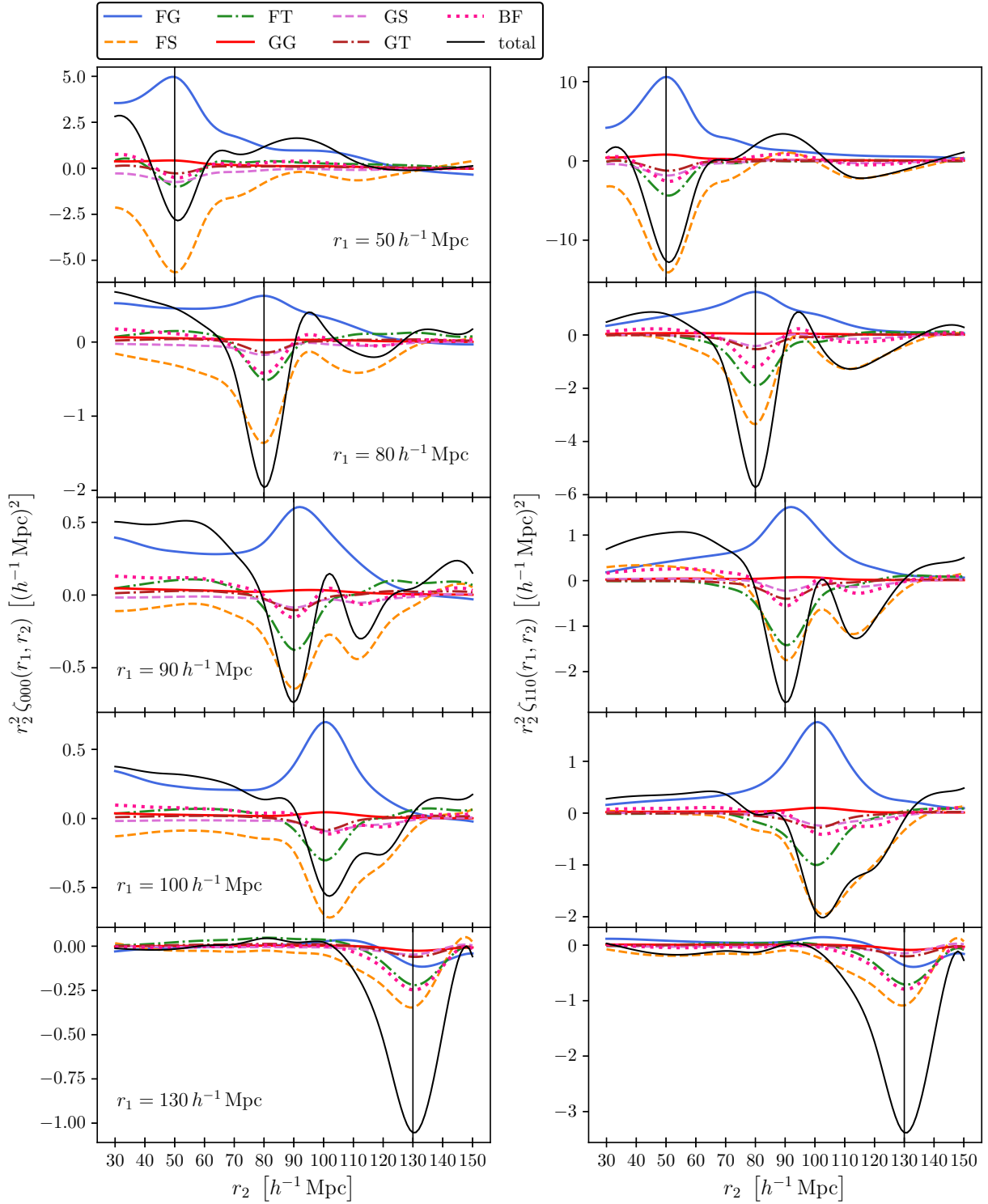


**Figure 1.** The monopole 3PCFs,  $\zeta_{000}$  (left) and  $\zeta_{110}$  (right), calculated from the decomposed bispectra (3.22) according to the parameter dependence, are shown as a function of  $r_2$  after fixing  $r_1$  to 50, 80, 90, 100, and 130  $h^{-1}$  Mpc. The “FG”, “FS”, and “FT” terms arise from the growth, shift and tidal effects of the non-linear density fluctuation; the “GG”, “GS”, and “GT” terms arise from those of the non-linear velocity field; the “BF” term consists only of linear density and linear velocity fields; the “total” term is the sum of all the decomposed components. For these calculations, the  $\Lambda$ CDM model at  $z = 0.61$ , the linear bias  $b_1 = 2.0$ , and no non-linear bias are assumed.



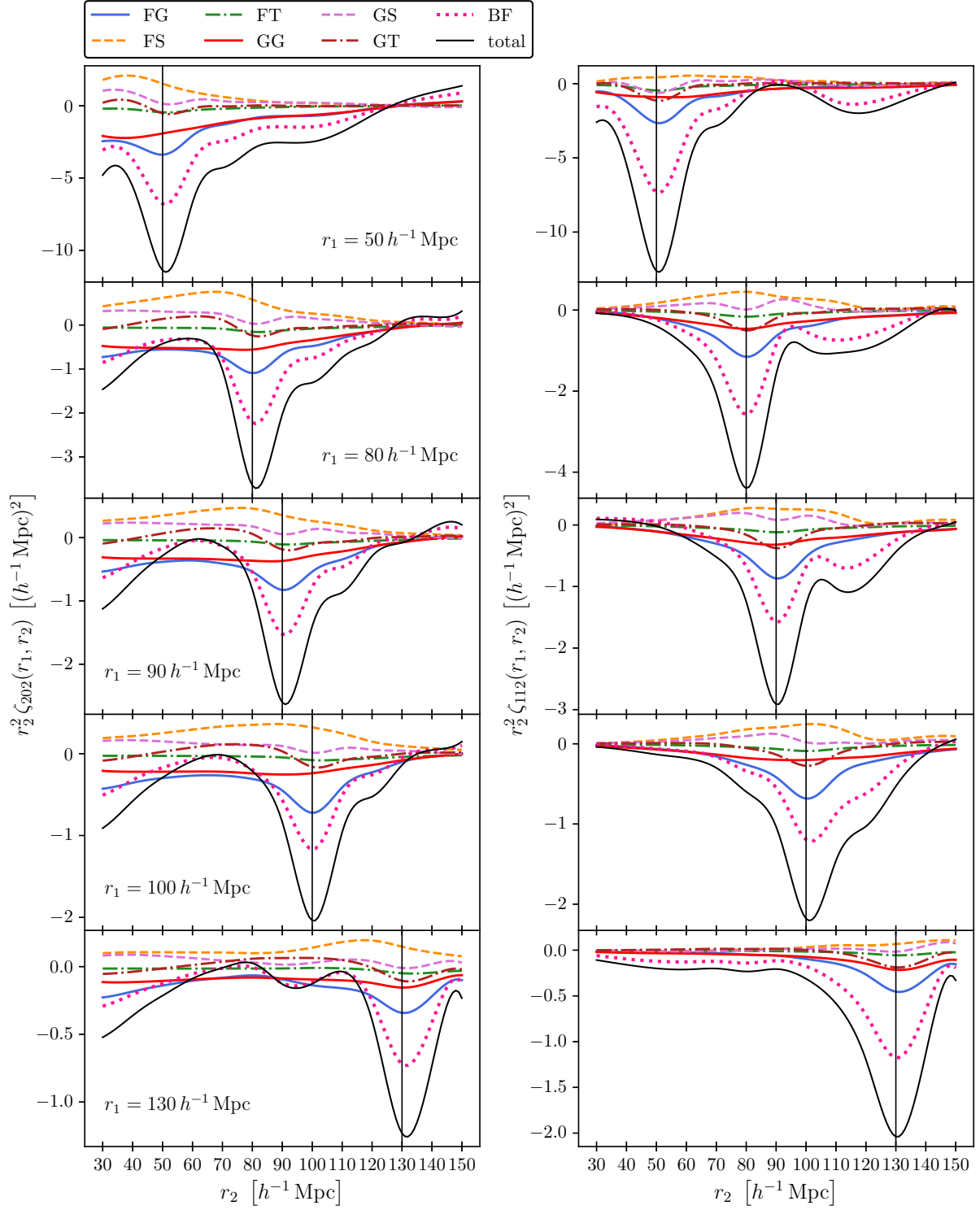


**Figure 2.** Same as Figure 1, except that the quadrupole 3PCFs,  $\zeta_{202}$  and  $\zeta_{112}$ , are shown.

follow the powers of  $\Omega_m$ . Therefore, we can parameterise the time-dependences of  $E_f$ ,  $E_s$ , and  $E_t$  as follows:

$$E_f \sim \Omega_m^{\xi_f}, \quad E_s \sim \Omega_m^{\xi_s}, \quad E_t \sim \Omega_m^{\xi_t}. \quad (3.27)$$

In GR, we have

$$\xi_f = \frac{6}{11}, \quad \xi_s = 0, \quad \xi_t = \frac{15}{1144}. \quad (3.28)$$

In summary, we parameterise the second-order kernel function of the velocity field (3.15) as

$$fG_2^{(g)}\sigma_8^2 = \Omega_m^{\xi_f} (F_s\sigma_8)^2 \left[ (G_g) + \Omega_m^{\xi_s} S + \frac{4}{7}\Omega_m^{\xi_t} T \right], \quad (3.29)$$

where  $(G_g) = \Omega_m^{\xi_s} - (8/21)\Omega_m^{\xi_t}$ , and the functions  $S$  and  $T$  are given in Eq. (3.14). We will test the theory of gravity by measuring the above three parameters,  $\xi_f$ ,  $\xi_s$ , and  $\xi_t$ , from the BOSS data in Section 9.

In DHOST theories, the Planck mass is time-varying, and the time variation of the Hubble parameter is different from GR. Therefore, one may be concerned that the time dependence of  $\Omega_m$  is different from  $\Omega_m^{\text{GR}}$  that is calculated assuming GR. However, Appendix C in Yamauchi & Sugiyama (2022) showed that the difference between DHOST theories and GR is suppressed by  $(1 - \Omega_m^{\text{GR}})$ . Hence, we can replace  $\Omega_m$  in Eq. (3.27) with  $\Omega_m^{\text{GR}}$  as an approximation and perform the analysis to constrain  $\xi_f$ ,  $\xi_s$ , and  $\xi_t$ .

### 3.5 Limitations of our theoretical approach to the 2PCF and 3PCF

In this subsection, we discuss the validity of the calculation methods of the 2PCF and 3PCF models described so far and the limitations of their application.

First, we can use the TripoSH decomposed 3PCF (3.6) to constrain all the scale dependencies in the 3PCF, such as the shift and tidal terms, as shown Figures 1 and 2, because it does not focus only on specific scale dependencies such as the squeezed limit. However, our analysis that uses only some multipoles of the TripoSH decomposition does not fully utilize the information on the scale dependence of the 3PCF. The reason for restricting the multipole components used in this work is to keep the number of data bins much smaller than the number of mock simulations used to compute the covariance matrix (Section 5). Therefore, increasing the number of multipoles in the 3PCF to be considered will improve the results of this work when more mock catalogues are created in the future.

Second, note that the power spectrum and bispectrum models in Eqs. (3.9) and (3.12) are valid for any theory in which the IR cancellation occurs based on the Galilean invariance of the system of equations in the IR limit: i.e., these models hold not only for  $\Lambda$ CDM but also for Horndeski theories (Crisostomi et al. 2020). On the other hand, as Lewandowski (2020) pointed out in the power spectrum case, additional terms arise when performing the IR resummation in DHOST theories because of the violation of the IR cancellation. Specifically, when one applies the IR limit to the one-loop solution of the power spectrum in DHOST theories, a term proportional to  $k^2 P_{\text{lin}}(k)$  appears, changing the shape of the power spectrum (Crisostomi et al. 2020; Lewandowski 2020; Hirano et al. 2020). Note also that this additional term is degenerate with the higher-order derivative bias, which is ignored in this paper. However, since this additional term in the IR limit is proportional to  $k^2 P_{\text{lin}}(k)$ , it is considered to be negligible at the large scales of interest in this paper ( $\geq 80 h^{-1}$  Mpc). Assuming that the same should happen in

the bispectrum, we directly use the power and bispectrum models in Eqs. (3.9) and (3.12) in the present analysis. In addition, it should be noted that Hirano et al. (2020) showed that in DHOST theories, a term consisting of the product of first- and third-order fluctuations in the one-loop power spectrum causes UV divergence. Further model development is thus needed to take advantage of smaller-scale information by solving these problems.

Third, since the linear equation for density fluctuations is scale-independent (2.6), we assume that we can use the shape of the linear matter power spectrum determined in the high- $z$  region, where the scalar field is expected to be sub-dominant. Thus, we can pre-compute the  $\sigma_8^2$ -normalized wiggle and no-wiggle power spectra,  $P_w^{(n)}$  and  $P_{\text{nw}}^{(n)}$ , appearing in the  $B^{(p)}$  terms (3.18), using a  $\Lambda$ CDM model.

Fourth, there is a concern about the pre-computation of  $\mathcal{D}(\mathbf{k})$  (3.10) appearing in the  $B^{(p)}$  terms (3.18). It is known that  $\sigma_{\perp}$  and  $\sigma_{\parallel}$ , which characterise  $\mathcal{D}(\mathbf{k})$ , can be calculated successfully using linear displacement vectors (e.g., Matsubara 2008), and we adopt the same calculation in this paper (3.11). Since  $\sigma_{\perp}$  and  $\sigma_{\parallel}$  in the linear theory depend on  $f$  and  $\sigma_8$ , their values should differ for different gravity theories. For this reason, it is desirable to vary  $\sigma_{\perp}$  and  $\sigma_{\parallel}$  as free parameters in the data analysis. However, to do so, the bispectrum decomposition method in Eq. (3.17) cannot be applied, and the computation time of the bispectrum model increases significantly, making it challenging to perform cosmological analysis. Fortunately, the BAO signal does not significantly impact the shape of the 3PCF. The reason is that the BAO signal is maximized when  $r_1 \sim r_2 \sim 100 h^{-1}$  Mpc, while  $r_1$  and  $r_2$  can take various combinations in the 3PCF (Sugiyama et al. 2021). Therefore, in this paper, we ignore the concern about  $\mathcal{D}(\mathbf{k})$  and pre-compute  $\sigma_{\perp}$  and  $\sigma_{\parallel}$  using the linear theory in  $\Lambda$ CDM. Furthermore, to keep consistency with the 3PCF calculation, we fix  $\sigma_{\perp}$  and  $\sigma_{\parallel}$  to those calculated using the  $\Lambda$ CDM model in the 2PCF calculation as well.

Finally, to simplify the analysis, we ignore the AP effect (Alcock & Paczyński 1979), which can directly measure the Hubble parameter and angular radial distance at the redshift of the galaxy distribution of interest. Ignoring the AP effect means that the values of the angular diameter distance and the Hubble parameter, which should be constrained by the AP effect, are given by the fiducial  $\Lambda$ CDM. In this sense, this paper assumes the fiducial  $\Lambda$ CDM for the expansion of the Universe in the background spacetime. However, the AP effect can be determined by the 2PCF by a few percent and is not expected to significantly affect the constraint results for the parameters that characterize the nonlinear fluctuations of interest in this paper, such as  $\xi_t$  and  $\xi_s$ . Since DHOST theories vary these parameter values, the AP effect is expected to provide further information into the constraint on DHOST theories. Sugiyama et al. (2021) have performed a joint analysis of the anisotropic 2PCF and 3PCF to constrain the AP parameters under the GR assumption. Combining that method with the analysis method developed in this paper allows for consistent DHOST theory constraints that simultaneously account for the AP and nonlinear gravity effects, which is left as future work.

## 4 MEASUREMENTS

This section summarises how to measure multipole 2PCFs and 3PCFs from BOSS galaxy data according to the method proposed by Sugiyama et al. (2021). First, Section 4.1 introduces the BOSS galaxy data used in this paper and the mock simulation data designed to reproduce it. Then, Section 4.2 describes the measurements of the multipole 2PCFs and 3PCFs. Finally, Section 4.3 explains how to

correct for the window function effects on the measured 2PCF and 3PCF.

#### 4.1 Data

We use the final galaxy clustering data set, Data Release 12 (DR12; Alam et al. 2015), from the Baryon Oscillation Spectroscopic Survey (BOSS; Dawson et al. 2013). The BOSS survey is part of the Sloan Digital Sky Survey III (SDSS III Eisenstein et al. 2011), selected galaxies from multicolour SDSS imaging (Fukugita et al. 1996; Gunn et al. 1998; Smith et al. 2002; Gunn et al. 2006; Doi et al. 2010) and used the SDSS multi-fibre spectrograph (Bolton et al. 2012; Smee et al. 2013) to measure spectroscopic redshifts of the galaxies. As detailed in Reid et al. (2016), the BOSS survey has four samples, CMASS, LOWZ, LOWZ2 and LOWZ3, and those four samples are combined into one sample. In brief, the survey footprint, veto masks and survey-related systematics (such as fibre collisions and redshift failures) are considered to construct data and random catalogues for the DR12 BOSS galaxies. This DR12 combined sample comprises 1.2 million massive galaxies over an effective area of  $9329 \text{ deg}^2$  and covers a redshift range of  $0.2 - 0.75$ . In our analysis, we split this redshift range into two redshift bins defined by  $0.2 < z < 0.5$  and  $0.5 < z < 0.75$  with the effective redshifts  $z_{\text{eff}} = 0.38$  and  $0.61$ , respectively, where the effective redshifts are calculated as the weighted average over all galaxies (see e.g. Eq. (67) in Beutler et al. 2014). The DR12 combined sample is observed across the two Galactic hemispheres, referred to as the Northern and Southern galactic caps (NGC and SGC, respectively), and the NGC and SGC samples probe slightly different galaxy populations in the low-redshift part of the combined sample (see Appendix A in Alam et al. 2015).

To derive the covariance matrices of the 2PCF and 3PCF and test the validity of the 2PCF and 3PCF models given in Eqs. (3.9) and (3.12), we use the MultiDark-Patchy mock catalogues (Patchy mocks; Kitaura et al. 2016). The Patchy mocks have been calibrated to an  $N$ -body simulation-based reference sample using approximate galaxy solvers and analytical-statistical biasing models and incorporate observational effects including the survey geometry, veto mask and fiber collisions. The reference catalogue is extracted from one of the BigMultiDark simulations (Klypin et al. 2016), which was performed using GADGET-2 (Springel 2005) with  $3840^3$  particles on a volume of  $(2.5 h^{-1} \text{ Mpc})^3$ . Halo abundance matching is used to reproduce the observed BOSS two and three-point clustering measurements (Rodríguez-Torres et al. 2016). There are 2048 catalogues available for each the NGC and SGC over the redshift range  $z = 0.2 - 0.75$ . The fiducial cosmology for these mocks assumes a  $\Lambda$ CDM cosmology with  $(\Omega_\Lambda, \Omega_m, \Omega_b, \sigma_8, h) = (0.692885, 0.307115, 0.048206, 0.8288, 0.6777)$ . These fiducial parameters are slightly different from those used in our analysis of the BOSS galaxy data introduced in the introduction (Section 1), but we expect that such differences do not significantly affect the covariance matrix estimations of the 2PCF and 3PCF.

We include three different incompleteness weights to account for shortcomings of the BOSS dataset: a fiber collision weight,  $w_{\text{cp}}$ , a redshift failure weight,  $w_{\text{noz}}$ , and a systematics weight,  $w_{\text{sys}}$ , which is a combination of a stellar density weight and a seeing condition weight. Each galaxy observed at position  $\mathbf{x}$  is counted with the following weight (Ross et al. 2012; Anderson et al. 2014; Reid et al. 2016):

$$w_c(\mathbf{x}) = w_{\text{sys}}(\mathbf{x}) (w_{\text{cp}}(\mathbf{x}) + w_{\text{noz}}(\mathbf{x}) - 1). \quad (4.1)$$

In addition, we use a signal-to-noise weight, the so-called FKP

weight, proposed by Feldman et al. (1994),  $w_{\text{FKP}}(\mathbf{x}) = 1/[1 + \bar{n}_0(\mathbf{x})\bar{P}]$ , where  $\bar{P} = 10^4 (h^{-1} \text{ Mpc})^3$ . The FKP weight function is effective not only for the power spectrum but also for the bispectrum when assuming Gaussian errors (Scoccimarro 2000), and bispectrum measurements from the Patchy mock catalogue confirm that the FKP weight improves the bispectrum signal-to-noise ratio even when including non-Gaussian errors (see Appendix D in Sugiyama et al. 2019). We expect the validity of the FKP weight to hold for the 2PCF and 3PCF in configuration space because we measure the 2PCF and 3PCF as Fourier transforms of the power spectrum and bispectrum, respectively (Section 4.2). For the galaxy data, multiplying the completeness weights by the FKP weights yields the local weight function that is used in our analysis, while the random catalogues have only the FKP weights:

$$\begin{aligned} w^{(\text{gal})}(\mathbf{x}) &= w_c(\mathbf{x}) w_{\text{FKP}}(\mathbf{x}), \\ w^{(\text{ran})}(\mathbf{x}) &= w_{\text{FKP}}(\mathbf{x}), \end{aligned} \quad (4.2)$$

where the superscripts, “(gal)” and “(ran)”, stand for “galaxy” and “random”.

#### 4.2 Estimators of the 2PCF and 3PCF

We measure the number densities of both real and random galaxies weighted by the spherical harmonic function  $Y_{\ell m}$ :

$$\begin{aligned} D_{\ell m}(\mathbf{x}) &= \sum_i^{N_{\text{gal}}} w^{(\text{gal})}(\mathbf{x}_i) Y_{\ell m}^* \left( \hat{x}_i^{(\text{gal})} \right) \delta_{\text{D}} \left( \mathbf{x} - \mathbf{x}_i^{(\text{gal})} \right), \\ R_{\ell m}(\mathbf{x}) &= \sum_j^{N_{\text{ran}}} w^{(\text{ran})}(\mathbf{x}_j) Y_{\ell m}^* \left( \hat{x}_j^{(\text{ran})} \right) \delta_{\text{D}} \left( \mathbf{x} - \mathbf{x}_j^{(\text{ran})} \right), \end{aligned} \quad (4.3)$$

where  $N_{\text{gal}}$  and  $N_{\text{ran}}$  are the total number of real and random galaxies, respectively, and the normal number densities are given by  $D(\mathbf{x}) = \sqrt{4\pi} D_{00}(\mathbf{x})$  and  $R(\mathbf{x}) = \sqrt{4\pi} R_{00}(\mathbf{x})$ . Defining  $N'_{\text{gal}} \equiv \int d^3x D(\mathbf{x})$  and  $N'_{\text{ran}} \equiv \int d^3x R(\mathbf{x})$ , we can estimate the survey volume as

$$V = \frac{N_{\text{ran}}'^2}{\int d^3x [R(\mathbf{x})]^2}. \quad (4.4)$$

Then, the observed density fluctuation weighted by  $Y_{\ell m}$  is

$$\delta_{\text{obs}, \ell m}(\mathbf{x}) = V [D_{\ell m}(\mathbf{x})/N'_{\text{gal}} - R_{\ell m}(\mathbf{x})/N'_{\text{ran}}], \quad (4.5)$$

and

$$\delta_{\text{obs}}(\mathbf{x}) = \sqrt{4\pi} \delta_{\text{obs}, 00}(\mathbf{x}). \quad (4.6)$$

We use the fast Fourier transform (FFT) algorithm<sup>13</sup> to calculate

$$\tilde{\delta}_{\text{obs}, \ell m}(\mathbf{k}) = \frac{1}{W_{\text{mass}}(\mathbf{k})} \int d^3x e^{-i\mathbf{k}\cdot\mathbf{x}} \delta_{\text{obs}, \ell m}(\mathbf{x}), \quad (4.7)$$

where the Fourier transform of the normal density fluctuation is given by  $\tilde{\delta}_{\text{obs}}(\mathbf{k}) = \sqrt{4\pi} \tilde{\delta}_{\text{obs}, 00}(\mathbf{k})$ , and  $W_{\text{mass}}(\mathbf{k})$  is the mass assignment function that corrects for the effect when arising assign particles on a regular grid in position space (Jing 2005). The most popular mass assignment function is given by (Hockney & Eastwood 1981)

$$W_{\text{mass}}(\mathbf{k}) = \prod_{i=x,y,z} \left[ \text{sinc} \left( \frac{\pi k_i}{2k_{N,i}} \right) \right]^p, \quad (4.8)$$

where  $k_{N,i}$  is the Nyquist frequency of  $i$ -axis with the grid spacing  $H_i$  on the axis. The indexes  $p = 1$ ,  $p = 2$ , and  $p = 3$  correspond to the

<sup>13</sup> <http://fftw.org/>

nearest grid point (NGP), cloud-in-cell (CIC), and triangular-shaped cloud (TSC) assignment functions, respectively.

The FFT-based estimator of the multipole 2PCFs is given by (Hand et al. 2017; Sugiyama et al. 2018) (see also Bianchi et al. 2015; Scoccimarro 2015)

$$\begin{aligned} \hat{\xi}_\ell(r) &= \frac{(4\pi)}{V} \sum_m \int \frac{d^2\hat{r}}{4\pi} Y_{\ell m}(\hat{r}) \int \frac{d^3k}{(2\pi)^3} e^{ik\cdot r} \\ &\times \left[ \tilde{\delta}_{\text{obs},\ell m}(\mathbf{k}) \tilde{\delta}_{\text{obs}}^*(\mathbf{k}) - S_{\ell m}(\mathbf{k}) \right]. \end{aligned} \quad (4.9)$$

The shot-noise term  $S_{\ell m}(\mathbf{k})$  is given by

$$\begin{aligned} S_{\ell m}(\mathbf{k}) &= \frac{C_{\text{shot}}(\mathbf{k})}{W_{\text{mass}}^2(\mathbf{k})} \left( \frac{V}{N'_{\text{gal}}} \right)^2 \\ &\times \left[ \sum_i^{N_{\text{gal}}} \left[ w^{(\text{gal})}(\mathbf{x}_i) \right]^2 Y_{\ell m}^* \left( \hat{\mathbf{x}}_i^{(\text{gal})} \right) \right. \\ &\left. + \left( \frac{N'_{\text{gal}}}{N'_{\text{ran}}} \right)^2 \sum_j^{N_{\text{ran}}} \left[ w^{(\text{ran})}(\mathbf{x}_j) \right]^2 Y_{\ell m}^* \left( \hat{\mathbf{x}}_j^{(\text{ran})} \right) \right] \end{aligned} \quad (4.10)$$

where  $C_{\text{shot}}(\mathbf{k})$  represents the correction for the assignment effect to the shot-noise term, given by (Eq. (20) in Jing 2005)

$$\begin{aligned} C_{\text{shot}}(\mathbf{k}) &= \begin{cases} 1, & \text{NGP;} \\ \prod_i \left[ 1 - \frac{2}{3} \sin^2 \left( \frac{\pi k_i}{2k_{N,i}} \right) \right], & \text{CIC;} \\ \prod_i \left[ 1 - \sin^2 \left( \frac{\pi k_i}{2k_{N,i}} \right) + \frac{2}{15} \sin^4 \left( \frac{\pi k_i}{2k_{N,i}} \right) \right], & \text{TSC.} \end{cases} \end{aligned} \quad (4.11)$$

The angle integral  $\int d^2\hat{r}/(4\pi)$  in Eq. (4.9) can be rewritten as

$$\int \frac{d^2\hat{r}}{4\pi} = \frac{1}{N_r(r)} \sum_{r-\Delta r/2 < r < r+\Delta r/2}, \quad (4.12)$$

where  $\Delta r$  is the width of the  $r$ -bins, and  $N_r(r)$  is the number of three-dimensional data contained in each  $r$ -bin width. From the expression of the shot noise term in the 2PCF given in Eq. (4.10), we compute the weighted mean number density as

$$\bar{n} = \left\{ \frac{V}{N'^2_{\text{gal}}} \sum_i^{N_{\text{gal}}} \left[ w^{(\text{gal})}(\mathbf{x}_i) \right]^2 \right\}^{-1}. \quad (4.13)$$

The FFT-based estimator of the multipole 3PCFs is given by (Sugiyama et al. 2019) (see also Scoccimarro 2015; Slepian & Eisenstein 2016)

$$\begin{aligned} \hat{\zeta}_{\ell_1\ell_2\ell}(r_1, r_2) &= \frac{(4\pi)^2 h_{\ell_1\ell_2\ell}}{V} \sum_{m_1 m_2 m} \begin{pmatrix} \ell_1 & \ell_2 & \ell \\ m_1 & m_2 & m \end{pmatrix} \\ &\times \left[ \int d^3x F_{\ell_1 m_1}(\mathbf{x}; r_1) F_{\ell_2 m_2}(\mathbf{x}; r_2) G_{\ell m}(\mathbf{x}) \right. \\ &\left. - \delta_{r_1 r_2}^{(\text{K})} S_{\ell_1 m_1; \ell_2 m_2; \ell m}(r_1) \right], \end{aligned} \quad (4.14)$$

where

$$\begin{aligned} F_{\ell m}(\mathbf{x}; r) &= i^\ell \int \frac{d^3k}{(2\pi)^3} e^{ik\cdot x} j_\ell(rk) Y_{\ell m}^*(\hat{k}) \tilde{\delta}_{\text{obs}}(\mathbf{k}), \\ G_{\ell m}(\mathbf{x}) &= \int \frac{d^3k}{(2\pi)^3} e^{ik\cdot x} \tilde{\delta}_{\text{obs},\ell m}(\mathbf{k}). \end{aligned} \quad (4.15)$$

Note that the shot-noise term only contributes to the 3PCF measurement for the  $r_1 = r_2$  bins, represented by the Kronecker delta  $\delta_{r_1 r_2}^{(\text{K})}$

in Eq. (4.14). To specifically calculate the shot-noise term in the 3PCF, we first measure the following density field

$$\begin{aligned} N(\mathbf{x}) &= \sum_i^{N_{\text{gal}}} \left[ w_i^{(\text{gal})}(\mathbf{x}_i) \right]^2 \delta_{\text{D}}(\mathbf{x} - \mathbf{x}_i^{(\text{gal})}) \\ &+ \left( \frac{N'_{\text{gal}}}{N'_{\text{ran}}} \right)^2 \sum_i^{N_{\text{ran}}} \left[ w_i^{(\text{ran})}(\mathbf{x}_i) \right]^2 \delta_{\text{D}}(\mathbf{x} - \mathbf{x}_i^{(\text{ran})}), \end{aligned} \quad (4.16)$$

and divide it by  $(N'_{\text{gal}}/V)$  to have

$$\delta_{\text{N}}(\mathbf{x}) = (V/N'_{\text{gal}}) N(\mathbf{x}). \quad (4.17)$$

Then, we calculate the Fourier transform of  $\delta_{\text{N}}(\mathbf{x})$  in the same manner as in Eq. (4.7) and denote it as  $\tilde{\delta}_{\text{N}}(\mathbf{k})$ . Finally, we derive  $S_{\ell_1 m_1; \ell_2 m_2; \ell m}(r)$  by substituting  $\tilde{\delta}_{\text{N}}(\mathbf{k})$  into the following equation

$$\begin{aligned} S_{\ell_1 m_1; \ell_2 m_2; \ell m}(r) &= \left( \frac{1}{4\pi r^2 \Delta r} \right) \left( \frac{V}{N'_{\text{gal}}} \right) (-1)^{\ell_1 + \ell_2} \\ &\times \int \frac{d^2\hat{r}}{4\pi} Y_{\ell_1 m_1}^*(\hat{r}) Y_{\ell_2 m_2}^*(\hat{r}) \int \frac{d^3k}{(2\pi)^3} e^{ik\cdot r} \\ &\times \left[ \tilde{\delta}_{\ell m}(\mathbf{k}) \tilde{\delta}_{\text{N}}^*(\mathbf{k}) - S_{\ell m}^{(3\text{PCF})}(\mathbf{k}) \right], \end{aligned} \quad (4.18)$$

where

$$\begin{aligned} S_{\ell m}^{(3\text{PCF})}(\mathbf{k}) &= \frac{C_{\text{shot}}(\mathbf{k})}{W_{\text{mass}}^2(\mathbf{k})} \left( \frac{V}{N'_{\text{gal}}} \right)^2 \\ &\times \left[ \sum_i^{N_{\text{gal}}} \left[ w^{(\text{gal})}(\mathbf{x}_i) \right]^3 Y_{\ell m}^* \left( \hat{\mathbf{x}}_i^{(\text{gal})} \right) \right. \\ &\left. - \left( \frac{N'_{\text{gal}}}{N'_{\text{ran}}} \right)^3 \sum_j^{N_{\text{ran}}} \left[ w^{(\text{ran})}(\mathbf{x}_j) \right]^3 Y_{\ell m}^* \left( \hat{\mathbf{x}}_j^{(\text{ran})} \right) \right] \end{aligned} \quad (4.19)$$

The factor  $(1/(4\pi r^2 \Delta r))$  can be rewritten as

$$\frac{1}{4\pi r^2 \Delta r} = \frac{1}{N_r(r)} \frac{N_{\text{grid}}}{V_{\text{FFT}}}, \quad (4.20)$$

where  $V_{\text{FFT}}$  is the volume of the Cartesian box in which the galaxies are placed before the FFT is performed, and  $N_{\text{grid}}$  is the number of FFT grid cells.

In the scale range of  $80 \leq r \leq 150 h^{-1}$  Mpc, we choose  $\Delta r = 5 h^{-1}$  Mpc for the 2PCF and  $\Delta r = 10 h^{-1}$  Mpc for the 3PCF. Considering  $\zeta_{\ell_1\ell_2\ell}(r_1, r_2) = \zeta_{\ell_2\ell_1\ell}(r_2, r_1)$ , the numbers of data bins for the 2PCF and 3PCF multipoles are 15, 15, 36, 36, 64, and 36 for  $\xi_0, \xi_2, \zeta_{000}, \zeta_{110}, \zeta_{202}$ , and  $\zeta_{112}$ , respectively.

We use the Cartesian coordinates  $\mathbf{x} = \{x, y, z\}$  with the  $z$ -axis pointing to the north pole to define a cuboid of dimension  $L[h^{-1} \text{Mpc}] = (L_x, L_y, L_z)$  containing the galaxy sample; to perform the FFT, each axis of this cuboid is delimited into  $N = (N_x, N_y, N_z)$  grids. We then distribute the galaxies on the FFT grid using the TSC assignment function. We adopt the same values for  $L$  and  $N$  that were used by the Fourier space analysis of the two-point statistics performed by Beutler et al. (2017). They are chosen so that the width of each grid is  $\sim 5 h^{-1}$  Mpc, which is well below the scales  $r \geq 80 h^{-1}$  Mpc that we are interested in. We summarise the specific values of  $L$  and  $N$ , as well as the survey volume (4.4) and the weighted mean number density (4.13) computed using these values of  $L$  and  $N$  in Table 1.

### 4.3 Window function corrections

When measuring 2PCFs and 3PCFs in configuration space from galaxy data, if we directly measure their angle-averaged multipole



	$(L_x, L_y, L_z) [h^{-1} \text{Mpc}]$	$(N_x, N_y, N_z)$	$V [(h^{-1} \text{Gpc})^3]$	$\bar{n}/10^{-4} [(h^{-1} \text{Mpc})^{-3}]$
NGC at $z_{\text{eff}} = 0.38$ ( $0.2 < z < 0.5$ )	(1350, 2450, 1400)	(250, 460, 260)	1.51	2.65
SGC at $z_{\text{eff}} = 0.38$ ( $0.2 < z < 0.5$ )	(1000, 1900, 1100)	(190, 360, 210)	0.56	2.88
NGC at $z_{\text{eff}} = 0.61$ ( $0.5 < z < 0.75$ )	(1800, 3400, 1900)	(340, 650, 360)	2.35	1.37
SGC at $z_{\text{eff}} = 0.61$ ( $0.5 < z < 0.75$ )	(1000, 2600, 1500)	(190, 500, 280)	0.87	1.29

**Table 1.** The length of each side of the cube containing the observed galaxies, defined for performing FFTs, and the number of grids on which the cube is delimited are shown for the four BOSS samples (Section 4.1). Also shown are the survey volume (4.4) and the mean galaxy number density (4.13), calculated using the values of these parameters.

components, we can not eliminate the effect of the window function (Appendix A in Sugiyama et al. 2021). The FFT-based estimators introduced in Section (4.2) are a typical example of this, but even when measuring multipole 3PCFs without using the FFT, we need to be aware of the window function effect (Slepian & Eisenstein 2015, 2018). Since the window function  $W(\mathbf{x})$  characterising the geometry of the observed region can be estimated as  $W(\mathbf{x}) = (V/N'_{\text{ran}})R(\mathbf{x})$ , we can quantitatively estimate the corrections due to the window function by measuring the multipole 2PCFs and 3PCFs from the random catalogue.

For the 2PCF, we compute

$$Q_\ell(r) = \frac{(4\pi)}{V} \sum_m \int \frac{d^2 \hat{r}}{4\pi} Y_{\ell m}(\hat{r}) \int \frac{d^3 k}{(2\pi)^3} e^{i\mathbf{k}\cdot\mathbf{r}} \times \left[ \widetilde{W}_{\ell m}(\mathbf{k}) \widetilde{W}^*(\mathbf{k}) - S_{\ell m}^{(w)}(\mathbf{k}) \right]. \quad (4.21)$$

where  $\widetilde{W}_{\ell m}(\mathbf{k})$  is the Fourier transform of  $(V/N'_{\text{ran}})R_{\ell m}(\mathbf{x})$  computed in the same manner as in Eq. (4.7),  $\widetilde{W}(\mathbf{k}) = \sqrt{4\pi} \widetilde{W}_{00}(\mathbf{k})$ , and the shot-noise term is given by

$$S_{\ell m}^{(w)}(\mathbf{k}) = \frac{C_{\text{shot}}(\mathbf{k})}{W_{\text{mass}}^2(\mathbf{k})} \left( \frac{V}{N'_{\text{ran}}} \right)^2 \times \left[ \sum_i^{N_{\text{ran}}} \left[ w^{(\text{ran})}(\mathbf{x}_i) \right]^2 Y_{\ell m}^* \left( \hat{\mathbf{x}}_i^{(\text{ran})} \right) \right]. \quad (4.22)$$

Then, we have the theoretical model of  $\xi_\ell(r)$  taking the survey window effect into account as follows (Wilson et al. 2017; Beutler et al. 2017):

$$\xi_\ell^{(w)}(r) = (2\ell + 1) \sum_{\ell_1 \ell_2} \binom{\ell}{\ell_1 \ell_2} Q_{\ell_1}(r) \xi_{\ell_2}(r). \quad (4.23)$$

For the 3PCF, we compute

$$Q_{\ell_1 \ell_2 \ell}(r_1, r_2) = \frac{(4\pi)^2 h_{\ell_1 \ell_2 \ell}}{V} \sum_{m_1 m_2 m} \binom{\ell}{m_1 m_2 m} \times \left[ \int d^3 x F_{\ell_1 m_1}^{(w)}(\mathbf{x}; r_1) F_{\ell_2 m_2}^{(w)}(\mathbf{x}; r_2) G_{\ell m}^{(w)}(\mathbf{x}) - \delta_{r_1 r_2}^{(K)} S_{\ell_1 m_1; \ell_2 m_2; \ell m}^{(w)}(r_1) \right], \quad (4.24)$$

where

$$F_{\ell m}^{(w)}(\mathbf{x}; r) = i^\ell \int \frac{d^3 k}{(2\pi)^3} e^{i\mathbf{k}\cdot\mathbf{x}} j_\ell(kr) Y_{\ell m}^*(\hat{k}) \widetilde{W}(\mathbf{k}),$$

$$G_{\ell m}^{(w)}(\mathbf{x}) = \int \frac{d^3 k}{(2\pi)^3} e^{i\mathbf{k}\cdot\mathbf{x}} \widetilde{W}_{\ell m}(\mathbf{k}). \quad (4.25)$$

The shot-noise term is given by

$$S_{\ell_1 m_1; \ell_2 m_2; \ell m}^{(w)}(r) = \left( \frac{1}{4\pi r^2 \Delta r} \right) \left( \frac{V}{N'_{\text{ran}}} \right) (-1)^{\ell_1 + \ell_2} \times \int \frac{d^2 \hat{r}}{4\pi} Y_{\ell_1 m_1}^*(\hat{r}) Y_{\ell_2 m_2}^*(\hat{r}) \int \frac{d^3 k}{(2\pi)^3} e^{i\mathbf{k}\cdot\mathbf{r}} \times \left[ \widetilde{W}_{\ell m}(\mathbf{k}) \widetilde{\delta}_N^{(w)*}(\mathbf{k}) - S_{\ell m}^{(3\text{PCF}, w)}(\mathbf{k}) \right] \quad (4.26)$$

where

$$S_{\ell m}^{(3\text{PCF}, w)}(\mathbf{k}) = \frac{C_{\text{shot}}(\mathbf{k})}{W_{\text{mass}}^2(\mathbf{k})} \left( \frac{V}{N'_{\text{ran}}} \right)^2 \times \left[ \sum_i^{N_{\text{ran}}} \left[ w^{(\text{ran})}(\mathbf{x}_i) \right]^3 Y_{\ell m}^* \left( \hat{\mathbf{x}}_i^{(\text{ran})} \right) \right], \quad (4.27)$$

and  $\widetilde{\delta}_N^{(w)}(\mathbf{k})$  is the Fourier transform of

$$\delta_N^{(w)}(\mathbf{x}) = \left( \frac{V}{N'_{\text{ran}}} \right) \sum_i^{N_{\text{ran}}} \left[ w_i^{(\text{ran})} \right]^2 \delta_D(\mathbf{x} - \mathbf{x}_i^{(\text{ran})}). \quad (4.28)$$

Then, we have the theoretical model of  $\zeta_{\ell_1 \ell_2 \ell}(r_1, r_2)$  taking the survey window effect into account as follows (Sugiyama et al. 2019; Sugiyama et al. 2021):

$$\zeta_{\ell_1 \ell_2 \ell}^{(w)}(r_1, r_2) = (4\pi) \sum_{\ell'_1 + \ell'_2 + \ell' = \text{even}} \sum_{\ell''_1 + \ell''_2 + \ell'' = \text{even}} \times \left\{ \begin{matrix} \ell'_1 & \ell'_2 & \ell' \\ \ell_1 & \ell_2 & \ell \end{matrix} \right\} \left[ \frac{h_{\ell_1 \ell_2 \ell} h_{\ell_1 \ell'_1 \ell'_2} h_{\ell_2 \ell'_2 \ell'_1} h_{\ell \ell' \ell''}}{h_{\ell'_1 \ell'_2 \ell'} h_{\ell'_1 \ell'_2 \ell''}} \right] \times Q_{\ell'_1 \ell'_2 \ell''}(r_1, r_2) \zeta_{\ell_1 \ell_2 \ell'}(r_1, r_2), \quad (4.29)$$

where the bracket with 9 multipole indices,  $\{\dots\}$ , denotes the Wigner-9j symbol. In the likelihood fitting performed in Section 9, we use  $\xi_\ell^{(w)}$  and  $\zeta_{\ell_1 \ell_2 \ell}^{(w)}$  to compare the measured multipole 2PCF and 3PCF estimators with the theoretical models given in Eqs. (3.9) and (3.12). In this paper, we ignore the contribution from the integral constraint (Peacock & Nicholson 1991) for both the 2PCF and the 3PCF.

In the 2PCF case, the correction equation for the window function effect shown in Eq. (4.23) calculates only the three multipole components for both  $Q_{\ell_1}$  and  $\xi_{\ell_2}$ , i.e.,  $\ell_1, \ell_2 = 0, 2, 4$ . The reason is that our analysis focuses only on large scales above  $80 h^{-1} \text{Mpc}$ , where the linear theory is dominant, and the linear Kaiser effect gives only up to the hexadecapole  $\ell = 4$ . For the window correction formula of the 3PCF (4.29), Sugiyama et al. (2021) examined in detail which multipole components contribute to the observed estimator (4.14) and to what extent, for the NGC sample at  $0.4 < z < 0.6$ , and showed that a finite number of multipole components can correct for the window effect on the 3PCF with sufficiently good accuracy. Assuming that this result is not significantly different for the other BOSS samples, we calculate a total of 14 multipole components for

both  $Q_{\ell_1' \ell_2' \ell'}$  and  $\zeta_{\ell_1' \ell_2' \ell'}$  as follows:  $(\ell_1, \ell_2, \ell) = (0, 0, 0), (1, 1, 0), (2, 2, 0), (3, 3, 0)$  and  $(4, 4, 0)$  for the monopole 3PCF ( $\ell = 0$ ), and  $(\ell_1, \ell_2, \ell) = (0, 2, 2), (1, 1, 2), (2, 0, 2), (1, 3, 2), (2, 2, 2), (3, 1, 2), (2, 4, 2), (3, 3, 2)$  and  $(4, 2, 2)$  for the quadrupole 3PCF ( $\ell = 2$ ).

Figures 3 and 4 plot the 13 window 3PCF multipoles normalized by  $Q_{000}$  as a function of  $r_2$  after fixing  $r_1$  to 60 and  $120 h^{-1}$  Mpc. For the monopole components ( $Q_{110}, Q_{220}, Q_{330}$ , and  $Q_{440}$ ), we find that the window 3PCF multipoles measured at different redshift bins in each sky region (NGC or SGC) behave similarly (see, for example, the solid blue and dashed orange lines). On the other hand, for the quadrupole component, we see that the four BOSS samples may behave differently. The first few terms of the monopole and quadrupole components, such as  $Q_{110}, Q_{220}, Q_{202}, Q_{112}$ , and  $Q_{022}$ , have values of  $\mathcal{O}(0.01) - \mathcal{O}(0.1)$ , while the higher-order terms have values of  $\mathcal{O}(0.01)$  or less. Therefore, we can conclude that the higher-order window 3PCF multipoles have no significant effect on the final  $\zeta_{\ell_1' \ell_2' \ell'}^{(w)}(r_1, r_2)$ , as long as we measure the first few terms of the monopole and quadrupole components, i.e.,  $\zeta_{000}^{(w)}(r_1, r_2), \zeta_{110}^{(w)}(r_1, r_2), \zeta_{202}^{(w)}(r_1, r_2)$ , and  $\zeta_{112}^{(w)}(r_1, r_2)$ .

Figures 5 and 6 plot the theoretical predictions for the 3PCF multipoles, including window function effects, corresponding to the four BOSS samples. These calculations assume the  $\Lambda$ CDM and linear bias as in Figures 1 and 2, with redshifts of 0.38 and 0.61. As the value of  $r_1$  increases, the difference between NGC and SGC due to the window function effect becomes more considerable.

To quantitatively estimate the extent to which the multipole component of interest,  $\zeta_{\ell_1' \ell_2' \ell'}^{(w)}$ , is affected by the other multipole components,  $\zeta_{\ell_1' \ell_2' \ell'}$ , through window function effects, we compute the following quantities (Sugiyama et al. 2021):

$$\Delta \bar{\zeta}_{\ell_1' \ell_2' \ell'} = \frac{\text{Sum} \left[ \Delta \zeta_{\ell_1' \ell_2' \ell'} / Q_{000} \right]}{\text{Sum} \left[ \zeta_{\ell_1' \ell_2' \ell'}^{(w)} / Q_{000} \right]} \quad (4.30)$$

with

$$\begin{aligned} \Delta \zeta_{\ell_1' \ell_2' \ell'}^{\ell_1 \ell_2 \ell}(r_1, r_2) &= (4\pi) \sum_{\ell_1' + \ell_2' + \ell' = \text{even}} \begin{Bmatrix} \ell_1' & \ell_2' & \ell' \\ \ell_1 & \ell_2 & \ell \end{Bmatrix} \\ &\times \left[ \frac{h_{\ell_1 \ell_2 \ell} h_{\ell_1' \ell_2' \ell'} h_{\ell_2 \ell_2' \ell_2'} h_{\ell \ell \ell'}}{h_{\ell_1' \ell_2' \ell'} h_{\ell_1' \ell_2' \ell'}} \right] \\ &\times Q_{\ell_1' \ell_2' \ell'}(r_1, r_2) \zeta_{\ell_1' \ell_2' \ell'}(r_1, r_2) \end{aligned} \quad (4.31)$$

and

$$\text{Sum} [\zeta_{\ell_1 \ell_2 \ell}] = \begin{cases} \sum_{r_1 \geq r_2} \zeta_{\ell_1 \ell_2 \ell}(r_1, r_2) & \text{for } \ell_1 = \ell_2; \\ \sum_{r_1, r_2} \zeta_{\ell_1 \ell_2 \ell}(r_1, r_2) & \text{for } \ell_1 \neq \ell_2, \end{cases} \quad (4.32)$$

where  $\Delta \bar{\zeta}_{\ell_1' \ell_2' \ell'}$  satisfies  $\sum_{\ell_1' \ell_2' \ell'} \Delta \bar{\zeta}_{\ell_1' \ell_2' \ell'} = 1$ , and the summation is performed in the range of  $80 \leq r \leq 150 h^{-1}$  Mpc which we use for our data analysis.

Table 2 summarises the  $\Delta \bar{\zeta}_{\ell_1' \ell_2' \ell'}$  results calculated from Eq. (4.30) for the four BOSS samples. Naturally, the multipole component that is the same as the target one has the largest contribution. For example, for  $\zeta_{000}^{(w)}$  at  $z_{\text{eff}} = 0.38$  in NGC, 95.34% of the contribution comes from  $\zeta_{000}$ . For all four samples, multipole components other than the measured one have positive or negative values, and their overall contribution is about 5 – 10%. As expected, the contributions of higher-order components such as  $\zeta_{330}, \zeta_{440}$ , and  $\zeta_{332}$  are mostly below 0.5%. Therefore, we conclude that the window function correction equation in Eq. (4.29) can account for the window function effect on the 3PCF in BOSS with sufficient accuracy, even if it is

truncated at a finite number of 14 multipole components used in this work.

We note here the importance of  $\Delta \bar{\zeta}_{112}$ , which includes the  $M \neq 0$  modes of Scoccimarro et al. (1999)’ decomposition method in the correction for window function effects: it gives a contribution comparable to  $\Delta \bar{\zeta}_{202}$  and  $\Delta \bar{\zeta}_{022}$ , which include only the  $M = 0$  mode, and tends to have the opposite sign to that of  $\Delta \bar{\zeta}_{202}$  and  $\Delta \bar{\zeta}_{022}$ . Therefore, failure to properly account for effects such as  $\Delta \bar{\zeta}_{112}$  that include the  $M \neq 0$  modes may result in an error of  $\sim 5\%$  in the correction for the window function effect.

## 5 COVARIANCE MATRIX

We estimate the covariance matrix from the 2048 Patchy mock catalogues described in Section 4.1. Let  $\mathbf{d}^{(r)}$  be the data vector measured from the  $r$ -th catalogue, and  $\bar{\mathbf{d}} = (1/N_s) \sum_{r=1}^{N_s} \mathbf{d}^{(r)}$  be its mean value, then the covariance matrix of the data vector is given by

$$\mathbf{C} = \frac{1}{N_s - 1} \sum_{r=1}^{N_s} \left( \mathbf{d}^{(r)} - \bar{\mathbf{d}} \right) \left( \mathbf{d}^{(r)} - \bar{\mathbf{d}} \right)^T. \quad (5.1)$$

where  $N_s = 2048$  is the number of the Patchy mock catalogues.

### 5.1 Effects of a finite number of mocks

The covariance matrix  $\mathbf{C}$  inferred from the mock catalogues suffers from noise due to the finite number of mocks, which directly leads to an increase in the uncertainty of the cosmological parameters (Hartlap et al. 2007; Taylor et al. 2013; Dodelson & Schneider 2013; Percival et al. 2014; Taylor & Joachimi 2014). This effect is decomposed into two factors. First, the inverse covariance matrix,  $\mathbf{C}^{-1}$ , provides a biased estimate of the true inverse covariance matrix. To correct this bias, we rescale the inverse covariance matrix as (Hartlap et al. 2007)

$$\mathbf{C}_{\text{Hartlap}}^{-1} = \left( \frac{N_s - N_b - 2}{N_s - 1} \right) \mathbf{C}^{-1}, \quad (5.2)$$

where the pre-factor on the right-hand side,  $(N_s - N_b - 2)/(N_s - 1)$ , is the so-called ‘‘Hartlap’’ factor, and  $N_b$  is the number of data bins. Second, we need to consider the propagation of the error in the covariance matrix to the error on the estimated parameters. This effect is corrected by multiplying the final result of the parameter errors by the following factor (Percival et al. 2014)

$$M_1 = \sqrt{\frac{1 + B(N_b - N_p)}{1 + A + B(N_p + 1)}} \quad (5.3)$$

with

$$\begin{aligned} A &= \frac{2}{(N_s - N_b - 1)(N_s - N_b - 4)} \\ B &= \frac{N_s - N_b - 2}{(N_s - N_b - 1)(N_s - N_b - 4)}, \end{aligned} \quad (5.4)$$

where  $N_p$  is the number of parameters.

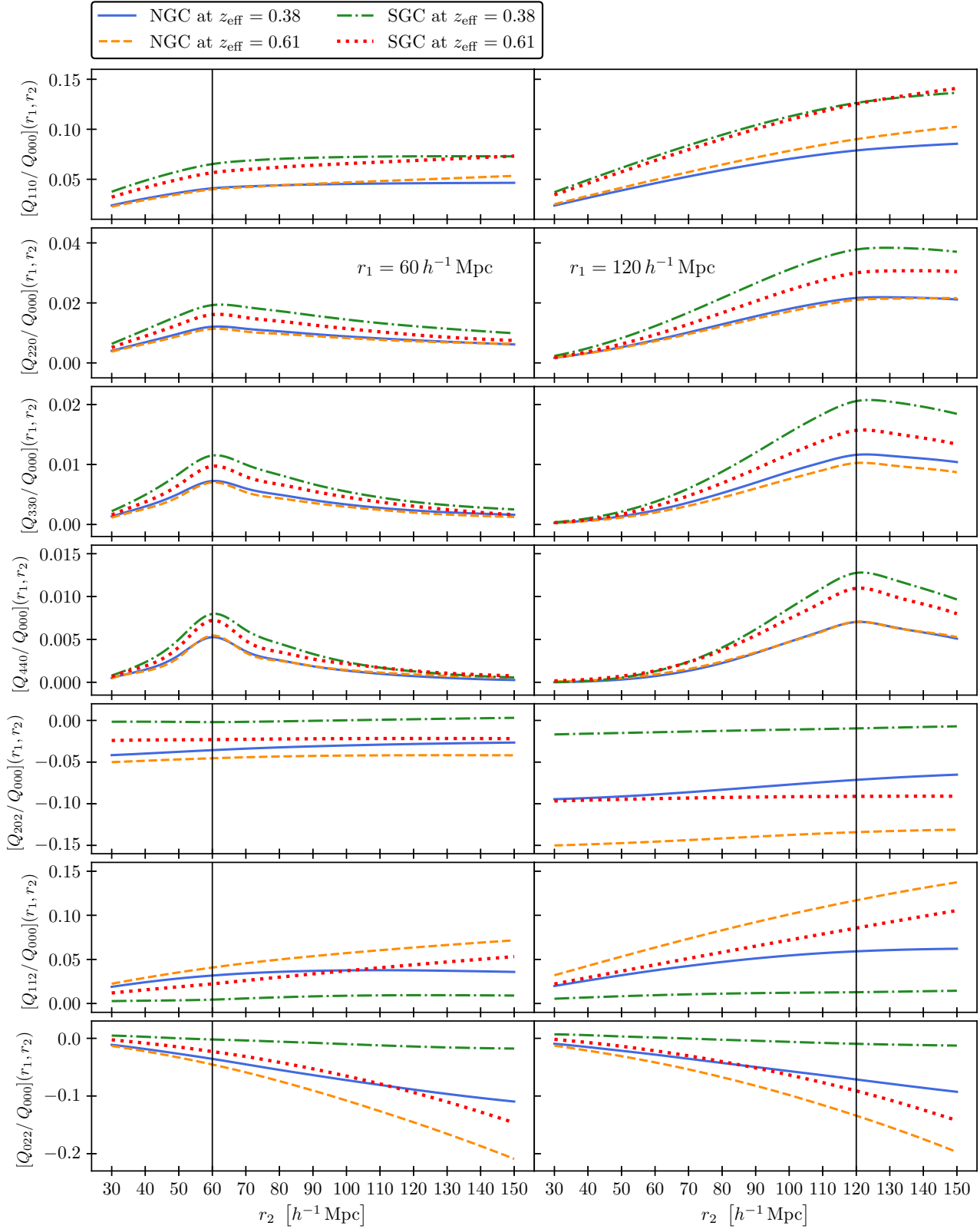
The derivation of the Hartlap factor (5.2) assumes that the data vector follows a Gaussian distribution. On the other hand, Sellentin & Heavens (2016) shows that in covariance matrix estimates from simulations, the data vector follows a multivariate  $t$ -distribution. When the number of simulations is sufficiently larger than the number of data bins, this  $t$ -distribution approaches a Gaussian distribution (Heavens et al. 2017), and the present analysis satisfies this condition. The reason is that the number of the Patchy mocks

$z_{\text{eff}} = 0.38 (0.2 < z < 0.5)$									
		NGC				SGC			
	$\Delta \bar{\zeta}_{\ell_1 \ell_2 \ell'}^{(w)}$ [%]	$\zeta_{000}^{(w)}$	$\zeta_{110}^{(w)}$	$\zeta_{202}^{(w)}$	$\zeta_{112}^{(w)}$	$\zeta_{000}^{(w)}$	$\zeta_{110}^{(w)}$	$\zeta_{202}^{(w)}$	$\zeta_{112}^{(w)}$
monopole ( $\ell = 0$ )	$\Delta \bar{\zeta}_{000}$	<b>95.34</b>	<b>1.59</b>	<b>-1.18</b>	<b>0.97</b>	<b>86.41</b>	<b>2.43</b>	-0.15	0.19
	$\Delta \bar{\zeta}_{110}$	<b>9.39</b>	<b>102.60</b>	<b>1.41</b>	<b>-3.77</b>	<b>13.66</b>	<b>98.60</b>	0.25	<b>-0.50</b>
	$\Delta \bar{\zeta}_{220}$	-0.09	<b>-0.53</b>	<b>1.14</b>	0.09	-0.12	<b>-0.79</b>	0.13	0.01
	$\Delta \bar{\zeta}_{330}$	0.26	0.21	0.08	-0.01	0.41	0.35	0.02	-0.02
	$\Delta \bar{\zeta}_{440}$	0.06	0.00	0.06	-0.00	0.09	0.01	-0.00	-0.00
quadrupole ( $\ell = 2$ )	$\Delta \bar{\zeta}_{202}$	<b>-3.75</b>	<b>0.59</b>	<b>90.14</b>	<b>2.07</b>	-0.43	0.10	<b>89.28</b>	<b>2.38</b>
	$\Delta \bar{\zeta}_{112}$	<b>4.36</b>	<b>-2.89</b>	<b>4.21</b>	<b>96.78</b>	<b>0.86</b>	-0.38	<b>5.06</b>	<b>92.64</b>
	$\Delta \bar{\zeta}_{022}$	<b>-4.57</b>	<b>0.81</b>	<b>0.50</b>	<b>2.75</b>	-0.48	0.14	<b>0.51</b>	<b>3.16</b>
	$\Delta \bar{\zeta}_{312}$	-0.10	-0.38	<b>1.95</b>	0.13	-0.05	-0.05	<b>2.87</b>	0.26
	$\Delta \bar{\zeta}_{222}$	0.04	0.04	0.38	0.07	-0.02	-0.01	-0.04	0.12
	$\Delta \bar{\zeta}_{132}$	<b>-0.56</b>	<b>-1.54</b>	0.14	0.23	-0.19	-0.19	0.18	<b>0.66</b>
	$\Delta \bar{\zeta}_{422}$	-0.21	-0.23	<b>1.02</b>	0.21	-0.02	-0.08	<b>1.53</b>	0.31
	$\Delta \bar{\zeta}_{332}$	0.10	0.08	0.02	0.10	-0.03	-0.02	0.10	0.24
$\Delta \bar{\zeta}_{242}$	-0.29	-0.34	0.12	0.38	-0.08	-0.14	0.26	<b>0.55</b>	

$z_{\text{eff}} = 0.61 (0.5 < z < 0.75)$									
		NGC				SGC			
	$\Delta \bar{\zeta}_{\ell_1 \ell_2 \ell'}^{(w)}$ [%]	$\zeta_{000}^{(w)}$	$\zeta_{110}^{(w)}$	$\zeta_{202}^{(w)}$	$\zeta_{112}^{(w)}$	$\zeta_{000}^{(w)}$	$\zeta_{110}^{(w)}$	$\zeta_{202}^{(w)}$	$\zeta_{112}^{(w)}$
monopole ( $\ell = 0$ )	$\Delta \bar{\zeta}_{000}$	<b>96.00</b>	<b>1.77</b>	<b>-2.00</b>	<b>1.78</b>	<b>89.49</b>	<b>2.40</b>	<b>-1.29</b>	<b>1.19</b>
	$\Delta \bar{\zeta}_{110}$	<b>10.43</b>	<b>104.18</b>	<b>2.92</b>	<b>-6.81</b>	<b>13.59</b>	<b>101.41</b>	<b>2.10</b>	<b>-4.36</b>
	$\Delta \bar{\zeta}_{220}$	-0.08	<b>-0.60</b>	<b>1.99</b>	0.01	-0.06	<b>-0.80</b>	<b>1.33</b>	-0.04
	$\Delta \bar{\zeta}_{330}$	0.25	0.21	0.04	0.01	0.35	0.31	0.00	-0.01
	$\Delta \bar{\zeta}_{440}$	0.06	0.01	0.05	-0.00	0.08	0.01	0.02	-0.00
quadrupole ( $\ell = 2$ )	$\Delta \bar{\zeta}_{202}$	<b>-6.26</b>	<b>1.21</b>	<b>86.94</b>	<b>2.72</b>	<b>-3.73</b>	<b>0.84</b>	<b>86.45</b>	<b>2.94</b>
	$\Delta \bar{\zeta}_{112}$	<b>7.84</b>	<b>-5.12</b>	<b>5.36</b>	<b>97.84</b>	<b>5.09</b>	<b>-3.31</b>	<b>5.98</b>	<b>94.88</b>
	$\Delta \bar{\zeta}_{022}$	<b>-7.65</b>	<b>1.65</b>	0.48	<b>3.64</b>	<b>-4.54</b>	<b>1.14</b>	0.44	<b>3.93</b>
	$\Delta \bar{\zeta}_{312}$	-0.01	<b>-0.54</b>	<b>2.25</b>	0.09	0.01	-0.30	<b>2.89</b>	0.17
	$\Delta \bar{\zeta}_{222}$	0.04	0.04	<b>0.69</b>	0.07	-0.00	0.01	0.42	0.11
	$\Delta \bar{\zeta}_{132}$	-0.28	<b>-2.63</b>	0.13	-0.02	-0.06	<b>-1.66</b>	0.15	0.25
	$\Delta \bar{\zeta}_{422}$	-0.18	-0.13	<b>0.98</b>	0.20	-0.07	-0.03	<b>1.21</b>	0.27
	$\Delta \bar{\zeta}_{332}$	0.08	0.09	0.03	0.10	-0.02	0.01	0.09	0.19
$\Delta \bar{\zeta}_{242}$	-0.24	-0.15	0.13	0.37	-0.12	-0.03	0.21	0.48	

**Table 2.** Contributions of other 3PCF multipole components to the observed 3PCF multipole components, as manifested through the effect of the window function, are shown for the four BOSS samples. When the contribution to the final result exceeds 0.5%, it is written in bold. The value of the same multipole component  $\Delta \bar{\zeta}_{\ell_1 \ell_2 \ell}$  (4.30) as the measured  $\zeta_{\ell_1 \ell_2 \ell}^{(w)}$  (4.29) is larger (smaller) than 100%, when the total contribution from all the other multipole components is negative (positive).



**Figure 3.** The monopole and quadrupole components of the window 3PCF (4.24),  $Q_{000}$ ,  $Q_{110}$ ,  $Q_{220}$ ,  $Q_{330}$ ,  $Q_{440}$ ,  $Q_{202}$ ,  $Q_{112}$ , and  $Q_{022}$ , measured from the four BOSS samples are shown as a function of  $r_2$  after fixing  $r_1$  to  $60 h^{-1} \text{ Mpc}$  (left) and  $120 h^{-1} \text{ Mpc}$  (right).



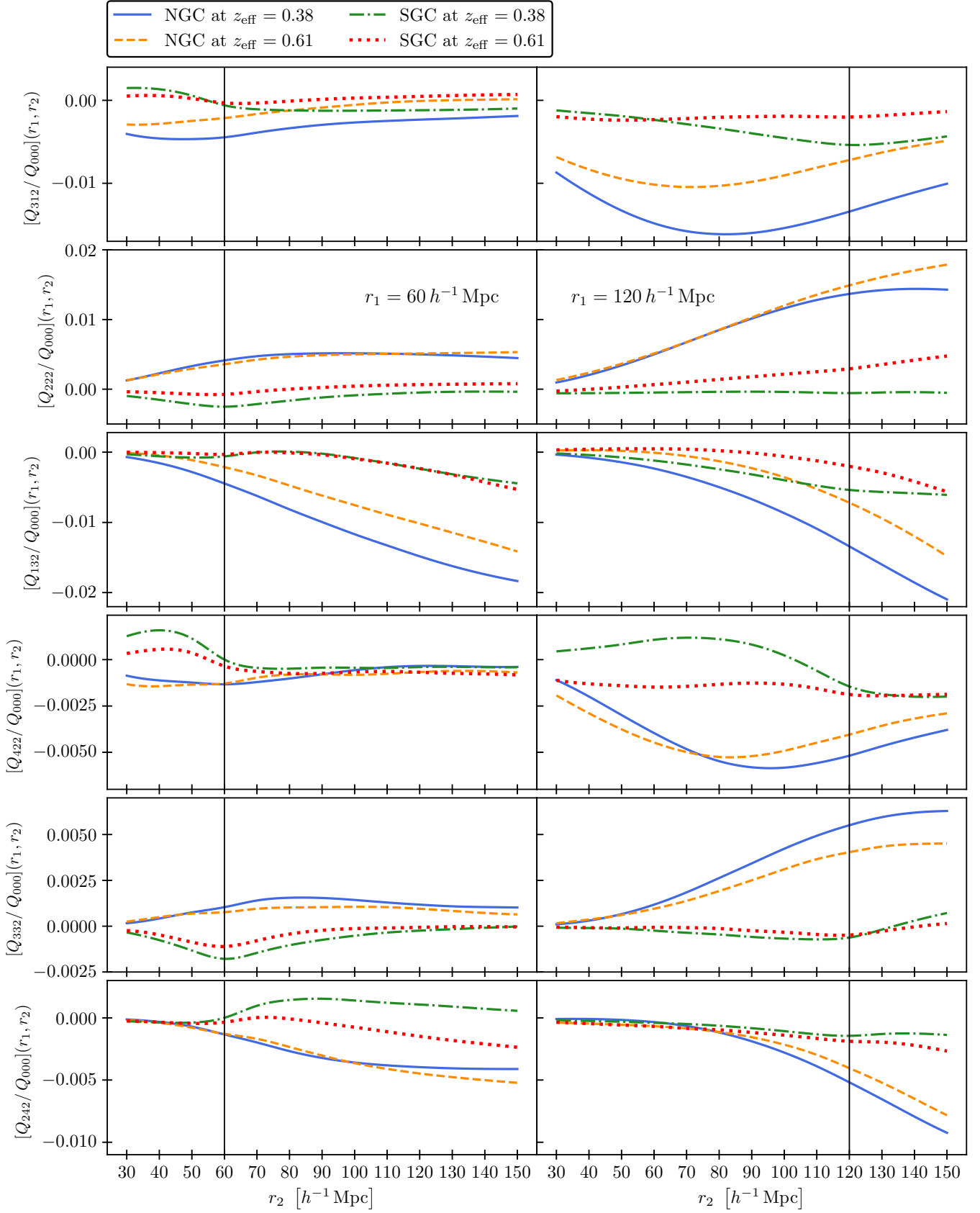


**Figure 4.** Same as Figure 3, except that the higher-order quadrupole components of the window 3PCF,  $Q_{312}$ ,  $Q_{222}$ ,  $Q_{132}$ ,  $Q_{422}$ ,  $Q_{332}$ , and  $Q_{242}$ , are shown.

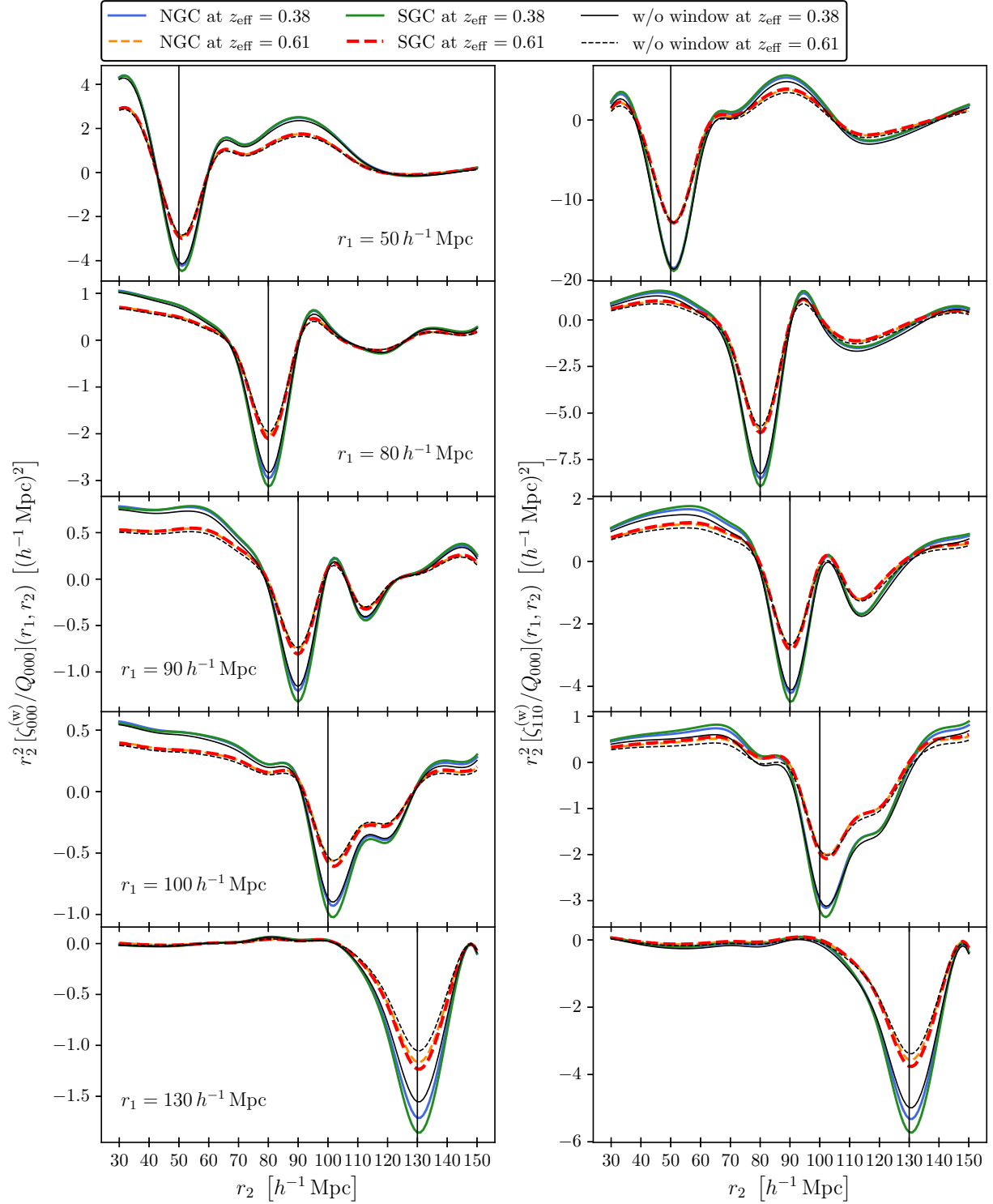


**Figure 5.** The monopole 3PCFs,  $\zeta_{000}$  (left) and  $\zeta_{110}$  (right), that include the window function effect (4.29) are shown for the four BOSS samples. The results are plotted as a function of  $r_2$  after fixing  $r_1$  to 50, 80, 90, 100, 130  $h^{-1}$  Mpc from top to bottom panels. For these calculations, the  $\Lambda$ CDM model at  $z = 0.61$ , the linear bias  $b_1 = 2.0$ , and no non-linear bias are assumed.

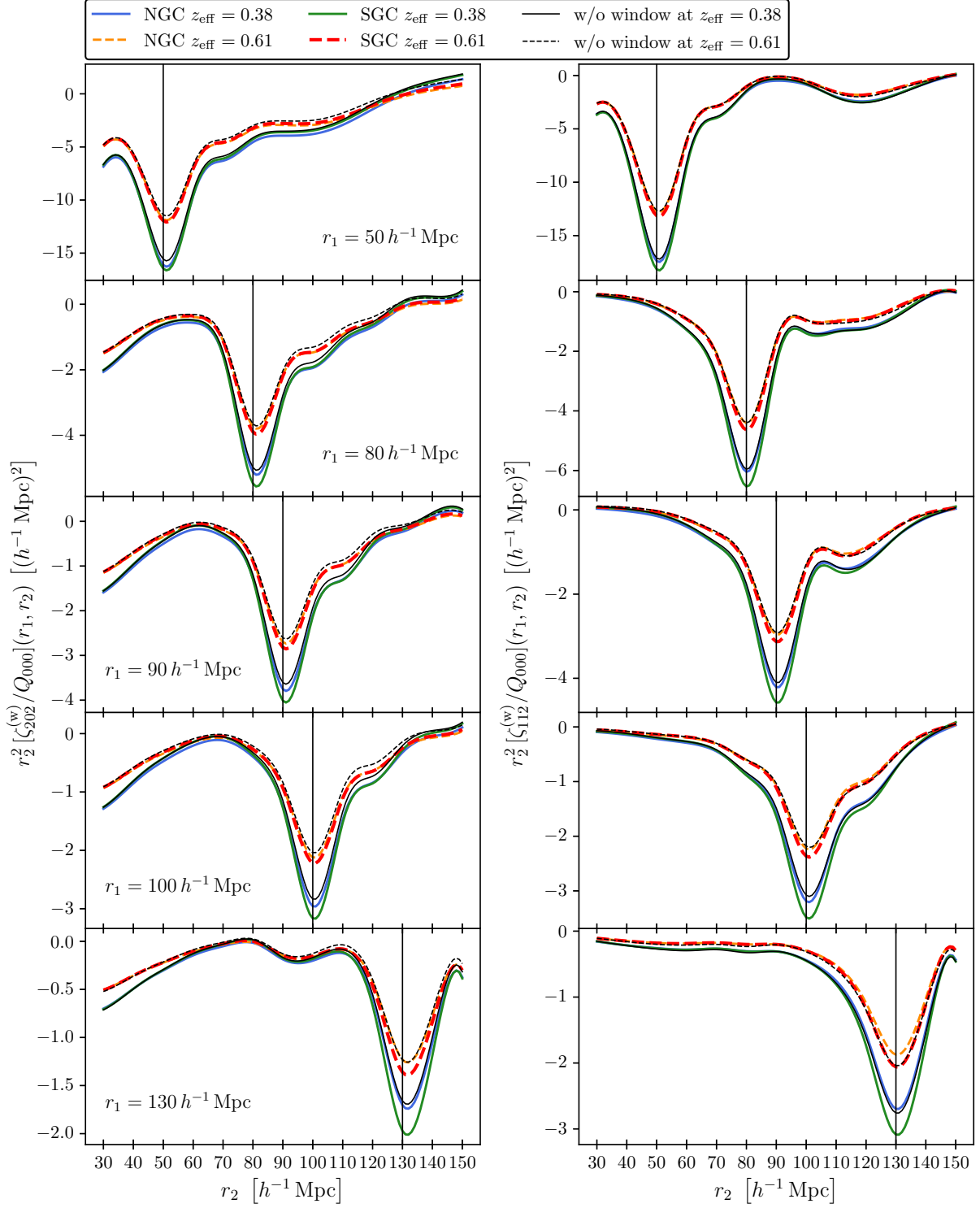


Figure 6. Same as Figure 5, except that the quadrupole 3PCFs,  $\zeta_{202}$  (left) and  $\zeta_{112}$  (right), are shown.

we use to estimate the covariance matrix is 2048, while the maximum number of data in our analysis is 202 (Section 6.2). In addition, the derivation of the  $M_1$  factor (5.3) also assumes the Gaussian distribution of the data vector, but there is no known value for the correction factor that corresponds to  $M_1$  in the Sellentin & Heavens (2016)'s method. Therefore, in this paper, we have decided to use Eqs. (5.2) and (5.3) to correct the uncertainty in parameter estimation due to a finite number of simulations (see also e.g., Percival et al. 2022).

We can therefore evaluate the effect of a finite number of mocks on the final error estimation using the square root of the Hartlap factor multiplied by the  $M_1$  factor (Percival et al. 2014),

$$M_2 = \sqrt{\frac{N_s - 1}{N_s - N_b - 2}} M_1. \quad (5.5)$$

Note that this  $M_2$  factor is not used in the actual analysis. It is essential to increase the number of simulations and reduce the number of data bins to keep the value of  $M_2$  as close to 1 as possible for a conservative analysis. The reason is that the Hartlap and  $M_1$  factors cannot be always accurately correct for parameter errors for any number of simulations. For example, using both monopole and quadrupole components of the 2PCF and 3PCF, as in this paper, Sugiyama et al. (2021) performed an anisotropic BAO analysis with the AP effect. The result showed that the error in the angular diameter distance for  $M_2 = 1.32$  is underestimated by about 10% compared to the case for  $M_2 = 1.06$  by changing the number of simulations. We will calculate the  $M_2$  factor in Section 6.4 and summarise the results in Table 3, where  $M_2 \sim 1.1$ , indicating that our analysis achieves  $M_2$  values sufficiently close to 1.

## 5.2 Correlation matrix

The  $(i, j)$  elements of the correlation matrix is computed from the covariance matrix as

$$r_{ij} = \frac{C_{ij}}{\sqrt{C_{ii}C_{jj}}}. \quad (5.6)$$

Considering the data vector  $\mathbf{d} = \{\xi_0, \xi_2, \zeta_{000}, \zeta_{110}, \zeta_{202}, \zeta_{112}\}$ , we show the results of the correlation matrix for the four BOSS samples in Figure 7. To simplify the figure, we only plot the results for the diagonal component of the 3PCF multipoles, i.e.,  $\zeta_{\ell_1\ell_2\ell}(r_1, r_2 = r_1)$ . The range of scales shown in the figure is  $80 \leq r \leq 150 h^{-1}$  Mpc, and the width of the  $r$ -bin is  $\Delta r = 10 h^{-1}$  Mpc. The four samples show similar results, and we summarise the overall features below. First, the monopole 2PCF and the monopole 3PCFs have a moderate correlation ( $0.25 < r_{ij} < 0.5$ ); the same is true for the quadrupole 2PCF and the quadrupole 3PCFs. Next, the first two terms of the monopole 3PCFs ( $\zeta_{000}$  and  $\zeta_{110}$ ) are strongly correlated with each other ( $0.5 < r_{ij} < 0.75$ ); on the other hand, the first two quadrupole 3PCFs ( $\zeta_{202}$  and  $\zeta_{112}$ ) are weakly correlated ( $0.0 < r_{ij} < 0.25$ ). This result indicates that  $\zeta_{202}$  and  $\zeta_{112}$  have independent information from each other. These results are consistent with the results in the bispectrum presented by Sugiyama et al. (2019).

## 5.3 Standard deviation

The standard deviation is given by the square root of the diagonal components of the covariance matrix: i.e.,  $\sqrt{C_{ii}}$ . Figure 8 shows the mean and standard deviation of  $\xi_\ell(r)$  and  $\zeta_{\ell_1\ell_2\ell}(r_1, r_2)$  calculated from the 2048 Patchy mock simulations. The mock data used are the NGC samples at  $z = 0.38$  and  $0.61$ . For  $\zeta_{\ell_1\ell_2\ell}(r_1, r_2)$ , the measured values and the standard deviations are plotted as a function of the scale variable  $r_1 = r_2 = r$  to simplify the figure.

From this figure, it can be seen that the mean values of  $\xi_\ell$  and  $\zeta_{\ell_1\ell_2\ell}$  do not differ much for the different redshifts, i.e.,  $z = 0.38$  and  $0.61$  (compare the magenta and blue lines). One may expect the amplitudes of  $\xi_\ell$  and  $\zeta_{\ell_1\ell_2\ell}$  to be larger at lower redshifts because the tree-level solutions (2.22) of  $\xi_\ell$  and  $\zeta_{\ell_1\ell_2\ell}$  are proportional to  $D^2$  and  $D^4$ , respectively, with  $D$  being the linear growth function. However, this is not the case in Figure 8. There are two possible reasons for this. The first is the bias effect. For halos with similar mass, the lower the redshift, the smaller the value of the linear bias  $b_1$  tends to be. Therefore,  $b_1 D(z)$  is less time-dependent and does not show significant differences at the different redshifts, especially for the monopole components of  $\xi_\ell$  and  $\zeta_{\ell_1\ell_2\ell}$ . A similar effect to the linear bias is likely to occur for the non-linear bias included in the 3PCF. Second, the product of the linear growth rate  $f$  and the linear growth function  $D$  is also a less time-dependent function. Therefore, the redshift dependence of  $\xi_\ell$  and  $\zeta_{\ell_1\ell_2\ell}$  is not pronounced, even for the quadrupole component.

On the other hand, the standard deviations of  $\xi_\ell$  and  $\zeta_{\ell_1\ell_2\ell}$  are significantly different for the different redshifts. In general, the so-called Gaussian terms in the covariance matrix depend only on the two-point statistic, while higher-order statistics such as the three-point statistic appear in the non-Gaussian terms. It is also known that the covariance matrix is inversely proportional to the survey volume, and that the higher the number density of observed galaxies, the smaller the covariance matrix. Therefore, the fact that the  $\xi_\ell$  and  $\zeta_{\ell_1\ell_2\ell}$  signals measured from the Patchy mock do not differ significantly at the different redshifts suggests that the redshift dependence in the standard deviation may be due to the survey volume and galaxy number density.

In Figure 8, the standard deviation at  $z = 0.61$  (blue) multiplied by  $\sqrt{V_{z=0.61}/V_{z=0.38}}$  is plotted as magenta dashed lines, with the survey volumes at  $z = 0.38$  and  $z = 0.61$  denoted as  $V_{z=0.38}$  and  $V_{z=0.61}$ , respectively. In the case of the 2PCF, the magenta dashed line is similar to the result at  $z = 0.38$  (magenta), indicating that the difference in the standard deviation of the 2PCF due to differences in redshift can be explained mainly by differences in the survey volume. However, this is not the case for the 3PCF, where the standard deviation of the 3PCF at  $z = 0.38$  is smaller than the magenta dashed line. This fact suggests that the effect of the galaxy number density on the covariance matrix is more significant for the 3PCF than for the 2PCF. In other words, as can be seen from Table 1, the sample at  $z = 0.38$  has a higher galaxy number density than the sample at  $z = 0.61$ , even though the survey volume is smaller. Therefore, the standard deviation at  $z = 0.38$  is smaller than the standard deviation at  $z = 0.61$  normalised to the survey volume at  $z = 0.38$ . This result is consistent with the finding of Sugiyama et al. (2020) that the galaxy number density plays an essential role in the covariance matrix of the bispectrum, even on large scales.

## 5.4 Cumulative signal-to-noise ratio

The covariance matrix is a two-dimensional quantity in the 2PCF case and a four-dimensional quantity in the 3PCF case. Therefore, a useful way compressing and quantifying this multi-dimensional information in the covariance matrix is to estimate the cumulative signal-to-noise (S/N) ratios, given by

$$\left(\frac{S}{N}\right) = \left(\bar{\mathbf{d}}^T \cdot \mathbf{C}_{\text{Hartlap}}^{-1} \cdot \bar{\mathbf{d}}\right)^{1/2}. \quad (5.7)$$

We calculate the cumulative S/N for each multipole component of the 2PCF and 3PCF: i.e.,  $\bar{\mathbf{d}} = \xi_0, \xi_2, \zeta_{000}, \zeta_{110}, \zeta_{202}$ , or  $\zeta_{112}$ . We



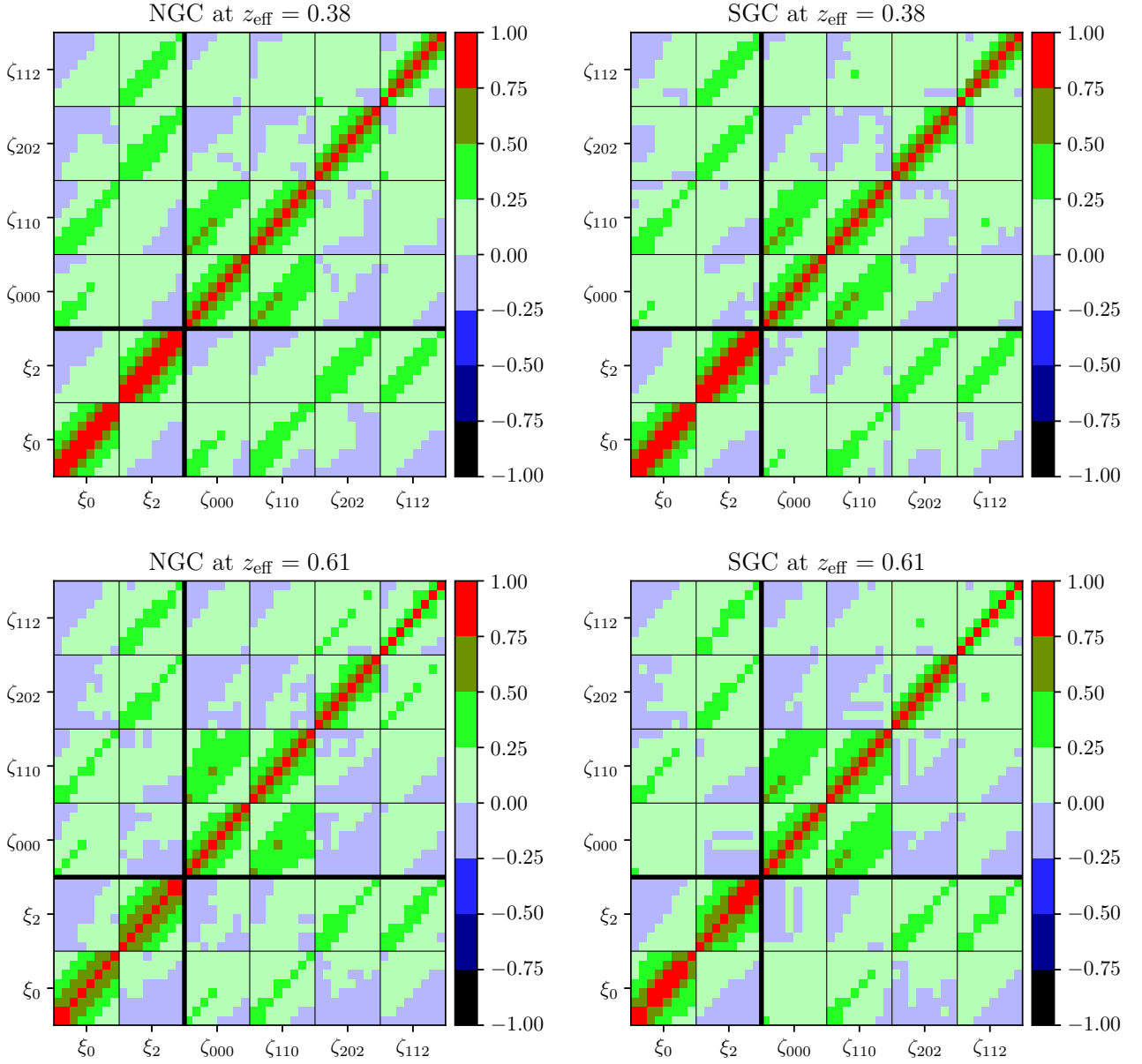


**Figure 7.** The correlation matrices of the monopole and quadrupole 2PCFs ( $\xi_0$  and  $\xi_2$ ), the first two monopole 3PCFs ( $\zeta_{000}$  and  $\zeta_{110}$ ), and the first two quadrupole 3PCFs ( $\zeta_{202}$  and  $\zeta_{112}$ ) are shown for the four BOSS samples. For simplicity of the figure, only the results for the  $r_1 = r_2$  case multipole 3PCFs, i.e.  $\zeta(r_1, r_2 = r_1)$ , are plotted, but in the actual analysis (Section 9), the data bins for the  $r_1 \neq r_2$  case are also used. The plotted scale range is  $80 \leq r \leq 150 h^{-1}$  Mpc, and the  $r$ -bin width is  $\Delta r = 10 h^{-1}$  Mpc.

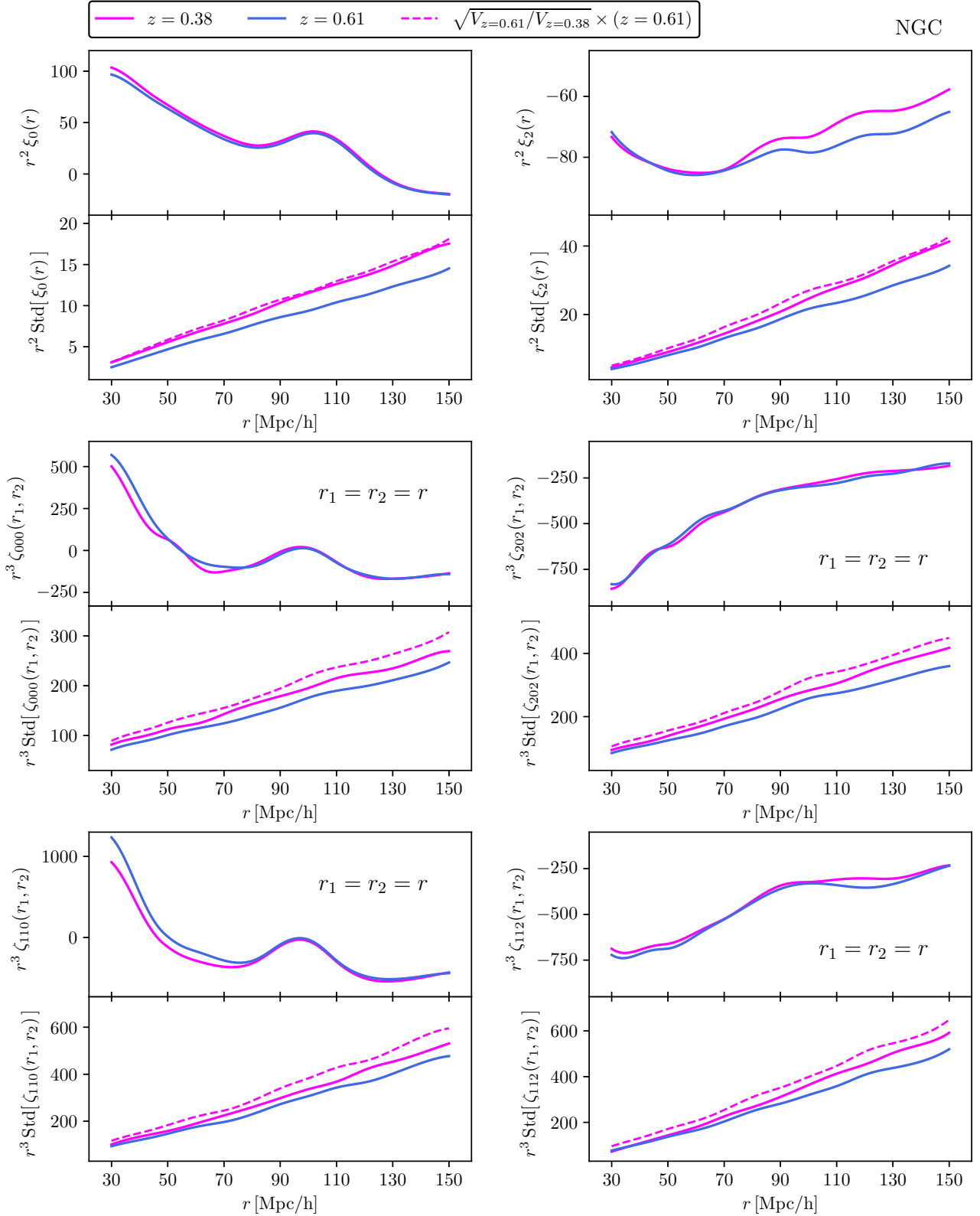


**Figure 8.** The mean values and standard deviations of  $\xi_0$ ,  $\xi_2$ ,  $\xi_{000}$ ,  $\xi_{110}$ ,  $\xi_{202}$ , and  $\xi_{112}$  calculated from the 2048 Patchy mock catalogues. The results are plotted at the two redshifts,  $z = 0.38$  (magenta) and  $0.61$  (blue), for the NGC sample. The magenta dashed lines are the standard deviation at  $z = 0.61$  multiplied by  $\sqrt{V_{z=0.61}/V_{z=0.38}}$  and normalized to have the same survey volume as the sample at  $z = 0.38$ , where the survey volumes at  $z = 0.38$  and  $z = 0.61$ ,  $V_{z=0.38}$  and  $V_{z=0.61}$ , respectively, are given in Table 1. For simplicity of the figure, only the results in the  $r_1 = r_2$  case for the 3PCF are plotted.

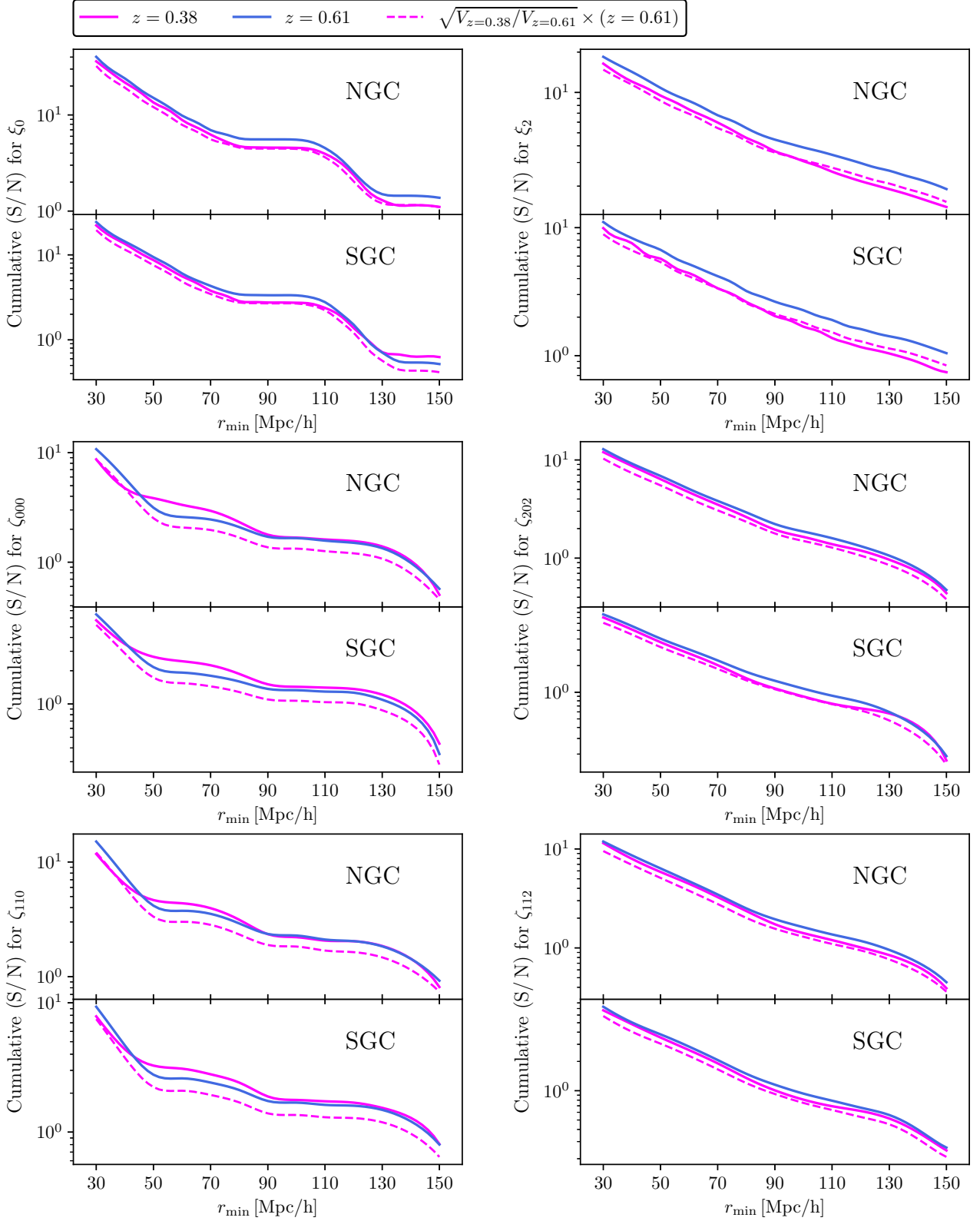


**Figure 9.** Cumulative signal-to-noise ratios ( $S/Ns$ ) for the multipole components of the 2PCF and 3PCF, where both signal and noise (covariance matrix) are computed from the 2048 Patchy mock catalogues. The maximum scale used for the  $S/N$  calculation is fixed at  $r_{\max} = 150 h^{-1} \text{Mpc}$  and the  $S/Ns$  are plotted as a function of the minimum scale  $r_{\min}$ . The blue and magenta solid lines show the results for the samples at  $z = 0.61$  and  $z = 0.38$ , respectively. The magenta dashed lines are the  $S/N$  values in the sample at  $z = 0.61$  multiplied by  $\sqrt{V_{z=0.38}/V_{z=0.61}}$ .

also fix the maximum scale  $r_{\max} = 150 h^{-1}$  Mpc, vary the minimum scale  $r_{\min}$  from  $150 h^{-1}$  Mpc to  $30 h^{-1}$  Mpc, and calculate the S/N as a function of  $r_{\min}$ . In Figure 9, we plot the S/N for the four BOSS samples, NGC and SGC at  $z = 0.38$  and  $0.61$ . Note that we do not consider cross-covariance matrices between different multipole components, e.g., between  $\xi_0$  and  $\zeta_{000}$ . How the information in the covariance matrix, including all cross-covariance matrices, ultimately propagates to the errors in the cosmological parameters of interest will be discussed through the Fisher analysis in Section 7.

The top two panels of Figure 9 show the S/N of  $\xi_0$  and  $\xi_2$ . In all cases shown in the panels, the S/N at  $z = 0.61$  (blue line) is larger than the S/N at  $z = 0.38$  (magenta line). The difference is because the S/N of the 2PCF is proportional to the square root of the survey volume  $V$ , and the survey volume at  $z = 0.61$ , denoted  $V_{z=0.61}$ , is larger than the survey volume at  $z = 0.38$ ,  $V_{z=0.38}$ . Therefore, multiplying the S/N at  $z = 0.61$  by  $\sqrt{V_{z=0.38}/V_{z=0.61}}$  approximately reproduces the S/N at  $z = 0.38$  (see magenta dashed lines). This result is consistent with the findings in the signal and standard deviation of the 2PCF in Figure 8.

The middle and bottom results are for  $\zeta_{000}$ ,  $\zeta_{110}$ ,  $\zeta_{202}$ , and  $\zeta_{112}$ . These results show that, in contrast to the 2PCF case, the S/N at  $z = 0.38$  is comparable to the S/N at  $z = 0.61$ . The difference in the S/N at  $z = 0.38$  and  $z = 0.61$  in the 3PCF case cannot be explained by the difference in the survey volumes (see magenta dashed lines). This behaviour of the S/N of the 3PCF can be explained by the finding shown in Figure 8 that the galaxy number density strongly influences the standard deviation of the 3PCF. In particular, in the present case, the effect of the galaxy number density is more pronounced when considering correlations between different scales, resulting in the S/N at  $z = 0.38$  that is comparable to the S/N at  $z = 0.61$ . This result shows that a higher galaxy number density is as important for obtaining cosmological information from the 3PCF as increasing the survey volume.

## 6 ANALYSIS SETTINGS

### 6.1 Likelihoods

We assume that the likelihood of the data compared to the model predictions follows a multivariate Gaussian distribution:

$$\ln \mathcal{L}(\mathbf{d}|\boldsymbol{\theta}) = -\frac{1}{2} [\mathbf{d} - \mathbf{t}(\boldsymbol{\theta})] \mathbf{C}_{\text{Hartlap}}^{-1} [\mathbf{d} - \mathbf{t}(\boldsymbol{\theta})]^T, \quad (6.1)$$

where  $\mathbf{d}$  is the data vector,  $\mathbf{t}$  is the model prediction of the data vector given the model parameters  $\boldsymbol{\theta}$ , and  $\mathbf{C}_{\text{Hartlap}}^{-1}$  is the inverse of the covariance matrix after correction by the Hartlap factor (5.2). We can then obtain the posterior distribution of the model parameters given the data by performing Bayesian inference:

$$\mathcal{P}(\boldsymbol{\theta}|\mathbf{d}) \propto \mathcal{L}(\mathbf{d}|\boldsymbol{\theta})\Pi(\boldsymbol{\theta}) \quad (6.2)$$

where  $\mathcal{P}(\boldsymbol{\theta}|\mathbf{d})$  is the posterior distribution of  $\boldsymbol{\theta}$  given the data vector,  $\mathbf{d}$ , and  $\Pi(\boldsymbol{\theta})$  is the prior distribution.

We assume that the four BOSS galaxy samples (Table 1) are far enough apart that they each have independent cosmological information. Then, when constraining the model parameters common to each galaxy sample, we add up the likelihood functions of each galaxy sample. For example, when using all four galaxy samples, the total likelihood function is given by

$$\begin{aligned} \ln \mathcal{L}_{\text{total}} = & \ln \mathcal{L}_{\text{NGC at } z=0.38} + \ln \mathcal{L}_{\text{SGC at } z=0.38} \\ & + \ln \mathcal{L}_{\text{NGC at } z=0.61} + \ln \mathcal{L}_{\text{SGC at } z=0.61}. \end{aligned} \quad (6.3)$$

### 6.2 Multipoles used, scale range, and number of bins

To repeat what was explained in Section 4.2, the scale range used for parameter estimation in Section 9 is  $80 h^{-1} \text{ Mpc} \leq r \leq 150 h^{-1} \text{ Mpc}$ , and we choose  $\Delta r = 5 h^{-1} \text{ Mpc}$  and  $10 h^{-1} \text{ Mpc}$  for the 2PCF and 3PCF bin widths, respectively. The 2PCF and 3PCF multipoles used are the monopole and quadrupole 2PCFs ( $\xi_0$  and  $\xi_2$ ), the two monopole 3PCFs ( $\zeta_{000}$  and  $\zeta_{202}$ ), and the two quadrupole 3PCFs ( $\zeta_{202}$  and  $\zeta_{112}$ ). Considering  $\zeta_{\ell_1 \ell_2 \ell}(r_1, r_2) = \zeta_{\ell_2 \ell_1 \ell}(r_2, r_1)$ , the numbers of data bins for the 2PCF and 3PCF multipoles are 15, 15, 36, 36, 64, and 36 for  $\xi_0$ ,  $\xi_2$ ,  $\zeta_{000}$ ,  $\zeta_{110}$ ,  $\zeta_{202}$ , and  $\zeta_{112}$ , respectively. The reason why the bin width for the 3PCF is wider than for the 2PCF is to reduce the number of data bins and to conservatively estimate the inverse covariance matrix for the 2PCF and 3PCF. The total number of data bins is then 202, which is small enough compared to the 2048 Patchy mock simulations (Section 5).

### 6.3 Parameter setting

The parameters we constrain are as follows:

$$\boldsymbol{\theta} = \boldsymbol{\theta}_{\text{phys}} + \boldsymbol{\theta}_{\text{bias}}, \quad (6.4)$$

where

$$\boldsymbol{\theta}_{\text{bias}} = \{(b_1 \sigma_8), (F_g \sigma_8), (F_t \sigma_8)\}, \quad (6.5)$$

and

$$\boldsymbol{\theta}_{\text{phys}} = \begin{cases} \{f \sigma_8, \sigma_8\}, & \text{GR;} \\ \{\sigma_8, \xi_f, \xi_t\}, & \text{Horndeski;} \\ \{F_s \sigma_8, \xi_f, \xi_s, \xi_t\}, & \text{DHOST.} \end{cases} \quad (6.6)$$

The parameters  $F_{g,s,t}$  and  $\xi_{f,s,t}$  are given in Eq. (3.15) and (3.27), respectively; the reason  $F_s$  does not appear in GR and Horndeski theories is that  $F_s = 1$  in those theories. We assume that the bias parameters  $\boldsymbol{\theta}_{\text{bias}}$  take different values in all four BOSS samples.  $f \sigma_8$ ,  $\sigma_8$ , and  $F_s \sigma_8$  have common values in NGC and SGC.  $\xi_{f,s,t}$  are common to all four BOSS samples. For the 2PCF analysis, we only consider  $b_1 \sigma_8$  and  $f \sigma_8$ . For example, if all four BOSS samples are used to constrain DHOST theories, the total number of parameters is 17. Once again, note that the AP parameters are not varied in this analysis.

### 6.4 $M_1$ and $M_2$ factors

As mentioned in Section 5, the number of the Patchy mock simulations used to calculate the covariance matrices for the 2PCF and 3PCF is finite, so the inverse of the covariance matrix must be multiplied by the Hartlap factor and the final parameter error by  $M_1$ .

The  $M_1$  factor (5.3) is derived assuming that all parameters are constrained from a single data set. However, when constraining the common parameters  $\xi_f$ ,  $\xi_s$ , and  $\xi_t$  (3.27) from the four independent BOSS samples, as in the present analysis, the  $M_1$  factor is expected to take a different form, but we do not know the correct correction factor corresponding to the  $M_1$  factor in such as case. Therefore, when we use different galaxy samples simultaneously, we first count up all common and non-common parameters in the galaxy samples. Then, we calculate the  $M_1$  factor using the number of data bins computed from a single galaxy sample and the number of the Patchy mocks, 2048, corresponding to that galaxy sample, and multiply it by the final parameter error. Specifically, the multipole components of the 2PCF and 3PCF measured from a single galaxy sample are  $\xi_0$ ,  $\xi_2$ ,  $\zeta_{000}$ ,  $\zeta_{110}$ ,  $\zeta_{202}$ , and  $\zeta_{112}$ , for a total data bin number of



	$M_1$	$M_2$	# of params.
2PCF only ( $z_{\text{eff}} = 0.38$ )	1.006	1.013	3
2PCF only ( $z_{\text{eff}} = 0.61$ )	1.006	1.013	3
GR ( $z_{\text{eff}} = 0.38$ )	1.049	1.105	8
GR ( $z_{\text{eff}} = 0.61$ )	1.049	1.105	8
Horndeski ( $z_{\text{eff}} = 0.38$ )	1.048	1.104	9
Horndeski ( $z_{\text{eff}} = 0.61$ )	1.048	1.104	9
Horndeski ( $z_{\text{eff}} = 0.38, 0.61$ )	1.044	1.100	16
DHOST ( $z_{\text{eff}} = 0.38$ )	1.048	1.104	10
DHOST ( $z_{\text{eff}} = 0.61$ )	1.048	1.104	10
DHOST ( $z_{\text{eff}} = 0.38, 0.61$ )	1.044	1.100	17

**Table 3.** A summary of the  $M_1$  (5.3) and  $M_2$  (5.5) factor values used in our analysis. These values are calculated from the number of the Patchy mock simulations, 2048 (Section 4.1), the number of data bins, 30 for the 2PCF only and 202 for the 2+3PCF (Section 6.2), and the number of parameters summarised in the rightmost column (Section 6.3).

202 (Section 6.2). The number of parameters depends on the type of analysis; for example, we need 17 parameters to test DHOST theories using all four galaxy samples (Section 6.3).

Table 3 summarises the values of the  $M_1$  and  $M_2$  factors calculated in our analysis, leading to  $M_2 \sim 1.1$  for all the 2+3PCF joint analyses. Thus, even without considering the Hartlap and  $M_1$  factors in our analysis, the effect of finite mocks is at most 10%. In other words, since our analysis correctly considers these factors, the error due to the finite mock effect in the estimated parameter error is guaranteed to be  $\lesssim 10\%$ .

## 6.5 MCMC

We apply the Metropolis-Hastings (MH) algorithm, an Markov Chain Monte Carlo (MCMC) method, implemented in the publicly available software package MONTE PYTHON (Audren et al. 2013; Brinckmann & Lesgourgues 2019) to estimate the posterior distribution of parameters in a multi-dimensional parameter space. In doing so, we set the super-update parameter to 20, as recommended by the developers. In order to improve the convergence of the posterior distributions obtained by MCMC, we first perform an MCMC analysis with the number of steps set to  $N_{\text{step}} = 200\,000$  and calculate the best-fit values and covariance matrix of the parameters. Then, we add the information of the best-fit values and covariance matrix and perform an MCMC analysis again with the same number of steps.

We ensure convergence of each MCMC chain, imposing  $R - 1 \lesssim \mathcal{O}(10^{-4})$  where  $R$  is the standard Gelman-Rubin criteria (Gelman & Rubin 1992). Furthermore, the convergence of the results is also checked through the following method. First, we create eight independent MCMC chains and compute the mean and standard deviation of the parameters from each chain. Then, from the eight means and standard deviations, we compute the standard deviation of the mean and the mean of the standard deviation and check that the ratio of them is less than about 20% for all the results.

## 6.6 Mock tests

We perform MCMC analyses on 100 Patchy mock catalogues (Kitaura et al. 2016) using the same set of cosmological and nuisance parameters as in the actual BOSS galaxy data analysis. We then verify that our analysis can correctly return the values of the

non-linear parameters predicted by GR for the Patchy mock catalogues designed under the assumption of a  $\Lambda$ CDM model. We also discuss the statistical scatter of the 100 values of the parameters to be estimated.

## 7 FISHER ANALYSIS

Before proceeding to the MCMC analysis using actual galaxies in Sections 8 and 9, in this section, we will understand how the 3PCF contains cosmological information through the Fisher analysis.

There are several reasons for performing the Fisher analysis before the MCMC analysis. First, calculating the Fisher matrix in Section 7.1 is less computationally intensive than performing the MCMC analysis, making it easier to compare the analysis results in various settings that take too much time in the MCMC analysis. Taking advantage of this, Section 7.2 examines how the constraints on the parameters of interest change for various combinations of the multipole components of the 3PCF; in doing so, we focus only on the NGC sample at  $z = 0.38$  as a representative example. Section 7.3 also discusses the relation among the values of the predicted parameter errors for the four BOSS samples, NGC and SGC at  $z = 0.38, 0.61$ , and how the combination of the four BOSS samples affects the final results. Finally, in Section 9.11, we compare the results obtained from the above Fisher analysis with those obtained from the MCMC parameter estimation and check their consistency to confirm the validity of the final results in this paper.

In Section 7.4, the Fisher analysis also allows us to estimate cosmological information at scales smaller than the scale range used in the MCMC analysis. The results are expected to motivate the construction of theoretical models applicable to smaller scales.

Finally, in Section 7.5, we use the results of the Fisher analysis to determine the range of a flat prior used when performing the MCMC analysis.

### 7.1 Fisher matrix

From the likelihood function given in Eq. (6.1), we calculate the Fisher matrix as

$$F_{ij} = - \left\langle \frac{\partial}{\partial \theta_i} \frac{\partial}{\partial \theta_j} \ln \mathcal{L} \right\rangle = \frac{\partial \mathbf{t}(\boldsymbol{\theta})}{\partial \theta_i} \mathbf{C}_{\text{Hartlap}}^{-1} \frac{\partial \mathbf{t}^T(\boldsymbol{\theta})}{\partial \theta_j}, \quad (7.1)$$

where we assumed that the covariance matrix  $\mathbf{C}$  is independent of the parameters. The indices  $i$  and  $j$  run over parameters of interest. In the limit of the Gaussian likelihood surface, the Cramer-Rao inequality shows that the Fisher matrix provides the minimum standard deviation on parameters, marginalized over all the other parameters:  $\sigma(\theta_i) \geq \sigma_{\text{fisher}}(\theta_i) = (F^{-1})_{ii}^{1/2}$ . We note that we adopt the inverse covariance matrix,  $\mathbf{C}_{\text{Hartlap}}^{-1}$ , that is non-Gaussian estimated from the Patchy mock simulations.

We consider three parameter vectors, depending on the gravity theory of interest:

$$\boldsymbol{\theta} = \{(b_1\sigma_8), (f\sigma_8)\} + \boldsymbol{\theta}_{3\text{PCF}}, \quad (7.2)$$

with

$$\boldsymbol{\theta}_{3\text{PCF}} = \begin{cases} \{(F_g\sigma_8), (F_s\sigma_8), (F_t\sigma_8)\}, & \text{GR;} \\ \{(F_g\sigma_8), (F_s\sigma_8), (F_t\sigma_8), (G_t\sigma_8)\}, & \text{Horndeski;} \\ \{(F_g\sigma_8), (F_s\sigma_8), (F_t\sigma_8), (G_s\sigma_8), (G_t\sigma_8)\}, & \text{DHOST,} \end{cases} \quad (7.3)$$

	$(b_1\sigma_8)_{\text{fid}}$	$(f\sigma_8)_{\text{fid}}$	$(F_g\sigma_8)_{\text{fid}}$	$(F_s\sigma_8)_{\text{fid}}$	$(F_t\sigma_8)_{\text{fid}}$	$(G_s\sigma_8)_{\text{fid}}$	$(G_t\sigma_8)_{\text{fid}}$
	1.362	0.485	0.552	0.681	0.194	0.681	0.386
	$\sigma_{\text{fisher}}(b_1\sigma_8)$	$\sigma_{\text{fisher}}(f\sigma_8)$	$\sigma_{\text{fisher}}(F_g\sigma_8)$	$\sigma_{\text{fisher}}(F_s\sigma_8)$	$\sigma_{\text{fisher}}(F_t\sigma_8)$	$\sigma_{\text{fisher}}(G_s\sigma_8)$	$\sigma_{\text{fisher}}(G_t\sigma_8)$
GR							
Case 1	0.159	0.093	–	–	–	–	–
Case 2	0.154	0.093	0.418	0.472	0.312	–	–
Case 3	0.159	0.092	0.802	1.170	2.387	–	–
Case 4	0.155	0.091	0.420	0.643	0.426	–	–
Case 5	0.151	0.090	0.330	0.450	0.291	–	–
Case 6	0.155	0.089	0.396	0.619	0.411	–	–
Case 7	0.151	0.089	0.315	0.442	0.283	–	–
Case 8	0.153	0.091	0.363	0.492	0.324	–	–
Horndeski							
Case 2	0.154	0.093	2.361	0.479	3.156	–	29.25
Case 3	0.159	0.092	0.816	2.433	2.633	–	1.312
Case 4	0.155	0.092	0.430	0.726	0.431	–	1.111
Case 5	0.151	0.091	0.331	0.463	0.295	–	1.044
Case 6	0.155	0.091	0.409	0.715	0.419	–	1.015
Case 7	0.151	0.091	0.316	0.459	0.285	–	0.946
Case 8	0.153	0.091	0.366	0.498	0.344	–	1.383
DHOST							
Case 2	0.154	0.093	3.100	3.840	4.774	35.22	38.88
Case 3	0.159	0.093	2.211	3.652	2.633	2.976	1.981
Case 4	0.157	0.092	0.726	0.748	0.446	1.896	1.112
Case 5	0.153	0.092	0.499	0.476	0.303	1.636	1.051
Case 6	0.156	0.091	0.710	0.739	0.431	1.757	1.017
Case 7	0.153	0.091	0.487	0.468	0.293	1.519	0.953
Case 8	0.154	0.092	0.595	0.528	0.344	2.292	1.580

**Table 4.** The standard deviations of the parameters as predicted by the Fisher analysis, denoted as  $\sigma_{\text{fisher}}(\theta)$ , are shown. These results are for the NGC at  $z_{\text{eff}} = 0.38$ . The parameter vectors of interest,  $\theta$ , are different for each of the three gravity theories, GR, Horndeski, and DHOST theories (Eq. 7.3). The classification of the data vectors used is as shown in Eq. (7.4). The fiducial values of the parameters are calculated under the assumption of GR and are denoted as  $(\theta)_{\text{fid}}$ . The scale range used for this Fisher analysis is  $80 h^{-1} \text{ Mpc} \leq r \leq 150 h^{-1} \text{ Mpc}$ .

	$(E_f)_{\text{fid}}$	$(E_s)_{\text{fid}}$	$(E_t)_{\text{fid}}$	$(\xi_f)_{\text{fid}}$	$(\xi_s)_{\text{fid}}$	$(\xi_t)_{\text{fid}}$
	0.713	1.000	0.992	0.545	0.000	0.013
	$\sigma_{\text{fisher}}(E_f)$	$\sigma_{\text{fisher}}(E_s)$	$\sigma_{\text{fisher}}(E_t)$	$\sigma_{\text{fisher}}(\xi_f)$	$\sigma_{\text{fisher}}(\xi_s)$	$\sigma_{\text{fisher}}(\xi_t)$
Horndeski						
Case 2	0.502	–	75.28	1.146	–	124.3
Case 3	2.558	–	6.018	5.844	–	9.934
Case 4	0.760	–	3.189	1.737	–	5.264
Case 5	0.488	–	2.767	1.114	–	4.567
Case 6	0.750	–	2.969	1.714	–	4.901
Case 7	0.483	–	2.522	1.103	–	4.163
Case 8	0.523	–	3.597	1.194	–	5.938
DHOST						
Case 2	4.018	57.31	103.8	9.180	93.85	171.3
Case 3	3.824	6.519	9.837	8.737	10.68	16.24
Case 4	0.785	2.835	3.213	1.794	4.642	5.304
Case 5	0.503	2.460	2.771	1.150	4.029	4.574
Case 6	0.777	2.633	2.998	1.776	4.311	4.950
Case 7	0.495	2.260	2.527	1.130	3.701	4.172
Case 8	0.558	3.542	3.981	1.274	5.801	6.572

**Table 5.** Same as Table 4, but the standard deviations of the parameters defined in Eqs. (3.23) and (3.27), calculated through variable transformations, are shown.

where  $F_s\sigma_8 = \sigma_8$  for GR and Horndeski theories. We obtain the results for  $E_{f,s,t}$  and  $\xi_{f,s,t}$  using the variable transformations in Eqs. (3.23) and (3.27). In particular, the results including  $\xi_{f,s,t}$  correspond to the parameter set (6.6) used in the MCMC analysis performed in Section 9.

The fiducial values of the cosmological parameters needed to compute the Fisher matrix are the values in the  $\Lambda$ CDM model presented in Section 1. In doing so, we assume that the linear bias is  $b_1 = 2$ , and the values of the non-linear biases are zero: i.e.,  $b_2 = b_{s2} = 0$ .

## 7.2 Information contained in 3PCF multipoles

For the NGC sample at  $z = 0.38$ , we perform Fisher analyses on the following eight data vectors consisting of combinations of the 2PCF and 3PCF multipole components, using the same settings as the MCMC analysis performed in Section 9 to investigate which components and how they affect parameter estimates.

$$\begin{aligned}
 \text{Case 1 } \mathbf{d} &= \{\xi_0, \xi_2\}; \\
 \text{Case 2 } \mathbf{d} &= \{\xi_0, \xi_2, \zeta_{000}, \zeta_{110}\}; \\
 \text{Case 3 } \mathbf{d} &= \{\xi_0, \xi_2, \zeta_{202}, \zeta_{112}\}; \\
 \text{Case 4 } \mathbf{d} &= \{\xi_0, \xi_2, \zeta_{000}, \zeta_{202}\}; \\
 \text{Case 5 } \mathbf{d} &= \{\xi_0, \xi_2, \zeta_{000}, \zeta_{202}, \zeta_{110}\}; \\
 \text{Case 6 } \mathbf{d} &= \{\xi_0, \xi_2, \zeta_{000}, \zeta_{202}, \zeta_{112}\}; \\
 \text{Case 7 } \mathbf{d} &= \{\xi_0, \xi_2, \zeta_{000}, \zeta_{202}, \zeta_{110}, \zeta_{112}\}; \\
 \text{Case 8 } \mathbf{d} &= \{\xi_0, \xi_2, \zeta_{110}, \zeta_{112}\}. \tag{7.4}
 \end{aligned}$$

Case 1 constrains  $f\sigma_8$  using only the monopole and quadrupole 2PCFs. Cases 2, 3, and 4 add to Case 1 the two monopole 3PCFs ( $\zeta_{000}$  and  $\zeta_{110}$ ), the two quadrupole 3PCFs ( $\zeta_{202}$  and  $\zeta_{112}$ ), and the first terms of the monopole and quadrupole 3PCFs ( $\zeta_{000}$  and  $\zeta_{202}$ ), respectively. These three cases will highlight the importance of simultaneously considering both monopoles and quadrupoles in the 3PCF. Moreover, Cases 5, 6, and 7 reveal the extent to which the final results can be improved by adding higher-order multipole components to Case 4. Finally, Case 8 only uses the higher-order multipoles,  $\zeta_{110}$  and  $\zeta_{112}$ , for the monopole and quadrupole components.

We summarise the results of the Fisher analysis in Table 4. In Horndeski and DHOST theories, the case 2 results show that using only the monopole 3PCFs very weakly constrains the non-linear velocity parameters  $G_s\sigma_8$  and  $G_t\sigma_8$ . On the other hand, in Case 3, using only the quadrupole 3PCFs, we can mildly constrain the non-linear coefficients of both the density field and the velocity field. The reason is that the density and velocity fluctuations contribute to the quadrupole 3PCFs to the same extent (Figure 2). Moreover, Cases 4, 5, 6, 7, and 8, using both the monopole and quadrupole components, can constrain the non-linear coefficients more strongly than Cases 2 and 3. In particular, for the  $G_s\sigma_8$  and  $G_t\sigma_8$  constraints in DHOST theories, Case 7 is  $\sim 20$  and  $\sim 40$  times better than Case 2, respectively:

$$\begin{aligned}
 \sigma_{\text{fisher}}(G_s\sigma_8) &= 35.22 \quad \text{for Case 2,} \\
 \sigma_{\text{fisher}}(G_t\sigma_8) &= 38.88 \quad \text{for Case 2,} \\
 \sigma_{\text{fisher}}(G_s\sigma_8) &= 1.519 \quad \text{for Case 7,} \\
 \sigma_{\text{fisher}}(G_t\sigma_8) &= 0.953 \quad \text{for Case 7.} \tag{7.5}
 \end{aligned}$$

These results support the argument of this paper that we should use both monopole and quadrupole 3PCFs to study the non-linearity of the velocity field.

Case 7, which uses all components of  $\zeta_{000}$ ,  $\zeta_{110}$ ,  $\zeta_{202}$ , and  $\zeta_{112}$ ,

provides the best constraints on  $F_s\sigma_8$ ,  $G_s\sigma_8$ , and  $G_t\sigma_8$ , as expected. Therefore, we can conclude that all these multipole components should be used in the MCMC analysis in Section 9.

Case 7 yields results that are about 10% better than Case 5, which uses  $\zeta_{000}$ ,  $\zeta_{110}$ , and  $\zeta_{202}$ . This result indicates that while  $\zeta_{202}$  contains the main cosmological information,  $\zeta_{112}$  contains other information in addition to  $\zeta_{202}$ . Existing studies using Scoccimarro et al. (1999)' decomposition method of the bispectrum tend to ignore the  $M \neq 0$  mode of the quadrupole component as not containing much cosmological information (e.g., Gagrani & Samushia 2017; Rizzo et al. 2023; D'Amico et al. 2022b). However, our results show the importance of the  $M \neq 0$  modes because  $\zeta_{202}$  contains only the  $M = 0$  mode, while  $\zeta_{112}$  further contains the  $M \neq 0$  modes in addition to the  $M = 0$  mode (see also Section 3.1).

By comparing the results of Case 4, consisting of  $\zeta_{000}$  and  $\zeta_{202}$ , with those of Case 8, consisting of  $\zeta_{110}$  and  $\zeta_{112}$ , we can find another viewpoint on the importance of higher-order multipole components. For example, the  $(F_s\sigma_8)$  constraint is better in Case 8, and the  $(G_s\sigma_8)$  and  $(G_t\sigma_8)$  constraints are better in Case 4. Also, the  $(G_{s,t}\sigma_8)$  result in Case 4 is only about 30% better than Case 8. Thus, although  $\zeta_{202}$  is more informative than  $\zeta_{112}$ , we interpret the information on both sides as overlapping to some extent.

We further calculate  $\sigma_{\text{fisher}}(\theta)$  for  $\theta = E_f, E_s, E_t, \xi_f, \xi_s$ , and  $\xi_t$  through the variable transformations in Eqs. (3.23) and (3.27), summarising the results in Table 5. We find that both the monopole and quadrupole components of the 3PCF are needed to constrain  $E_s$ ,  $E_t$ ,  $\xi_s$ , and  $\xi_t$  better. In Case 7, the standard deviations of  $E_s$  and  $E_t$  are more than twice larger than the fiducial values of  $E_s$  and  $E_t$ , i.e.,  $\sigma_{\text{fisher}}(E_{s,t})/(E_{s,t})_{\text{fid}} > 2$ , indicating that it is impossible to detect the  $E_s$  and  $E_t$  signals in the BOSS data. We can also confirm that for each of the  $\xi_s$  and  $\xi_t$  constraints in DHOST theories, the results of Case 7 are  $\sim 25$  and  $\sim 40$  times stronger than those of Case 2, respectively:

$$\begin{aligned}
 \sigma_{\text{fisher}}(\xi_s) &= 93.85 \quad \text{for Case 2,} \\
 \sigma_{\text{fisher}}(\xi_t) &= 171.3 \quad \text{for Case 2,} \\
 \sigma_{\text{fisher}}(\xi_s) &= 3.701 \quad \text{for Case 7,} \\
 \sigma_{\text{fisher}}(\xi_t) &= 4.172 \quad \text{for Case 7.} \tag{7.6}
 \end{aligned}$$

In GR, adding any multipole component of the 3PCF can only improve the  $b_1\sigma_8$  and  $f\sigma_8$  constraints by a few per cent. This result is consistent with the MCMC analysis of Sugiyama et al. (2021) on the Patchy mock catalogues. Furthermore, the 3PCF-specific information,  $\sigma_8$ , is also uninformative compared to  $f\sigma_8$ . Specifically,  $f\sigma_8$  can be determined with a precision of  $\sim 20\%$ , while  $\sigma_8$  can only reach a precision of  $\sim 60\%$ . These results are for large scales ( $r \geq 80 h^{-1} \text{Mpc}$ ); what happens when even smaller scales are used will be discussed in Section 7.4.

## 7.3 Fisher forecasts with all four BOSS samples

In this subsection, we repeat the analysis of Case 7 in DHOST theories, performed in Section 7.2, for the other three BOSS samples, NGC at  $z = 0.61$  and SGC at  $z = 0.38, 0.61$ , and summarise the results in Tables 6 and 7.

Table 6 shows that the results for  $(b_1\sigma_8)$  and  $(f\sigma_8)$ , which are mainly determined by the 2PCF, are slightly better for the sample at  $z = 0.61$  than for the sample at  $z = 0.38$  for both NGC and SGC. On the other hand, for the 3PCF-specific parameters,  $(F_{g,s,t}\sigma_8)$  and  $(G_{s,t}\sigma_8)$ , the error is smaller for the  $z = 0.38$  sample than for the  $z = 0.61$  sample. This result reflects the different characteristics of the cumulative S/N between the 2PCF and the 3PCF, as discussed in

DHOST							
$\sigma_{\text{fisher}}(\theta)/(\theta)_{\text{fid}}$	$(b_1\sigma_8)$	$(f\sigma_8)$	$(F_g\sigma_8)$	$(F_s\sigma_8)$	$(F_t\sigma_8)$	$(G_s\sigma_8)$	$(G_t\sigma_8)$
NGC at $z = 0.38$	0.112	0.188	0.883	0.687	1.511	2.231	2.469
NGC at $z = 0.61$	0.110	0.181	1.201	0.880	2.077	2.789	3.265
SGC at $z = 0.38$	0.188	0.311	1.446	1.142	2.609	3.642	4.123
SGC at $z = 0.61$	0.188	0.304	2.055	1.444	3.609	4.721	5.460

**Table 6.** The standard deviations computed by the Fisher analysis of Case 7 in DHOST theories divided by the fiducial values of the parameters,  $\sigma_{\text{fisher}}(\theta)/(\theta)_{\text{fid}}$ , are shown, where  $\theta = \{(b_1\sigma_8), (f\sigma_8), (F_g\sigma_8), (F_s\sigma_8), (F_t\sigma_8), (G_s\sigma_8), (G_t\sigma_8)\}$ . These results are for the NGC and SGC at  $z = 0.38, 0.61$ .

DHOST						
	$\sigma_{\text{fisher}}(E_f)/(E_f)_{\text{fid}}$	$\sigma_{\text{fisher}}(E_s)/(E_s)_{\text{fid}}$	$\sigma_{\text{fisher}}(E_t)/(E_t)_{\text{fid}}$	$\sigma_{\text{fisher}}(\xi_f)$	$\sigma_{\text{fisher}}(\xi_s)$	$\sigma_{\text{fisher}}(\xi_t)$
NGC at $z = 0.38$	0.626	2.260	2.541	1.130	3.701	4.172
NGC at $z = 0.61$	0.890	2.931	3.384	2.084	6.890	7.955
SGC at $z = 0.38$	1.035	3.653	4.234	1.867	5.983	6.950
SGC at $z = 0.61$	1.469	4.878	5.677	3.439	11.468	13.345

**Table 7.** Same as Figure 6, but  $\sigma_{\text{fisher}}(\theta)/(\theta)_{\text{fid}}$  for  $\theta = \{E_f, E_s, E_t\}$  and  $\sigma_{\text{fisher}}(\theta)$  for  $\theta = \{\xi_f, \xi_s, \xi_t\}$ .

Section 5.4. In other words, it suggests that higher number densities are more favourable than larger survey volumes for constraining the non-linear parameters,  $(F_{g,s,t}\sigma_8)$  and  $(G_{s,t}\sigma_8)$ , using 3PCF measurements.

Table 7 summarises the results of  $E_{f,s,t}$  and  $\xi_{f,s,t}$ . As expected, the  $z = 0.38$  sample gives a smaller error than the  $z = 0.61$  sample for both  $E_{f,s,t}$  and  $\xi_{f,s,t}$ . However, in the case of  $\xi_{f,s,t}$ , the error at  $z = 0.38$  is almost twice as small as that at  $z = 0.61$ , which is extremely favourable for the  $z = 0.38$  sample. For example, the  $\xi_s$  results for the NGC samples are

$$\begin{aligned} \sigma_{\text{fisher}}(\xi_s) &= 3.701 \quad \text{for NGC at } z = 0.38, \\ \sigma_{\text{fisher}}(\xi_s) &= 6.890 \quad \text{for NGC at } z = 0.61. \end{aligned} \quad (7.7)$$

This is because we parameterise the time evolution of  $E_{f,s,t}$  as  $E_{f,s,t} = \Omega_m^{\xi_{f,s,t}}$ . That is, because  $d\xi_{f,s,t} = d \ln E_{f,s,t} / (\ln \Omega_m)$ , the errors in  $\xi_{f,s,t}$  are smaller for lower redshifts with smaller values of  $\Omega_m$ . Specifically, in the LCDM model introduced in Section 1,  $\Omega_m(z = 0.38) = 0.54$  and  $\Omega_m(z = 0.61) = 0.65$ , so  $1/\ln \Omega_m(z = 0.38) = 1.62$  and  $1/\ln \Omega_m(z = 0.61) = 2.32$ . Even if  $\sigma_{\text{fisher}}(E_{f,s,t})/(E_{f,s,t})_{\text{fid}}$  has the same value at the two redshifts of  $z = 0.38$  and  $z = 0.61$ , the value of  $\sigma_{\text{fisher}}(\xi_{f,s,t})$  at  $z = 0.38$  is  $2.32/1.62 = 1.42$  times smaller than at  $z = 0.61$ .

#### 7.4 Fisher forecasts using smaller scales

So far, we have performed the Fisher analysis in the same setting as the MCMC analysis that will be performed in Section 9. There, we have dealt with the behaviour of only large scales,  $80 h^{-1} \text{ Mpc} \leq r \leq 150 h^{-1} \text{ Mpc}$ . However, seeing how the parameter constraints improve when the minimum scale used,  $r_{\text{min}}$ , is varied should be an excellent motivation for the future development of theoretical models.

Figure 10 plots  $\sigma_{\text{fisher}}(\theta)/(\theta)_{\text{fid}}$  as a function of  $r_{\text{min}}$  for the three gravity theories, GR, Horndeski, and DHOST, at two redshifts of  $z = 0.38$  (magenta lines) and  $z = 0.61$  (blue lines). The multipole components of the 2PCF and 3PCF used here are Case 7 (Eq. (7.4)). First, even on the smaller scale, adding the 3PCF hardly improves the  $f\sigma_8$  constraint compared to the case where only the 2PCF is used (compare solid and dashed lines in the top left panel of Figure 10).

On the other hand, at  $r_{\text{min}} = 30 h^{-1} \text{ Mpc}$ , the  $\sigma_8$  constraint reaches a precision of  $\sim 10\%$ , from which useful cosmological information may be extracted: e.g.,  $f = (f\sigma_8)/\sigma_8$  can be determined with a precision of  $\sim 10\%$ .

In addition, the non-linear velocity parameters,  $G_s\sigma_8$  and  $G_t\sigma_8$ , can be determined with 30-50% precision at  $r_{\text{min}} = 30 h^{-1} \text{ Mpc}$ . Thus, future galaxy surveys with even larger volumes than the BOSS survey, such as DESI, Euclid, and PFS, may detect such non-linear coefficients of the velocity field.

Note that we obtained the Fisher analysis results using the IR-resummed tree-level solutions of the 2PCF and 3PCF given in Eqs. (3.9) and (3.12). Although these models accurately describe the non-linear damping behaviour of BAO on large scales, they cannot predict the 2PCF and 3PCF on small scales with high accuracy. Therefore, to apply these models to smaller scales, it is necessary to account for non-linear effects, called loop correction terms. We leave to investigate how the results change when such a loop correction is added for future research.

#### 7.5 Flat priors

As shown by the results of the Fisher analysis in Section 7, the constraints on the non-linear parameters  $\xi_{f,s,t}$  constrained by the 3PCF measured from BOSS are weak. Therefore, we need to set appropriate priors to efficiently perform the MCMC analysis.

We use the Fisher analysis results of Case 7 in DHOST theories for the four BOSS galaxy samples, performed in Section 7.3. Then, we adopt a flat prior of  $\theta_{\text{fid}} \pm 5\sigma_{\text{fisher}}(\theta)$  as the base setting for all parameters. If using several samples to constrain common parameters, we adopt a narrower range of priors for those samples. For example, at  $z_{\text{eff}} = 0.38$ , when constraining  $f\sigma_8$  using both NGC and SGC samples, we adopt the prior computed in NGC. After this basic setting, we set a stronger prior based on further physical considerations below.

The linear bias  $b_1$ , the linear growth rate  $f$ , and  $\sigma_8$  are always positive by definition: i.e.,  $b_1\sigma_8 \geq 0$  and  $f\sigma_8 \geq 0$ .

In the case of GR, the non-linear parameters to be constrained are  $F_g\sigma_8$ ,  $\sigma_8$ , and  $F_t\sigma_8$ . The non-linear local bias parameter  $(1/2)(b_2/b_1)$  appearing in  $F_g$  is calculated to be  $-0.02$



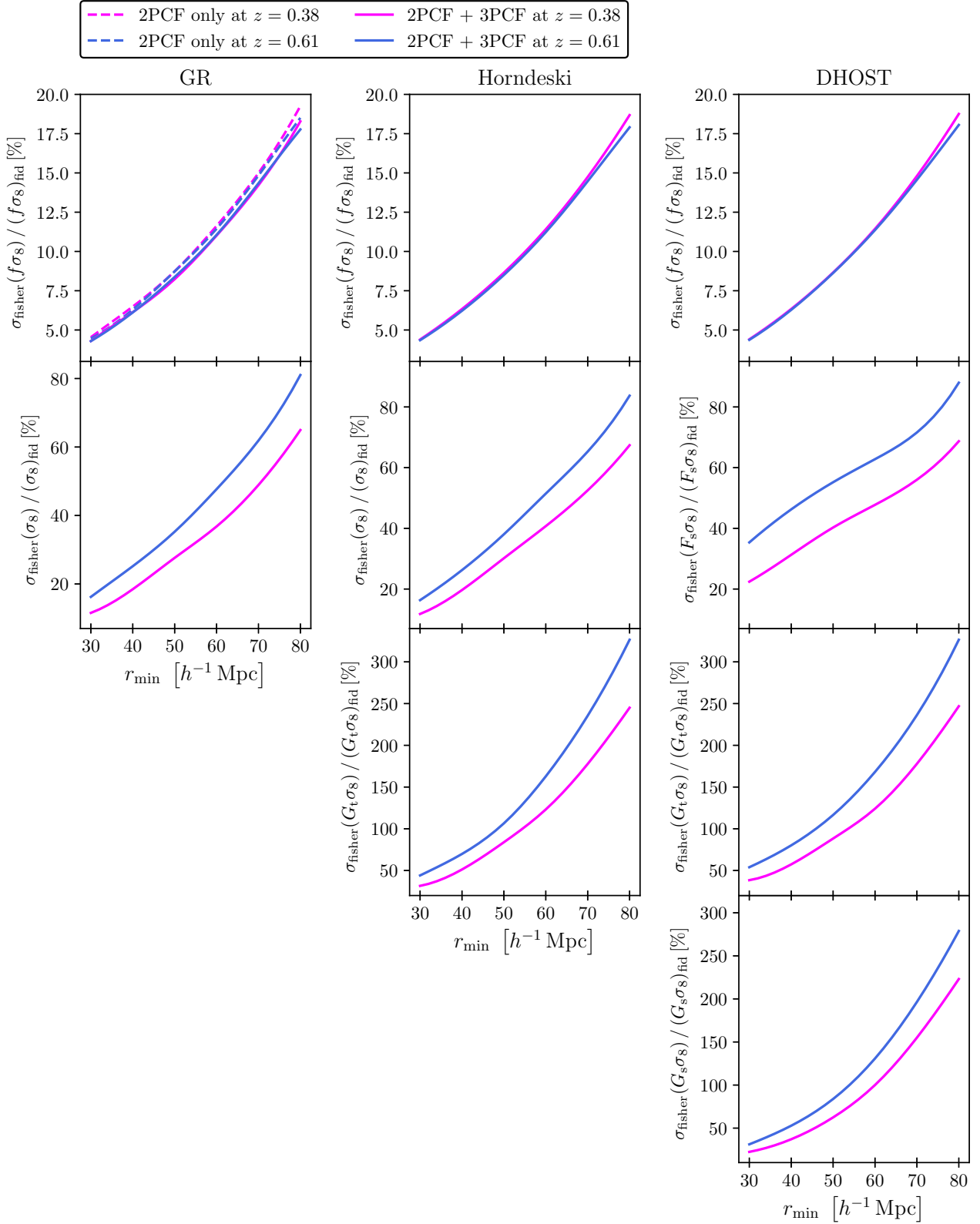


**Figure 10.** The standard deviations computed by the Fisher analysis divided by the fiducial values of the parameter,  $\sigma_{\text{fisher}}(\theta)/(\theta)_{\text{fid}}$ , are shown as a function of the minimum scale used,  $r_{\text{min}}$ . These results are for the NGC at  $z_{\text{eff}} = 0.38, 0.61$ . The solid lines show the results using the multipole components of the 2PCF and 3PCF given in Case 7 (7.4), and the dashed lines are for the 2PCF-only analysis, Case 1. The points at  $r_{\text{min}} = 80 h^{-1} \text{ Mpc}$  in the right panels correspond to the results in Table 6.

Prior range	
$(b_1\sigma_8)_{\text{NGC}, z=0.38}$	[0.60, 2.13]
$(b_1\sigma_8)_{\text{SGC}, z=0.38}$	[0.08, 2.64]
$(b_1\sigma_8)_{\text{NGC}, z=0.61}$	[0.54, 1.88]
$(b_1\sigma_8)_{\text{SGC}, z=0.61}$	[0.07, 2.36]
$(f\sigma_8)_{\text{NGC}, z=0.38}$	[0.03, 0.94]
$(f\sigma_8)_{\text{SGC}, z=0.38}$	[0.00, 1.24]
$(f\sigma_8)_{\text{NGC}, z=0.61}$	[0.05, 0.91]
$(f\sigma_8)_{\text{SGC}, z=0.61}$	[0.00, 1.21]
$(F_g\sigma_8)_{\text{NGC}, z=0.38}$	[0.00, 2.99]
$(F_g\sigma_8)_{\text{SGC}, z=0.38}$	[0.00, 4.54]
$(F_g\sigma_8)_{\text{NGC}, z=0.61}$	[0.00, 3.44]
$(F_g\sigma_8)_{\text{SGC}, z=0.61}$	[0.00, 5.54]
$(F_s\sigma_8)_{\text{NGC}, z=0.38}$	[0.00, 3.02]
$(F_s\sigma_8)_{\text{SGC}, z=0.38}$	[0.00, 4.57]
$(F_s\sigma_8)_{\text{NGC}, z=0.61}$	[0.00, 3.27]
$(F_s\sigma_8)_{\text{SGC}, z=0.61}$	[0.00, 4.99]
$(F_t\sigma_8)_{\text{NGC}, z=0.38}$	[0.00, 1.66]
$(F_t\sigma_8)_{\text{SGC}, z=0.38}$	[0.00, 2.72]
$(F_t\sigma_8)_{\text{NGC}, z=0.61}$	[0.00, 1.97]
$(F_t\sigma_8)_{\text{SGC}, z=0.61}$	[0.00, 3.29]
$(\xi_f)_{\text{NGC}, z=0.38}$	[-5.11, 6.20]
$(\xi_f)_{\text{SGC}, z=0.38}$	[-8.79, 9.88]
$(\xi_f)_{\text{NGC}, z=0.61}$	[-9.88, 10.97]
$(\xi_f)_{\text{SGC}, z=0.61}$	[-16.65, 17.74]
$(\xi_s)_{\text{NGC}, z=0.38}$	[-18.51, 11.10]
$(\xi_s)_{\text{SGC}, z=0.38}$	[-29.91, 17.95]
$(\xi_s)_{\text{NGC}, z=0.61}$	[-34.45, 20.67]
$(\xi_s)_{\text{SGC}, z=0.61}$	[-57.34, 34.40]
$(\xi_t)_{\text{NGC}, z=0.38}$	[-20.84, 12.53]
$(\xi_t)_{\text{SGC}, z=0.38}$	[-34.74, 20.86]
$(\xi_t)_{\text{NGC}, z=0.61}$	[-39.76, 23.88]
$(\xi_t)_{\text{SGC}, z=0.61}$	[-66.71, 40.05]

**Table 8.** The flat priors for the parameters that we employ in our MCMC analysis are shown. The results are calculated from Case 7 in Eq. (7.4) assuming DHOST theories.

for  $b_1 = 2.0$  using the fitting formula given by Lazeyras et al. (2016), which is sufficiently small compared to  $17/21$ . The tidal bias parameter ( $b_{s,2}/b_1$ ) appearing in  $F_t$  is also calculated to be  $b_{s,2}/b_1 = (-2/7)(1 - 1/b_1) = -0.14$  for the linear Lagrangian bias model (e.g., Desjacques et al. 2018b), and its value is also smaller than  $2/7$ . Therefore, even if the non-linear bias parameter is present,  $F_g\sigma_8$  and  $F_t\sigma_8$  are expected to be larger than zero: i.e.,  $F_g\sigma_8 \geq 0$  and  $F_t\sigma_8 \geq 0$ . We will discuss the validity of the analysis results when these conditions are imposed in Section 9.5 by comparing them with the results when  $F_g\sigma_8$  and  $F_t\sigma_8$  can take negative values.

In the cases of Horndeski and DHOST theories, the parameterisation we adopt describes the time evolution of the coefficients of the tidal and shift terms as powers of  $\Omega_m$  (Section 3.4), implicitly assuming that these coefficients are always positive: i.e.,  $F_s\sigma_8 \geq 0$ ,  $G_s\sigma_8 \geq 0$ , and  $G_t\sigma_8 \geq 0$ . For  $F_g\sigma_8$  and  $F_t\sigma_8$ , assuming that Horndeski and DHOST theories are not far from GR, we adopt  $F_g\sigma_8 \geq 0$  and  $F_t\sigma_8 \geq 0$ , just like GR.

The Fisher analysis shows that the BOSS data cannot detect the  $E_{s,t}$  signals and only give them an upper limit (Section 7). This fact means that as  $E_{s,t}$  approach zero, the parameters  $\xi_{s,t} = \log_{\Omega_m} E_{s,t}$  can be as large as desired because of  $\Omega_m < 1$ . Therefore, in this

analysis, we set the upper limit of  $\xi_{s,t}$  to  $(\xi_{s,t})_{\text{fid}} + 3\sigma_{\text{fisher}}(\xi_{s,t})$ , which is narrower than the basic setting. If  $\xi_{s,t}$  reach their upper bounds set here, we report only the lower bounds for those parameters as the final results.

We summarise the results of the above discussion in Table 8.

## 8 GOODNESS OF FIT

In this section, we examine the extent to which our analysis can give good fits to the 2PCF and 3PCF measurements from the BOSS data or Patchy mocks for a variety of cases, before presenting specific parameter constraint values in Section 9.

For this purpose, we calculate the minimum of  $\chi^2 = -2 \ln \mathcal{L}$  (6.1), denoted  $\chi_{\text{min}}^2$ , from the best-fit parameter values obtained from the joint analysis of the 2PCF and 3PCF. We use two multipole 2PCFs ( $\xi_0$  and  $\xi_2$ ), two monopole 3PCFs ( $\zeta_{000}$  and  $\zeta_{110}$ ), and two quadrupole 3PCFs ( $\zeta_{202}$  and  $\zeta_{112}$ ) in this analysis; the assumed gravity theories are GR, Horndeski, and DHOST theories. Tables 9-14 show the  $\chi_{\text{min}}^2$  divided by the degrees of freedom (DoF), i.e., the reduced  $\chi_{\text{min}}^2$ , and the corresponding one-tailed  $p$ -values. At two redshift bins,  $z = 0.38$  and  $z = 0.61$ , results are presented for NGC only, SGC only, and both NGC and SGC. In Horndeski and DHOST theories, we constrain the common parameters  $\xi_{f,s,t}$  among different redshift bins using the samples at both the redshift bins. Finally, we also include the results of the analysis using only 2PCF.

If the theoretical model fits the measurements well, the  $p$ -value should be close to 0.5. A  $p$ -value close to 1 does not mean that the theoretical model is correct, but that the theoretical model can explain the measurements within the error range, thanks to too large statistical errors in the measurements. On the other hand, a  $p$ -value close to 0 indicates that the theoretical model cannot explain the measurements. In this paper, we decide that if  $p < 0.05$ , attention should be paid to the consistency between the theoretical model and the measurements, and if  $p < 0.01$ , there is an apparent discrepancy between them. We write in bold the  $\chi^2$  and  $p$  values shown in Tables 9-14 if  $p < 0.01$ . Finally, we comment on the behaviour of  $p$ -values when combining different galaxy samples. For example, suppose that the reduced  $\chi_{\text{min}}^2$  is larger than 1: i.e.,  $\chi_{\text{min}}^2/\text{DoF} > 1$ . In this case, if we increase the values of  $\chi_{\text{min}}^2$  and DoF by an equal factor while keeping the value of the reduced  $\chi_{\text{min}}^2$ , the resulting  $p$ -value will be smaller than the original value, and conversely, if  $\chi_{\text{min}}^2/\text{DoF} < 1$ , it will be larger than the original value. Since we treat the different galaxy samples as statistically independent, a similar situation occurs in analyses with multiple galaxy samples. Thus, if the  $p$ -value obtained from each galaxy sample is small, combining galaxy samples will yield a smaller  $p$ -value.

Section 8.1 reports an unexplained discrepancy between the 3PCF measured from the BOSS galaxy data at  $z = 0.38$  and our theoretical model on large scales, even considering DHOST theories, which is beyond GR. Section 8.2 shows that this discrepancy between the data and the theoretical model appears from the monopole 3PCF. Section 8.3 shows that the discrepancy still appears even when the parameter prior set introduced in Section 7.5 is removed. Section 8.4 confirms that the discrepancy does not appear in the analysis using the Patchy mock. Finally, as a temporary measure, we rescale the covariance matrix of the 3PCF at  $z = 0.38$  to generate acceptable  $p$ -values in Section 8.5. Section 9 will report the parameter estimation results with and without rescaling the covariance matrix.

BOSS DR12			
$\chi^2_{\min}/\text{DoF}$ ( $p$ -value)			
	NGC + SGC	NGC	SGC
2PCF only ( $z_{\text{eff}} = 0.38$ )	56.04/57 (0.511)	32.18/28 (0.267)	23.36/28 (0.715)
2PCF only ( $z_{\text{eff}} = 0.61$ )	80.24/57 (0.023)	42.08/28 (0.043)	36.94/28 (0.120)
GR ( $z_{\text{eff}} = 0.38$ )	<b>488.38/396 (0.001)</b>	238.22/197 (0.024)	<b>248.72/197 (0.007)</b>
GR ( $z_{\text{eff}} = 0.61$ )	428.60/396 (0.125)	218.48/197 (0.140)	209.24/197 (0.262)
Horndeski ( $z_{\text{eff}} = 0.38$ )	<b>488.24/395 (0.001)</b>	236.38/196 (0.026)	<b>251.62/196 (0.004)</b>
Horndeski ( $z_{\text{eff}} = 0.61$ )	427.56/395 (0.125)	218.06/196 (0.134)	209.16/196 (0.247)
Horndeski ( $z_{\text{eff}} = 0.38, 0.61$ )	<b>918.76/792 (0.001)</b>	456.50/394 (0.016)	458.94/394 (0.013)
DHOST ( $z_{\text{eff}} = 0.38$ )	<b>487.48/394 (0.001)</b>	235.80/195 (0.024)	<b>248.36/195 (0.006)</b>
DHOST ( $z_{\text{eff}} = 0.61$ )	427.62/394 (0.117)	217.94/195 (0.125)	209.06/195 (0.233)
DHOST ( $z_{\text{eff}} = 0.38, 0.61$ )	<b>918.04/791 (0.001)</b>	455.96/393 (0.015)	458.88/393 (0.012)

**Table 9.** The reduced  $\chi^2$  and  $p$ -values (in round brackets) obtained from the joint analysis of the 2PCF and 3PCF are shown. These values are written in bold if  $p < 0.01$ . The minimum  $\chi^2$ , denoted  $\chi^2_{\min}$ , is calculated from the best-fit parameters. The data used is the BOSS DR12 galaxy, split into two sky regions, NGC and SGC, and two redshift bins,  $z = 0.38$  and  $z = 0.61$ . The joint analysis shows the results for three gravity theories, i.e., GR, Horndeski, and DHOST theories; for Horndeski and DHOST theories, also shown are the results using the two redshift bins to constrain the parameters  $\xi_{f,s,t}$ , which characterises the time evolution of the linear and non-linear effects of the velocity field. Furthermore, the results for the 2PCF-only analysis are shown. The combinations of the 2PCF and 3PCF multipole components used in this analysis correspond to Case 1 and Case 7 in Eq. 7.4.

## 8.1 BOSS galaxies

Table 9 shows the results from the analysis method described in this paper. We have performed the MCMC analysis (Section 6) using  $\xi_0, \xi_2, \zeta_{000}, \zeta_{110}, \zeta_{202}$ , and  $\zeta_{112}$  measured from the BOSS galaxy data (Section 4), the covariance matrix computed from the 2048 Patchy mocks (Section 5), and the flat prior of the parameter range (Section 7.5).

First, we focus on the analysis case using only the 2PCF. For the NGC+SGC sample, the obtained  $p$ -values are  $p = 0.511$  at  $z = 0.38$  and  $p = 0.023$  at  $z = 0.61$ . This  $p = 0.023$  indicates a small amount of a poor fit between the model and the measurements, but we consider it not problematic.

Next, turning to the joint analysis results of the 2PCF and 3PCF assuming GR, we find that the  $p$ -value at  $z = 0.38$  obtained for the NGC+SGC sample is extremely small, 0.001. At  $z = 0.38$ , the results for only NGC and only SGC are  $p = 0.024$  and  $p = 0.007$ , indicating that the SGC sample is more problematic than the NGC. On the other hand, the  $p$ -value at  $z = 0.61$  for the NGC+SGC sample is  $p = 0.125$ , indicating that our model explains the measured values without problems.

Finally, for Horndeski and DHOST theories, we find results similar to the GR case: the  $p$ -value is 0.001 at  $z = 0.38$  and  $p \sim 0.1$  at  $z = 0.61$  for the NGC+SGC sample.

Thus, we conclude that there is an unexplained discrepancy between the 3PCF measurement from the BOSS sample at  $z = 0.38$  and the theoretical model we are using. Even Horndeski and DHOST theories, which are modified gravity theories beyond GR, cannot explain this discrepancy.

## 8.2 Monopole- or Quadrupole-only 3PCF

We investigate whether the discrepancy between the 3PCF measurement from the galaxy sample at  $z = 0.38$  and the theoretical model, shown in Table 9, originates from the monopole or quadrupole component.

For this purpose, Tables 10 and 11 show the joint analysis results

using only monopole 3PCFs or only quadrupole 3PCFs in addition to the monopole and quadrupole 2PCFs. For a fair comparison with Table 9, the prior distributions of the parameters used here are those given in Table 8. For the NGC+SGC at  $z = 0.38$ , the  $p$ -value obtained using the monopole 3PCFs is less than 0.01 in all three gravity theories, whereas the  $p$ -value obtained using the quadrupole 3PCFs is  $p \sim 0.1$ . Therefore, we can conclude that the monopole component of the 3PCF measurement at  $z = 0.38$  is inconsistent with the theoretical model.

## 8.3 No prior in DHOST theories

As an attempt to explain the discrepancy between the 3PCF measurement from the galaxy sample at  $z = 0.38$  and the theoretical model, we remove all flat prior for the non-linear parameters,  $F_g\sigma_8, F_s\sigma_8, F_t\sigma_8, \xi_f, \xi_s$ , and  $\xi_t$ , set in Table 8 and perform parameter fitting without imposing any prior. In particular, we investigate the possibility that imposing the conditions  $F_g \geq 0$  and  $F_t \geq 0$  on the parameters with the non-linear bias may have caused some problems fitting the monopole 3PCF. This subsection focuses on DHOST theories because they have the largest number of parameters to be varied.

Table 12 summarises the results of the calculations and confirms that the  $p$ -value obtained from the NGC+SGC sample at  $z = 0.38$  is 0.001, even if we assume no prior for the non-linear parameters. Therefore, we can conclude that the discrepancy between the galaxy data and the theoretical model at  $z = 0.38$  is not due to the prior imposed in Table 8.

## 8.4 Patchy mocks

Table 13 shows the means and standard deviations of the  $\chi^2_{\min}$  and the corresponding means and  $1\sigma$  errors of the  $p$ -values obtained from the 100 Patchy mock catalogues. The setup for the data analysis is the same as that performed in Table 9.

In all 30 cases shown in Table 13, the mean  $p$ -values obtained are almost always  $p \gtrsim 0.5$ , both in the analysis using only the 2PCF

Joint analysis with monopole 3PCFs ( $\zeta_{000}$ and $\zeta_{110}$ ) only			
$\chi^2_{\min}/\text{DoF}$ ( $p$ -value)			
	NGC + SGC	NGC	SGC
GR ( $z_{\text{eff}} = 0.38$ )	<b>252.08/196 (0.004)</b>	122.56/97 (0.041)	127.32/97 (0.021)
GR ( $z_{\text{eff}} = 0.61$ )	216.54/196 (0.150)	109.00/97 (0.191)	106.94/97 (0.230)
Horndeski ( $z_{\text{eff}} = 0.38$ )	<b>252.02/195 (0.004)</b>	122.54/96 (0.035)	127.30/96 (0.018)
Horndeski ( $z_{\text{eff}} = 0.61$ )	216.40/195 (0.140)	109.02/96 (0.172)	106.90/96 (0.210)
Horndeski ( $z_{\text{eff}} = 0.38, 0.61$ )	<b>469.58/392 (0.004)</b>	231.70/194 (0.033)	234.68/194 (0.024)
DHOST ( $z_{\text{eff}} = 0.38$ )	<b>251.78/194 (0.003)</b>	122.48/95 (0.030)	127.28/95 (0.015)
DHOST ( $z_{\text{eff}} = 0.61$ )	216.40/194 (0.129)	108.96/95 (0.155)	106.90/95 (0.190)
DHOST ( $z_{\text{eff}} = 0.38, 0.61$ )	<b>469.86/391 (0.004)</b>	231.78/193 (0.029)	234.94/193 (0.021)

**Table 10.** Same as Table 9, except that only the monopole component of the 3PCF is used in the joint analysis of the 2PCF and 3PCF. The combination of the 2PCF and 3PCF multipole components used in this analysis corresponds to Case 2 in Eq. (7.4).

Joint analysis with quadrupole 3PCFs ( $\zeta_{202}$ and $\zeta_{112}$ ) only			
$\chi^2_{\min}/\text{DoF}$ ( $p$ -value)			
	NGC + SGC	NGC	SGC
GR ( $z_{\text{eff}} = 0.38$ )	280.18/252 (0.107)	146.56/125 (0.091)	132.68/125 (0.302)
GR ( $z_{\text{eff}} = 0.61$ )	281.58/252 (0.097)	148.04/125 (0.078)	132.48/125 (0.306)
Horndeski ( $z_{\text{eff}} = 0.38$ )	279.66/251 (0.103)	144.68/124 (0.099)	132.38/124 (0.287)
Horndeski ( $z_{\text{eff}} = 0.61$ )	281.68/251 (0.089)	148.14/124 (0.069)	132.48/124 (0.285)
Horndeski ( $z_{\text{eff}} = 0.38, 0.61$ )	563.66/504 (0.034)	294.48/250 (0.028)	265.08/250 (0.245)
DHOST ( $z_{\text{eff}} = 0.38$ )	279.18/250 (0.099)	144.52/123 (0.090)	132.28/123 (0.268)
DHOST ( $z_{\text{eff}} = 0.61$ )	281.68/250 (0.082)	148.04/123 (0.062)	132.50/123 (0.263)
DHOST ( $z_{\text{eff}} = 0.38, 0.61$ )	563.26/503 (0.032)	294.66/249 (0.025)	265.24/249 (0.229)

**Table 11.** Same as Table 9, except that only the quadrupole component of the 3PCF is used in the joint analysis of the 2PCF and 3PCF. The combination of the 2PCF and 3PCF multipole components used in this analysis corresponds to Case 3 in Eq. (7.4).

No prior in DHOST			
$\chi^2_{\min}/\text{DoF}$ ( $p$ -value)			
	NGC + SGC	NGC	SGC
DHOST ( $z_{\text{eff}} = 0.38$ )	<b>486.14/394 (0.001)</b>	235.80/195 (0.024)	<b>246.28/195 (0.008)</b>
DHOST ( $z_{\text{eff}} = 0.61$ )	428.16/394 (0.114)	218.58/195 (0.119)	209.58/195 (0.225)
DHOST ( $z_{\text{eff}} = 0.38, 0.61$ )	<b>916.04/791 (0.001)</b>	458.02/393 (0.013)	456.78/393 (0.014)

**Table 12.** The analysis is repeated as in Table 9, except that the prior is removed for all parameters related to non-linear effects in DHOST theories,  $F_g\sigma_8$ ,  $F_s\sigma_8$ ,  $F_t\sigma_8$ ,  $\xi_f$ ,  $\xi_s$ , and  $\xi_t$ , allowing them to vary from  $-\infty$  to  $+\infty$ .

and in the joint analysis with the 3PCF. This result means that our 2PCF and 3PCF theoretical templates fit well with the Patchy mock simulation data, indicating that the small  $p$ -values found in Table 9 are a peculiar property of the BOSS galaxies.

As two representative examples, the rest of this subsection focuses on the DHOST theory analyses using only the SGC sample at  $z = 0.38$  and all four galaxy samples (NGC+SGC at  $z = 0.38, 0.61$ ). The reasons are as follows: (1) our primary goal is to test DHOST theories; (2) the analysis of the SGC at  $z = 0.38$  in the BOSS data gives a  $p$ -value of 0.006, which is the most significant discrepancy from the theoretical model among the four galaxy samples; (3) the analysis using all four BOSS galaxy samples gives our final results in Section 9.

For the SGC sample at  $z = 0.38$ , the  $\chi^2_{\min}$  values for the BOSS samples and the Patchy mocks are

$$\begin{aligned}\chi^2_{\min}(\text{BOSS}) &= 248.36, \\ \chi^2_{\min}(\text{Patchy mocks}) &= 180.39 \pm 21.43,\end{aligned}\quad (8.1)$$

where  $\text{DoF} = 195$ . The above result means that assuming that the  $\chi^2_{\min}$  follows a Gaussian distribution, the BOSS galaxy sample deviates from the Patchy mocks at the  $3.2\sigma$  significance level.

For the NGC+SGC sample at  $z = 0.38, 0.61$ , we have

$$\begin{aligned}\chi^2_{\min}(\text{BOSS}) &= 918.04, \\ \chi^2_{\min}(\text{Patchy mocks}) &= 728.23 \pm 37.03\end{aligned}\quad (8.2)$$

where  $\text{DoF} = 791$ . This result implies a discrepancy between the



MultiDark-Patchy mocks			
$\chi_{\min}^2/\text{DoF}$ ( $p$ -value)			
	NGC + SGC	NGC	SGC
2PCF only ( $z_{\text{eff}} = 0.38$ )	$(57.76 \pm 12.25)/57$ ( $0.447^{+0.416}_{-0.331}$ )	$(28.84 \pm 7.92)/28$ ( $0.421^{+0.408}_{-0.297}$ )	$(27.75 \pm 8.15)/28$ ( $0.478^{+0.401}_{-0.332}$ )
2PCF only ( $z_{\text{eff}} = 0.61$ )	$(56.50 \pm 9.54)/57$ ( $0.494^{+0.332}_{-0.301}$ )	$(27.99 \pm 6.79)/28$ ( $0.465^{+0.352}_{-0.289}$ )	$(27.52 \pm 6.76)/28$ ( $0.490^{+0.345}_{-0.298}$ )
GR ( $z_{\text{eff}} = 0.38$ )	$(364.08 \pm 29.31)/396$ ( $0.873^{+0.115}_{-0.346}$ )	$(181.04 \pm 20.14)/197$ ( $0.786^{+0.186}_{-0.382}$ )	$(180.91 \pm 21.55)/197$ ( $0.788^{+0.189}_{-0.408}$ )
GR ( $z_{\text{eff}} = 0.61$ )	$(362.41 \pm 24.97)/396$ ( $0.886^{+0.099}_{-0.274}$ )	$(179.10 \pm 18.41)/197$ ( $0.815^{+0.158}_{-0.339}$ )	$(181.45 \pm 18.02)/197$ ( $0.780^{+0.181}_{-0.342}$ )
Horndeski ( $z_{\text{eff}} = 0.38$ )	$(363.90 \pm 29.45)/395$ ( $0.867^{+0.121}_{-0.353}$ )	$(180.68 \pm 20.20)/196$ ( $0.777^{+0.193}_{-0.386}$ )	$(180.62 \pm 21.48)/196$ ( $0.778^{+0.197}_{-0.410}$ )
Horndeski ( $z_{\text{eff}} = 0.61$ )	$(361.99 \pm 25.00)/395$ ( $0.882^{+0.102}_{-0.278}$ )	$(178.48 \pm 18.49)/196$ ( $0.810^{+0.162}_{-0.343}$ )	$(181.21 \pm 17.92)/196$ ( $0.768^{+0.189}_{-0.344}$ )
Horndeski ( $z_{\text{eff}} = 0.38, 0.61$ )	$(728.47 \pm 36.96)/792$ ( $0.948^{+0.048}_{-0.203}$ )	$(360.88 \pm 25.46)/394$ ( $0.883^{+0.102}_{-0.284}$ )	$(363.77 \pm 26.65)/394$ ( $0.860^{+0.122}_{-0.319}$ )
DHOST ( $z_{\text{eff}} = 0.38$ )	$(363.26 \pm 29.37)/394$ ( $0.865^{+0.123}_{-0.355}$ )	$(180.14 \pm 20.18)/195$ ( $0.770^{+0.199}_{-0.388}$ )	$(180.39 \pm 21.43)/195$ ( $0.766^{+0.207}_{-0.412}$ )
DHOST ( $z_{\text{eff}} = 0.61$ )	$(361.46 \pm 25.03)/394$ ( $0.879^{+0.105}_{-0.282}$ )	$(178.00 \pm 18.40)/195$ ( $0.803^{+0.167}_{-0.345}$ )	$(180.95 \pm 17.98)/195$ ( $0.757^{+0.197}_{-0.348}$ )
DHOST ( $z_{\text{eff}} = 0.38, 0.61$ )	$(728.23 \pm 37.03)/791$ ( $0.946^{+0.050}_{-0.208}$ )	$(360.45 \pm 25.33)/393$ ( $0.879^{+0.105}_{-0.286}$ )	$(363.47 \pm 26.59)/393$ ( $0.855^{+0.127}_{-0.322}$ )

**Table 13.** Same as Table 9, except that the  $\chi_{\min}^2$  is calculated from each of 100 Patchy mocks, showing their mean values and standard deviations, and the means and  $1\sigma$  errors of the corresponding  $p$ -values.

BOSS galaxy sample and the Patchy mocks at the  $5.1\sigma$  level. Thus, we conclude that the discrepancy with the theoretical model in the BOSS galaxies cannot be explained by the statistical scatter of the Patchy mocks.

Although Table 13 has shown the results obtained from 100 Patchy mocks, for a more detailed exploration, we perform MCMC analysis on all 2048 publicly available Patchy mocks for the two examples above to see if it is possible to find realizations that return the similar  $p$ -values to the BOSS galaxy sample. For the SGC sample of  $z = 0.38$ , only one Patchy mock catalogue gives  $p = 0.005$ , close to the BOSS result. In this case, the Patchy mocks have a probability of  $100 \times (1/2048) = 0.0488\%$  to reproduce the BOSS galaxy results. On the other hand, using all four galaxy samples, not a single catalogue among the 2048 Patchy mocks reproduced the BOSS results. This result means that the BOSS result has less than a 0.0488% probability of appearing in the Patchy mocks. These results are consistent with the  $3.2\sigma$  and  $5.1\sigma$  discrepancies between the BOSS and Patchy mock data presented in Eqs. (8.1) and (8.2).

Figure 11 visualizes the results for the DHOST theory analysis in Tables 9 and 13. As expected, the histogram of  $\chi_{\min}^2$  computed from the Patchy mocks (blue bars) can be well approximated by a Gaussian function (orange line) with input values for the mean and standard deviation of  $\chi_{\min}^2$  computed from the Patchy mocks. In the cases of SGC at  $z = 0.38$  (top right panel) and NGC+SGC at  $z = 0.38, 0.61$  (bottom left panel), we compute the histograms from the 2048 Patchy mocks; otherwise, we compute them from 100 Patchy mocks. Also, we plot the  $\chi_{\min}^2$  values obtained from the BOSS data in magenta.

### 8.5 Rescaling of the covariance matrix

We have discussed the discrepancy between the 3PCF measured from the BOSS data at  $z = 0.38$  and the corresponding theoretical model. Unfortunately, this paper cannot provide a definitive answer to this question.

There are three possible reasons for this discrepancy. The first concern is about the calculation of the covariance matrix. There may be physical effects that the Patchy mock used to calculate the covariance matrix needs to account for fully. For example, it is necessary to

verify to what extent non-linear galaxy bias effects (Desjacques et al. 2018b) and super-sample covariance effects (Takada & Hu 2013) are correctly included in the Patchy mock. The second concern is about the theoretical model. For example, the theoretical model may have new physical effects dominating large scales at low redshifts. If so, we also need to account for that effect in the covariance matrix simultaneously. Finally, we are concerned with the observed galaxy data. There may be unknown observational effects that the weight function in Eq. (4.1) cannot explain. In any case, the findings in this section indicate the importance of discussing the validity of cosmological analyses that consider the 2PCF and 3PCF simultaneously.

This paper assumes that the discrepancy between the BOSS galaxy sample and the theoretical model is due to an improper covariance matrix for the 3PCF calculated with the Patchy mock. Therefore, as a temporary measure, we decided to rescale the 3PCF covariance matrix at  $z = 0.38$  to increase the obtained  $p$ -value to an acceptable value. Specifically, we rescale the 3PCF covariance matrix at  $z = 0.38$  as follows:

$$\text{Cov}[3\text{PCF}]_{\text{rescaled}} = A \text{Cov}[3\text{PCF}]. \quad (8.3)$$

where the rescaling factor  $A$  is  $A = 1.15$  and  $A = 1.25$  for NGC and SGC, respectively. The values of  $A$  are determined so that the resulting  $p$ -values at  $z = 0.38$  become similar to those at  $z = 0.61$ .

Table 14 summarises the results of repeating the same analysis as Table 9 using the rescaled covariance matrix; Figure 11 visualizes the results for the DHOST theory analysis in Tables 14. As expected,  $p \gtrsim 0.1$  for the NGC+SGC sample at  $z = 0.38$ . Thus, if the discrepancy between the galaxy data and the theoretical model in the 3PCF measurement is due to the covariance matrix computed by the Patchy mocks, we find that we can solve this problem by increasing the resulting covariance matrix by 15–25%. We will give the results using this rescaled covariance matrix as the final result of this paper when we perform parameter estimation in Section 9 using the galaxy data at  $z = 0.38$ .

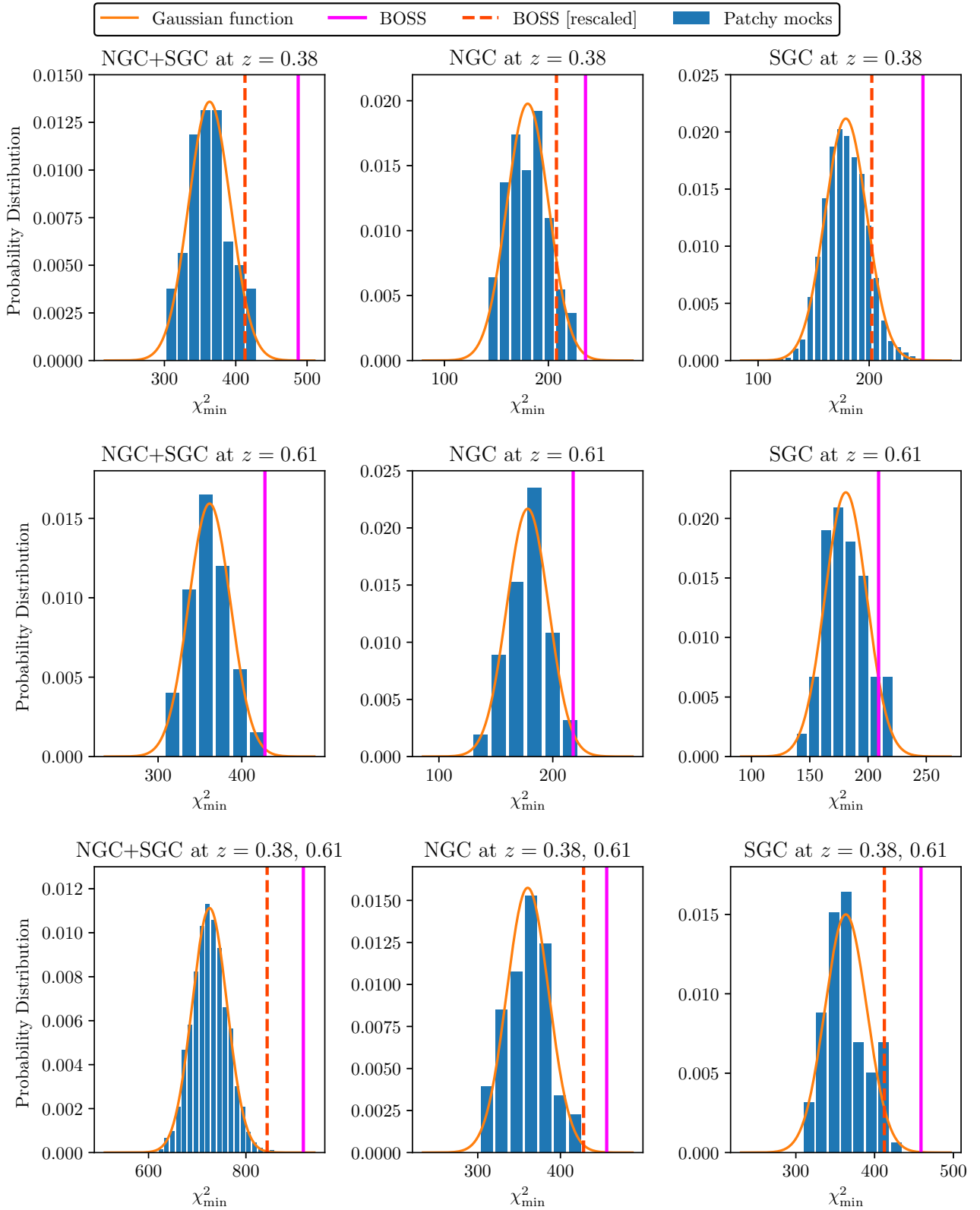


**Figure 11.** Visualizations of the DHOST theory analysis results in Tables 9, 13 and 14. The histograms of  $\chi^2_{\min}$  computed from the Patchy mocks are shown. In the cases of SGC at  $z = 0.38$  (top right panel) and NGC+SGC at  $z = 0.38, 0.61$  (bottom left panel), the histograms are computed from 2048 Patchy mocks; otherwise, they are computed from 100 Patchy mocks. Also, Gaussian functions (orange lines) with input values for the mean and standard deviation of  $\chi^2_{\min}$  computed from the Patchy mocks are shown. The  $\chi^2_{\min}$  values obtained from the BOSS data are plotted in magenta. Also shown are the results for the BOSS data using the rescaled 3PCF covariance matrix at  $z = 0.38$  (Section 8.5) in dashed red lines.

	$\chi^2_{\min}/\text{DoF}$ ( $p$ -value)		
	NGC + SGC	NGC	SGC
GR ( $z_{\text{eff}} = 0.38$ [rescaled])	413.86/396 (0.258)	209.98/197 (0.250)	202.56/197 (0.378)
Horndeski ( $z_{\text{eff}} = 0.38$ [rescaled])	413.66/395 (0.249)	208.24/196 (0.261)	202.36/196 (0.363)
Horndeski ( $z_{\text{eff}} = 0.38$ [rescaled], 0.61)	844.18/792 (0.097)	428.14/394 (0.114)	412.46/394 (0.251)
DHOST ( $z_{\text{eff}} = 0.38$ [rescaled])	412.88/394 (0.246)	207.82/195 (0.252)	202.34/195 (0.344)
DHOST ( $z_{\text{eff}} = 0.38$ [rescaled], 0.61)	843.66/791 (0.095)	428.00/393 (0.108)	412.36/393 (0.241)

**Table 14.** Same as Table 9, except that the covariance matrix of the 3PCF at  $z = 0.38$  is rescaled as in Eq. (8.3).

## 9 RESULTS

This section calculates the mean, standard deviation,  $\pm 1\sigma$  errors, and 95% upper and lower bounds for the parameters computed from the likelihoods, where we perform parameter estimation for each BOSS DR12 galaxy and Patchy mock data. When using the Patchy mock data, we compute the mean, standard deviation,  $\pm 1\sigma$  errors, and 95% limits for the parameters from each of the 100 Patchy mocks; then, we calculate the means and standard deviations of them. All results here take into account both the NGC and SGC samples. We have already given the  $\chi^2_{\min}$  and  $p$ -values calculated from the best-fit values of the parameters in the NGC+SGC columns of Tables 9, 13, and 14.

The main results of this paper are Eqs. (9.7)-(9.10), which provide constraints in  $\xi_t$  and  $\xi_s$ . In Figure 21, we plot the one- and two-dimensional likelihood distributions corresponding to these results. Finally, we summarise the measurement results for the 3PCF multipole components ( $\zeta_{000}$ ,  $\zeta_{110}$ ,  $\zeta_{202}$ , and  $\zeta_{112}$ ) from the BOSS galaxies used in this analysis in Figures 12-19.

The combination of the 2PCF and 3PCF multipoles used in the joint analysis performed in this section corresponds to Case 7 in Eq. (7.4); the analysis using only the 2PCF corresponds to Case 1. In Section 9.10, the results of the joint analysis with only the monopole 3PCF, which corresponds to Case 2, are also presented and compared with the final results obtained from Case 7.

### 9.1 Measurements

Figures 12-19 plot the measurement results of the monopole 3PCFs ( $\zeta_{000}$  and  $\zeta_{110}$ ) and the quadrupole 3PCFs ( $\zeta_{202}$  and  $\zeta_{112}$ ) from the BOSS galaxies as a function of  $r_2$  with  $r_1$  fixed at  $50 h^{-1}$  Mpc,  $80 h^{-1}$  Mpc,  $90 h^{-1}$  Mpc,  $100 h^{-1}$  Mpc, and  $130 h^{-1}$  Mpc from top to bottom; they are shown by blue circled points with  $1\sigma$  error bars. Also plotted are the 3PCF measurements from 100 Patchy mocks (grey) and the mean from the 3PCF measurements from 2048 Patchy mocks (black). Finally, the theoretical models computed from the best-fit parameter values obtained from the DHOST theory analysis using all four BOSS samples are plotted with magenta lines; they are shown as solid lines on the scales  $r_1, r_2 \geq 80 h^{-1}$  Mpc used in the MCMC analysis and as dashed lines on smaller scales. Note that the theoretical model shown by the magenta dashed line does not need to explain the measurements from the galaxy data.

As can be seen from the lower left of Figure 14, the  $\zeta_{000}$  measured from the SGC sample at  $z = 0.38$  shows a significant discrepancy with the theoretical model on large scales, which is to be expected from the results presented in Section 8.2.

Theoretical predictions from Figures 1 and 2 indicate that the monopole and quadrupole 3PCFs have trough-shaped signals at  $r_1 = r_2$ . For example, this characteristic trough signal is seen in the blue

data points for  $\zeta_{112}$  measured in the NGC sample at  $z = 0.38$ , shown in the first and second panels from the top in the right panel of Figure 13. However, due to the significant statistical scattering in the galaxy data, the trough signal is not necessarily found in the blue points of all panels in Figures 12-19.

In particular, for the monopole 3PCF, the BAO peak appears at  $r_1 \simeq r_2 \simeq 100 h^{-1}$  Mpc. Therefore, it is expected to cancel out the trough signal, resulting in a smooth line with no irregularities when plotting the 3PCF as a function of  $r_2$  after fixing  $r_1 = 100 h^{-1}$  Mpc. For example, as seen from the second panel from the bottom in the right panel of Figure 12, the  $\zeta_{110}$  measured from the NGC sample at  $z = 0.38$  shows that the trough-shaped signal disappears from the data points. Conversely, this is evidence of a BAO signal in the monopole 3PCF. Although plotting the 3PCF as a function of  $r_1 = r_2 = r$  makes it easier to see the BAO signal from the galaxy data points (e.g., see Figure 8 and Figure 11 in Sugiyama et al. 2021), we do not plot such a figure because the subject of this paper is not the BAO signal.

### 9.2 $f\sigma_8$ constraints from the Patchy mocks in GR

Table 15 shows the  $f\sigma_8$  results obtained from the analysis of 100 Patchy mocks, assuming GR.

The standard deviations of  $f\sigma_8$  from the 2PCF-only analysis are almost identical to those obtained from the joint analysis with the 3PCF. This result is consistent with the results of the Fisher analysis in Section 7. Therefore, we can conclude that neither monopole 3PCF nor quadrupole 3PCF contributes to reducing the  $f\sigma_8$  error. Nevertheless, note that we can constrain the growth rate function  $f$  using the joint analysis with the 3PCF by combining the  $\sigma_8$  constraint in Section 9.6. Furthermore, in the context of modified gravity theories,  $f$  is extended to  $E_f$ , and Section 9.7 will constrain the parameter  $\xi_f$  characterizing its time evolution.

Looking at the mean of  $f\sigma_8$ , the results obtained in the joint analysis with the 3PCF (0.498 at  $z = 0.38$  and 0.504 at  $z = 0.61$ ) are slightly closer to the values input to the Patchy mock (0.491 and 0.485) than those obtained with the 2PCF alone (0.445 and 0.457). Thus, the 3PCF information helps reduce the bias in the  $f\sigma_8$  mean values.

### 9.3 $f\sigma_8$ constraints from the BOSS DR12 galaxies in GR

Table 16 summarises the results of the  $f\sigma_8$  constraints obtained from the BOSS galaxy under the assumption of GR. "GR ( $z = 0.38$ ) [rescaled]" means the results using the rescaled covariance matrix (Section 8.5).

Note that the standard deviation result of  $f\sigma_8$  does not change with and without rescaling the 3PCF covariance matrix at  $z = 0.38$ :

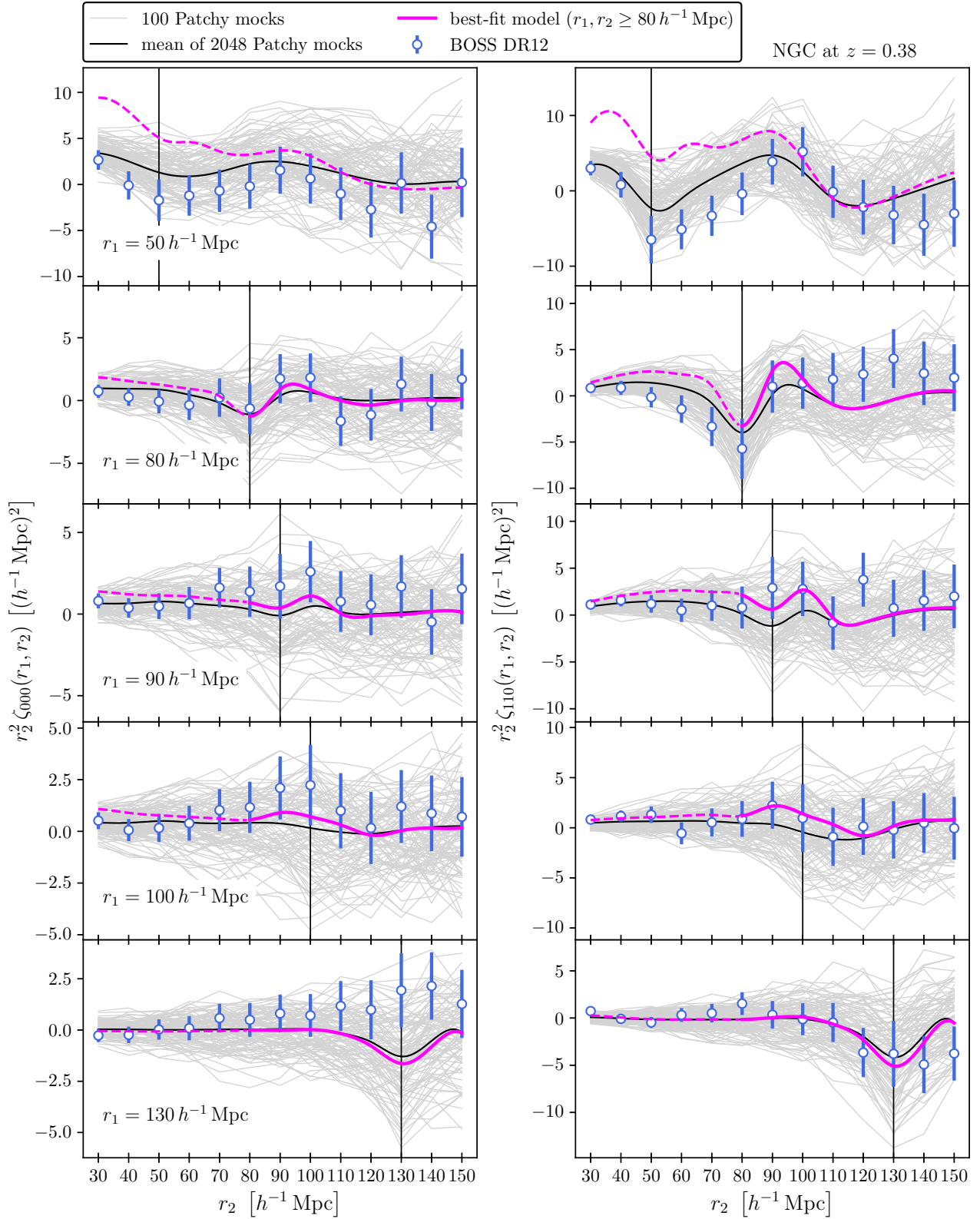


**Figure 12.** Monopole 3PCFs ( $\zeta_{000}$  and  $\zeta_{110}$ ) measured from the NGC sample at  $z = 0.38$  (blue points). These plots are shown as a function of  $r_2$ , with  $r_1$  fixed from the top to  $50 h^{-1}$  Mpc,  $80 h^{-1}$  Mpc,  $90 h^{-1}$  Mpc,  $100 h^{-1}$  Mpc, and  $130 h^{-1}$  Mpc. The error bars are the standard deviation of the 3PCF measurements computed from 2048 Patchy mocks. Also plotted are the 3PCF measurements from 100 Patchy mocks (grey) and the mean from the 3PCF measurements from 2048 Patchy mocks (black). Finally, the results of the theoretical model calculated from the best-fit parameter values obtained from the DHOST theory analysis using all four BOSS samples (Sections 9.7-9.9) are shown by the magenta lines; they are shown as solid lines on the scales  $r_1, r_2 \geq 80 h^{-1}$  Mpc used in the analysis and as dashed lines on smaller scales.



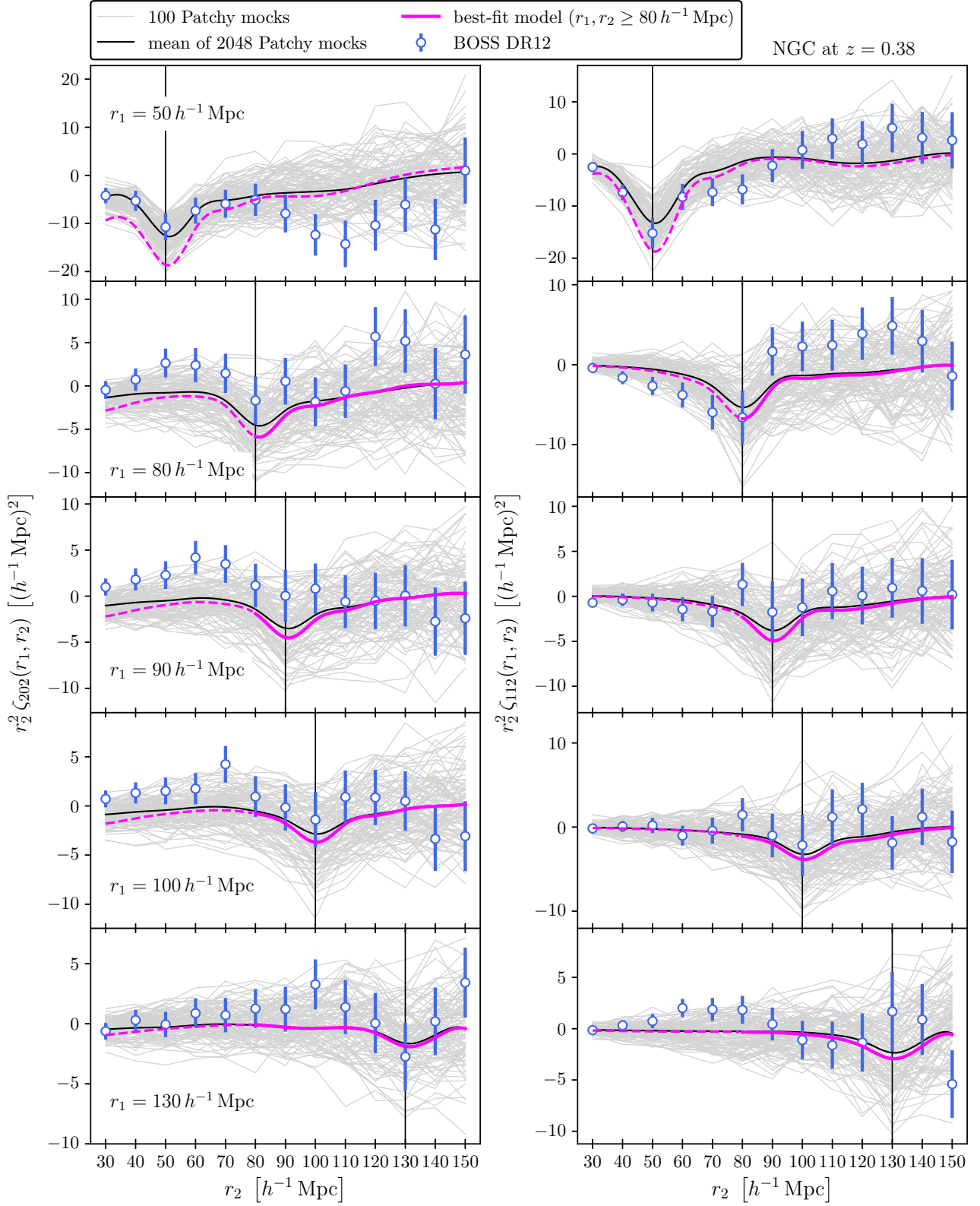
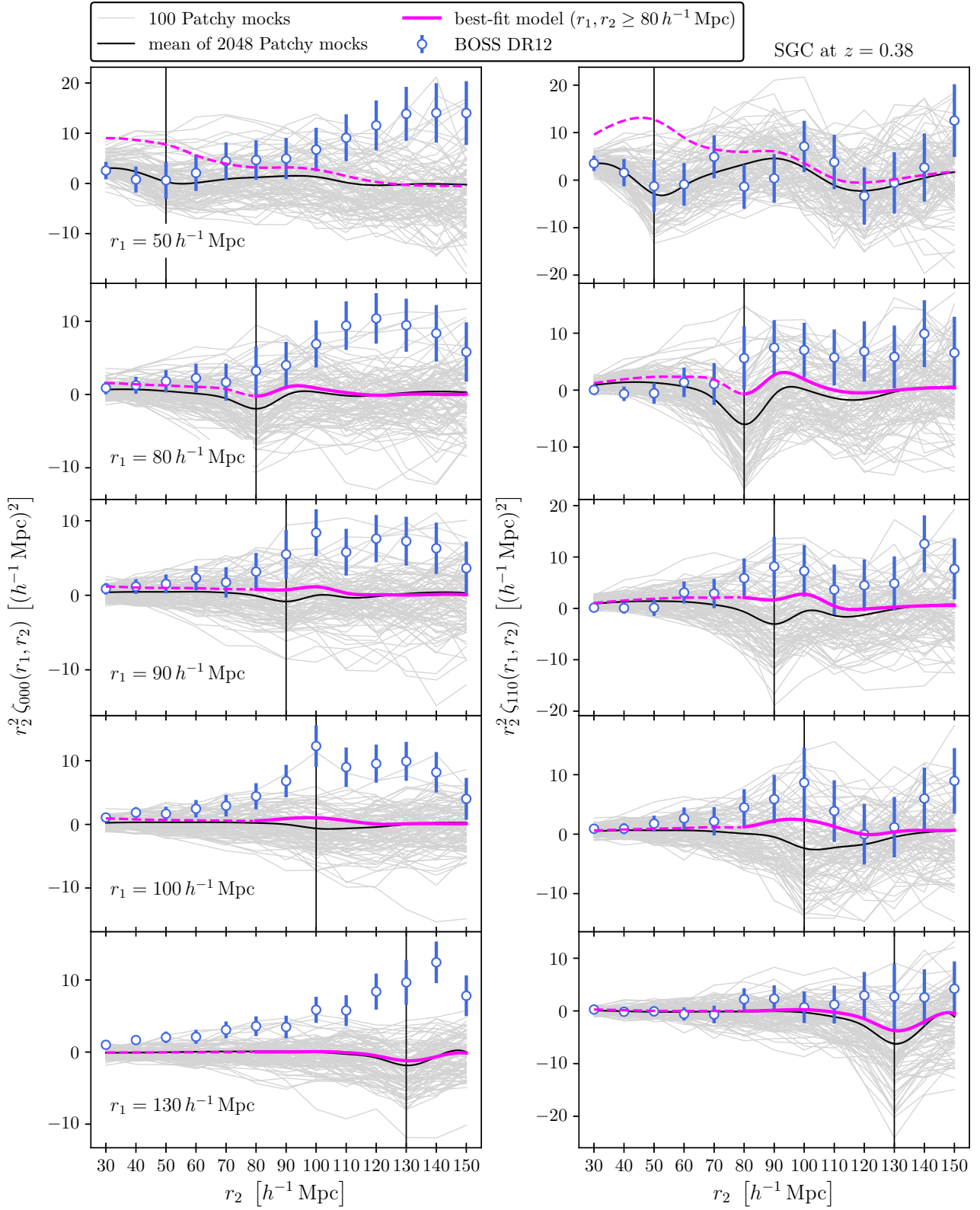


Figure 13. Same as Figure 12, except that the quadrupole 3PCF results ( $\zeta_{202}$  and  $\zeta_{112}$ ) measured from the NGC sample at  $z = 0.38$  are shown.





**Figure 14.** Same as Figure 12, except that the monopole 3PCF results ( $\zeta_{000}$  and  $\zeta_{110}$ ) measured from the SGC sample at  $z = 0.38$  are shown.

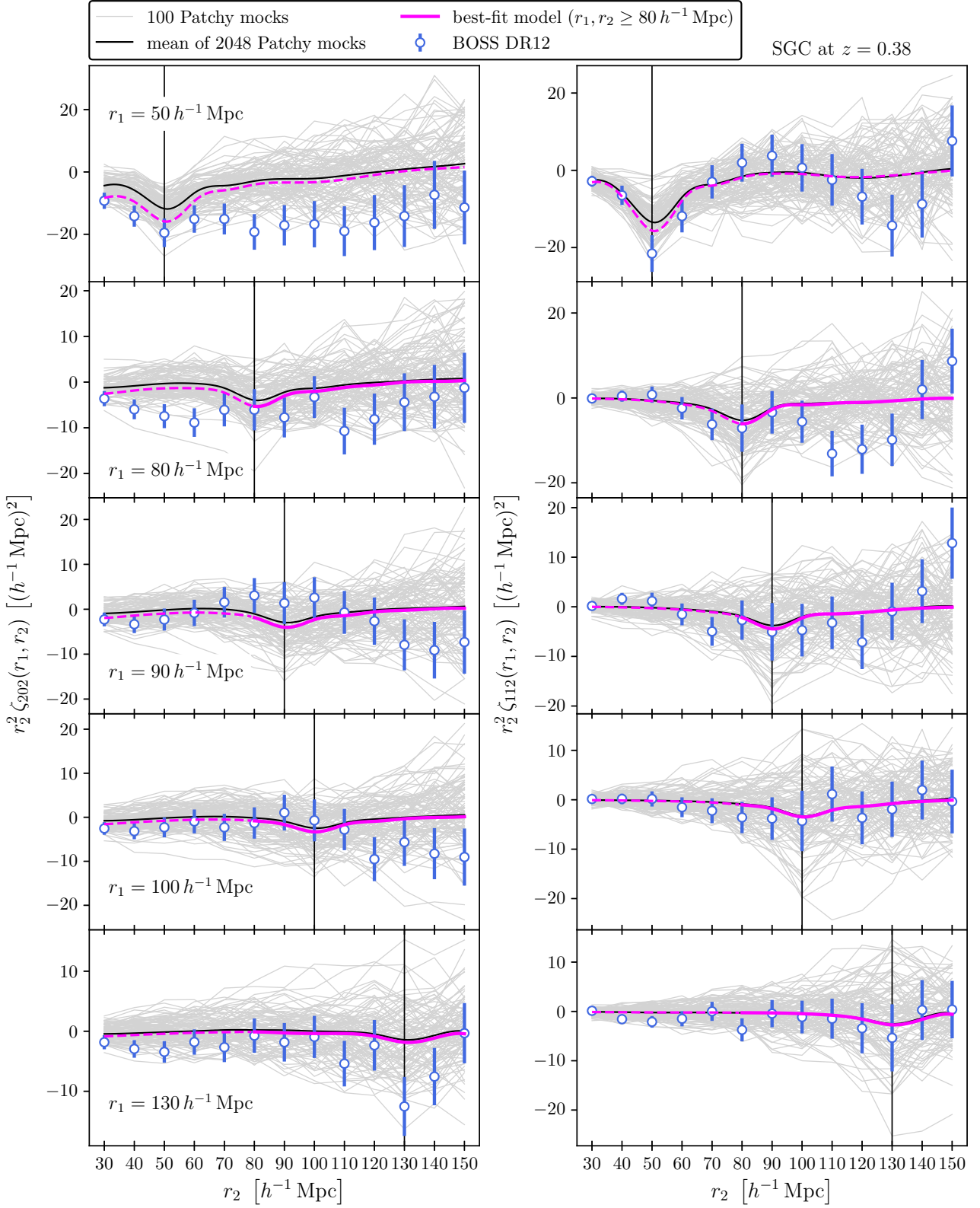
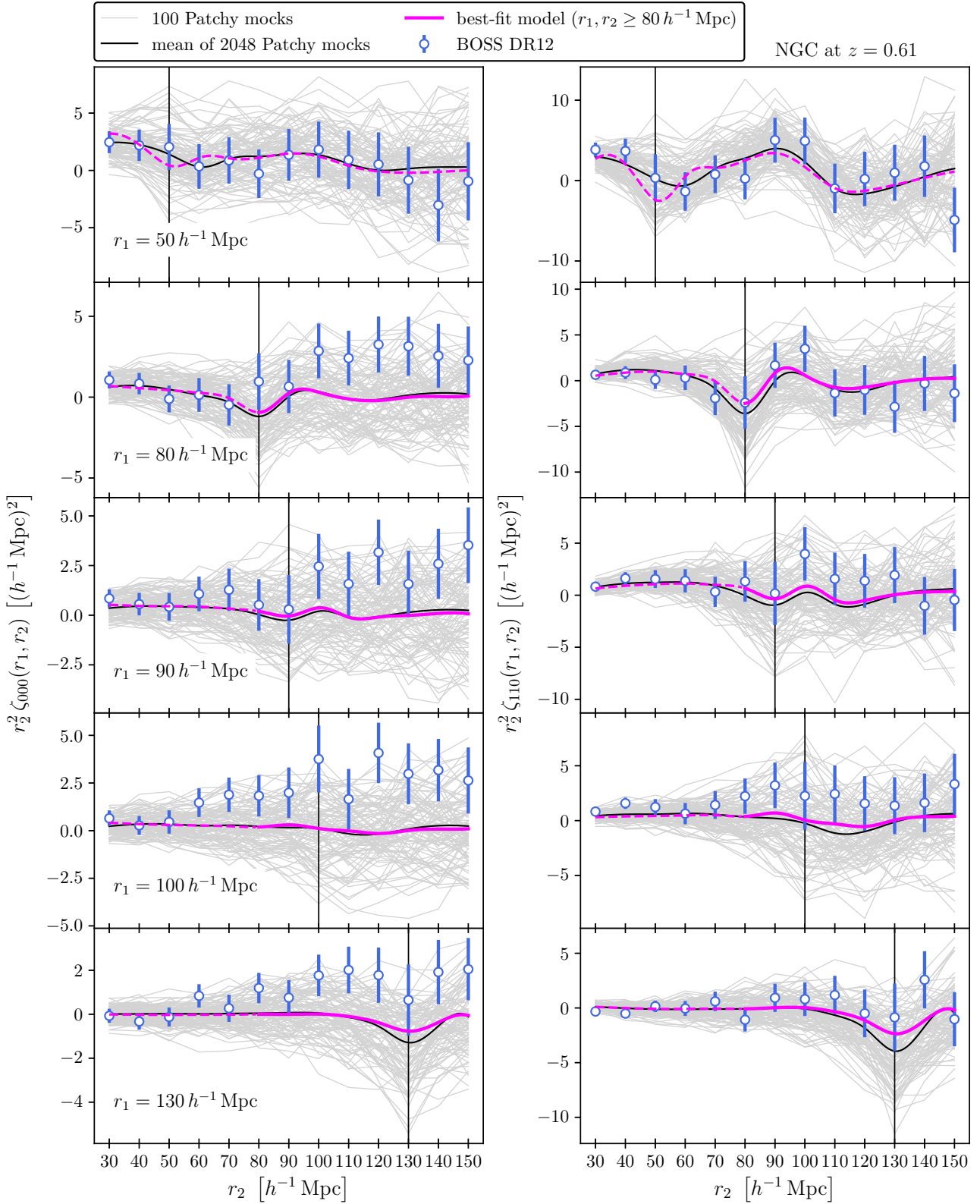
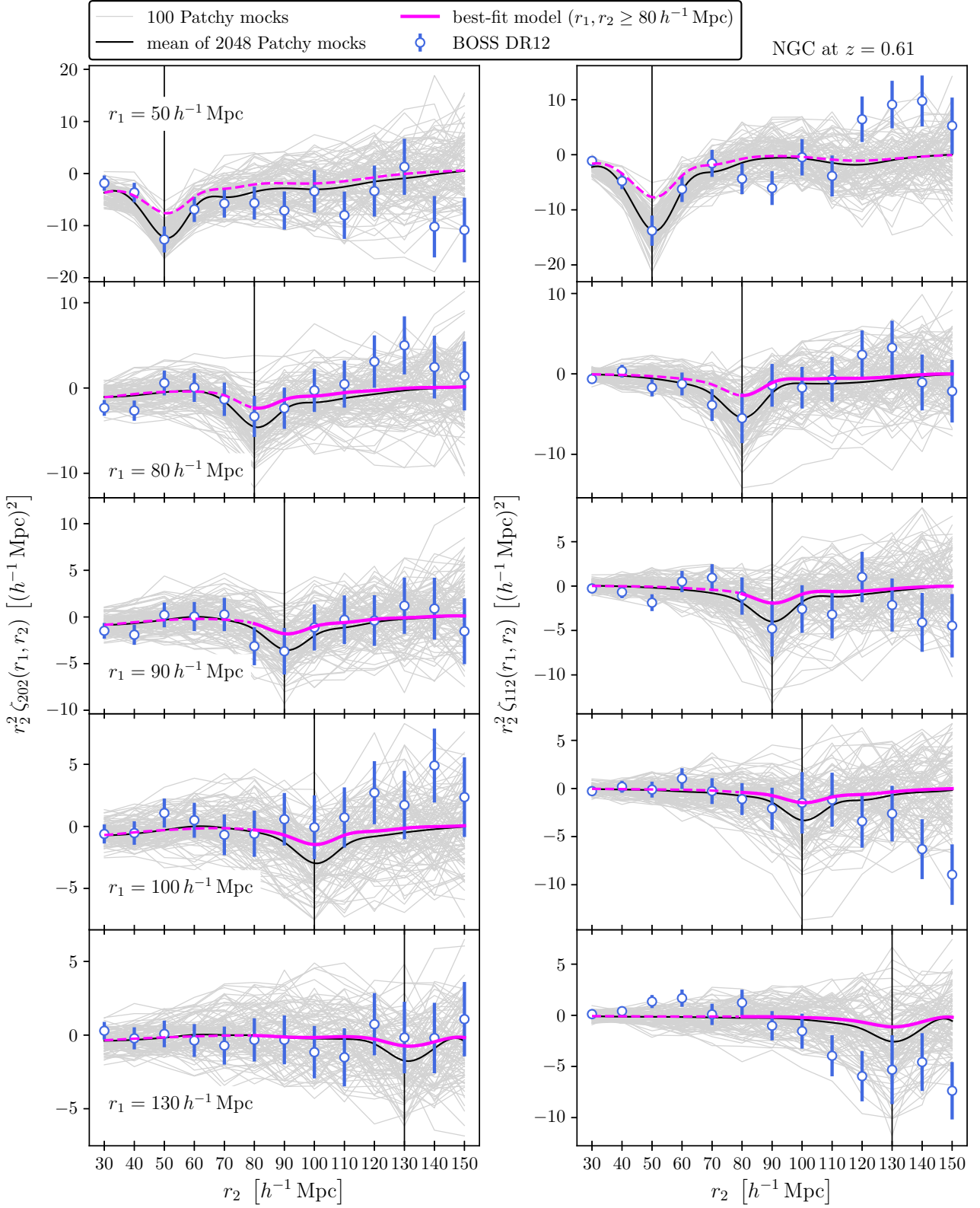


Figure 15. Same as Figure 12, except that the quadrupole 3PCF results ( $\zeta_{202}$  and  $\zeta_{112}$ ) measured from the SGC sample at  $z = 0.38$  are shown.



**Figure 16.** Same as Figure 12, except that the monopole 3PCF results ( $\zeta_{000}$  and  $\zeta_{110}$ ) measured from the NGC sample at  $z = 0.61$  are shown.



**Figure 17.** Same as Figure 12, except that the quadrupole 3PCF results ( $\zeta_{202}$  and  $\zeta_{112}$ ) measured from the NGC sample at  $z = 0.61$  are shown.



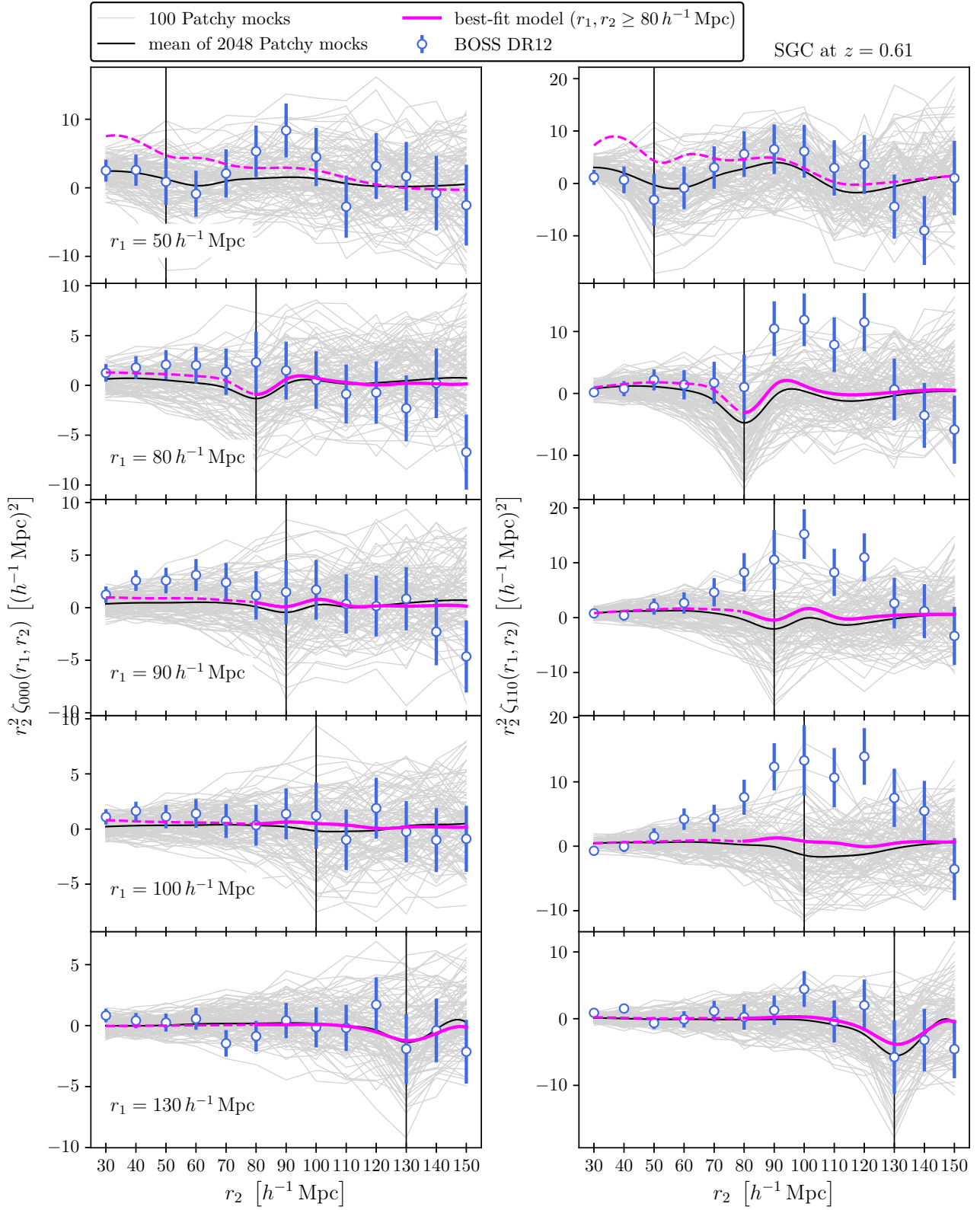


**Figure 18.** Same as Figure 12, except that the monopole 3PCF results ( $\zeta_{000}$  and  $\zeta_{110}$ ) measured from the SG sample at  $z = 0.61$  are shown.



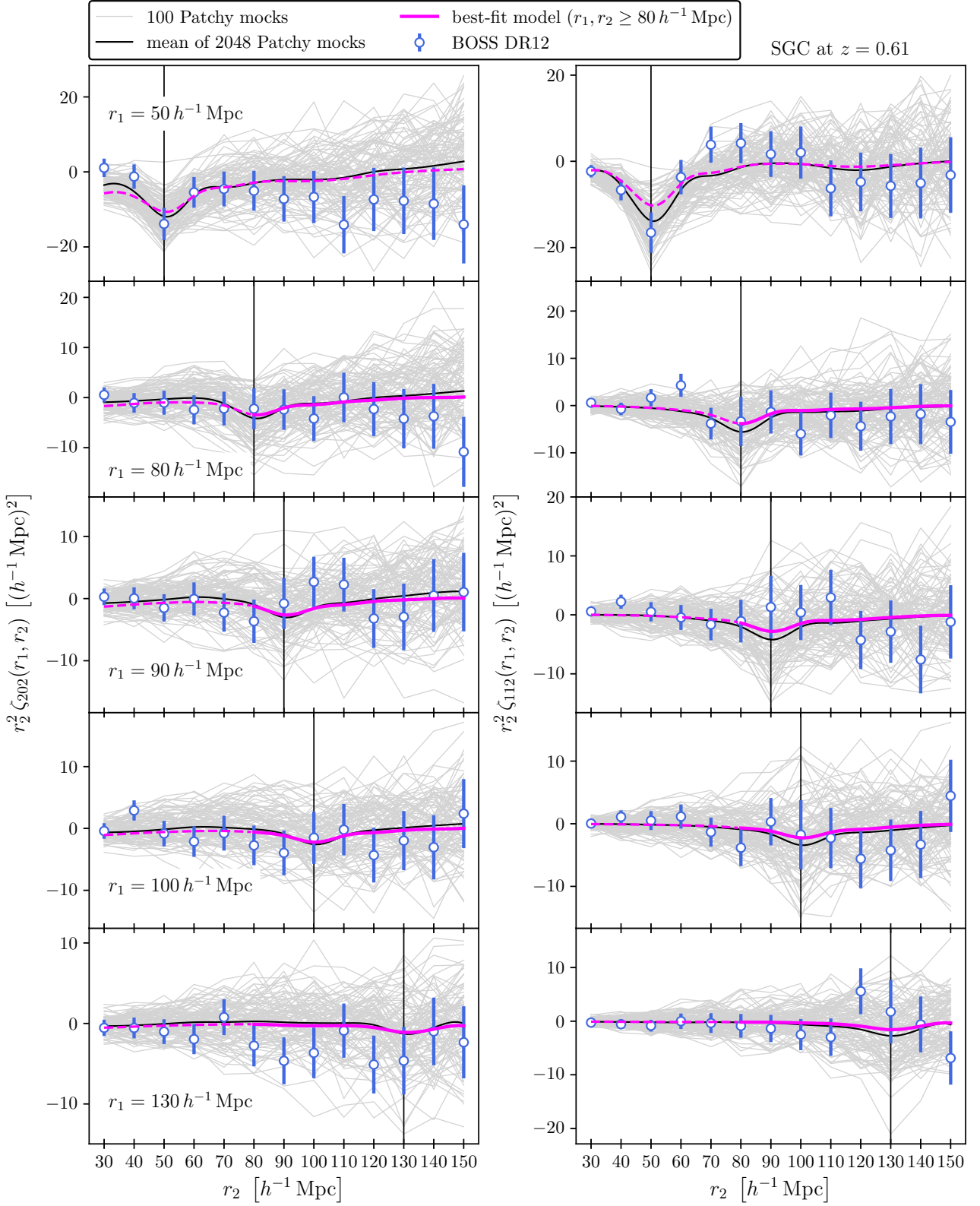


**Figure 19.** Same as Figure 12, except that the quadrupole 3PCF results ( $\zeta_{202}$  and  $\zeta_{112}$ ) measured from the SGC sample at  $z = 0.61$  are shown.

MultiDark-Patchy mocks						
	$\langle f\sigma_8 \rangle_{\text{mean}}$	$\langle f\sigma_8 \rangle_{\text{std}}$	$\langle f\sigma_8 \rangle_{-1\sigma}$	$\langle f\sigma_8 \rangle_{+1\sigma}$	$\langle f\sigma_8 \rangle_{>95\%}$	$\langle f\sigma_8 \rangle_{<95\%}$
2PCF only ( $z_{\text{eff}} = 0.38$ )	0.445 (0.491) $\pm$ 0.078	0.094 $\pm$ 0.010	-0.106 $\pm$ 0.013	0.091 $\pm$ 0.009	0.256 $\pm$ 0.074	0.635 $\pm$ 0.090
2PCF only ( $z_{\text{eff}} = 0.61$ )	0.457 (0.485) $\pm$ 0.068	0.083 $\pm$ 0.009	-0.091 $\pm$ 0.011	0.082 $\pm$ 0.008	0.291 $\pm$ 0.066	0.624 $\pm$ 0.077
GR ( $z_{\text{eff}} = 0.38$ )	0.498(0.491) $\pm$ 0.085	0.107 $\pm$ 0.008	-0.118 $\pm$ 0.009	0.105 $\pm$ 0.012	0.283 $\pm$ 0.082	0.718 $\pm$ 0.093
GR ( $z_{\text{eff}} = 0.61$ )	0.504(0.485) $\pm$ 0.070	0.095 $\pm$ 0.010	-0.104 $\pm$ 0.010	0.092 $\pm$ 0.011	0.314 $\pm$ 0.065	0.698 $\pm$ 0.082

**Table 15.** Constraint results for  $f\sigma_8$  obtained from the 100 Patchy mocks. One hundred means, standard deviations,  $\pm 1\sigma$  errors, and 95% upper and lower bounds are computed from the 100 Patchy mocks; then, the means and standard deviations of them are shown. Values in parentheses are the input values for the Patchy mocks. Results are shown for two redshift bins at  $z = 0.38$  and  $0.61$  in combination with the NGC and SGC samples. Also shown are the results for the 2PCF only analysis and the joint analysis with the 3PCF assuming GR. The  $\chi^2_{\text{min}}$  and  $p$  values corresponding to this table are shown in the NGC+SGC column of Table 13.

BOSS DR12						
	$(f\sigma_8)_{\text{mean}}$	$(f\sigma_8)_{\text{std}}$	$(f\sigma_8)_{-1\sigma}$	$(f\sigma_8)_{+1\sigma}$	$(f\sigma_8)_{>95\%}$	$(f\sigma_8)_{<95\%}$
2PCF only ( $z_{\text{eff}} = 0.38$ )	0.446	0.086	-0.096	0.084	0.273	0.620
2PCF only ( $z_{\text{eff}} = 0.61$ )	0.408	0.086	-0.095	0.084	0.236	0.580
GR ( $z_{\text{eff}} = 0.38$ )	0.561	0.108	-0.122	0.098	0.348	0.785
GR ( $z_{\text{eff}} = 0.61$ )	0.394	0.091	-0.099	0.088	0.208	0.580
GR ( $z_{\text{eff}} = 0.38$ [rescaled])	0.549	0.108	-0.122	0.097	0.337	0.776

**Table 16.** Means, standard deviations,  $\pm 1\sigma$  errors, and 95% upper and lower bounds for  $f\sigma_8$  obtained in the 2PCF-only analysis and the joint analysis with the 3PCF using the BOSS DR12 galaxies, assuming GR for the joint analysis with the 3PCF. Results are shown for two redshifts at  $z = 0.38$  and  $0.61$  using the NGC and SGC samples. Also shown are the results at  $z = 0.38$  for the analysis using the rescaled covariance matrix (8.3) to give an acceptable  $p$ -value. The  $\chi^2_{\text{min}}$  and  $p$  values corresponding to this table are shown in the NGC+SGC column of Tables 9 and 14.

i.e.,  $(f\sigma_8)_{\text{std}} = 0.108$  in both cases. Thus, the 15 – 25% difference in the 3PCF covariance matrix due to rescaling (Section 8.5) does not propagate significantly to the final  $f\sigma_8$  error. The reason for this may be mainly due to the effect of parameter degeneracy and other factors. However, due to the decisively different  $p$ -values obtained (see Tables 9 and 14), we adopt the rescaled result at  $z = 0.38$  as the final result.

Comparing the results of the joint analysis with the 3PCF and the 2PCF-only analysis, the former has a larger  $f\sigma_8$  error: i.e.,  $(f\sigma_8)_{\text{std}} = 0.108, 0.091$  at  $z = 0.38, 0.61$  for the joint analysis with the 3PCF, and  $(f\sigma_8)_{\text{std}} = 0.086, 0.086$  at  $z = 0.38, 0.61$  for the 2PCF-only analysis. Therefore, one may think that adding the 3PCF information has weakened the constraint on  $f\sigma_8$ . However, since Table 15 shows that the statistical uncertainty of  $(f\sigma_8)_{\text{std}}$  is  $\sim 0.01$ , the both results are statistically consistent at the  $\lesssim 2\sigma$  level.

Our final results for the  $f\sigma_8$  constraints are as follows. The 2PCF-only analysis gives, at the  $1\sigma$  level,

$$\begin{aligned} f\sigma_8 &= 0.446_{-0.096}^{+0.084} \quad \text{at } z = 0.38 \\ f\sigma_8 &= 0.408_{-0.095}^{+0.084} \quad \text{at } z = 0.61, \end{aligned} \quad (9.1)$$

and the joint analysis with the 3PCF presents

$$\begin{aligned} f\sigma_8 &= 0.549_{-0.122}^{+0.097} \quad \text{at } z = 0.38 \\ f\sigma_8 &= 0.394_{-0.099}^{+0.088} \quad \text{at } z = 0.61. \end{aligned} \quad (9.2)$$

These  $f\sigma_8$  constraints are consistent with the  $f\sigma_8$  values ( $f\sigma_8 = 0.485, 0.479$  at  $z = 0.38, 0.61$ ) calculated from the cosmological parameters in a flat  $\Lambda$ CDM model (Section 1) given by Planck 2018 (Aghanim et al. 2020). However, the  $f\sigma_8$  result in this analysis, which constrains  $f\sigma_8$  with a  $\sim 20\%$  precision, is not as competitive as existing constraints (e.g., Alam et al. 2017; Ivanov et al. 2020;

Lange et al. 2022; Kobayashi et al. 2022) because we only use large-scale information ( $r \geq 80 h^{-1}$  Mpc).

#### 9.4 $\sigma_8$ constraints from the Patchy mocks in GR

Table 17 summarises the results for  $\sigma_8$  from 100 Patchy mocks.

The mean values for  $\sigma_8$  are 0.741 and 0.612 for  $z = 0.38$  and  $z = 0.61$ , respectively, in good agreement with the mock input values (0.691 and 0.615). Specifically, they agree to an accuracy of 7% and 0.5%, respectively. Since  $\sigma_8$  is the only physical parameter unique to the 3PCF in GR, the fact that we can estimate the  $\sigma_8$  value with high accuracy guarantees the validity of our analysis.

On the other hand, the 95% lower limit of  $\sigma_8$  is consistent with zero, so we cannot detect a statistically significant signal for  $\sigma_8$  in our analysis.

#### 9.5 $\sigma_8$ constraints from the Patchy mocks in GR with negative $F_g\sigma_8$ and $F_t\sigma_8$ allowed

This subsection discusses the validity of the priors set in Section 7.5 for the parameters  $F_g\sigma_8$  and  $F_t\sigma_8$ , which include non-linear bias parameters. We impose the assumption that  $F_g$  and  $F_t$  are positive, but there is no theoretical requirement that this assumption is correct since the values of the non-linear biases are uncertain. Therefore, as a test, we perform parameter estimation for  $\sigma_8$  using a prior with negative  $F_g$  and  $F_t$  allowed to check if it returns the input values of the Patchy mocks. Specifically, the upper bounds of  $F_g\sigma_8$  and  $F_t\sigma_8$  given in Table 8 are multiplied by  $(-1)$  to set the lower bounds of  $F_g\sigma_8$  and  $F_t\sigma_8$ . For example, we set  $-2.99 \leq (F_g\sigma_8)_{\text{NGC}, z=0.38} \leq 2.99$ .

We summarise the results of this analysis in Table 18. This table

MultiDark-Patchy mocks						
	$\langle\sigma_8\rangle_{\text{mean}}$	$\langle\sigma_8\rangle_{\text{std}}$	$\langle\sigma_8\rangle_{-1\sigma}$	$\langle\sigma_8\rangle_{+1\sigma}$	$\langle\sigma_8\rangle_{>95\%}$	$\langle\sigma_8\rangle_{<95\%}$
GR ( $z_{\text{eff}} = 0.38$ )	$0.741 (0.691) \pm 0.347$	$0.476 \pm 0.142$	$-0.626 \pm 0.184$	$0.235 \pm 0.191$	$0.024 \pm 0.097$	$1.668 \pm 0.617$
GR ( $z_{\text{eff}} = 0.61$ )	$0.612 (0.615) \pm 0.319$	$0.415 \pm 0.165$	$-0.550 \pm 0.220$	$0.176 \pm 0.156$	$0.003 \pm 0.023$	$1.410 \pm 0.636$

**Table 17.** Constraint results for  $\sigma_8$  obtained from the 100 Patchy mocks. One hundred means, standard deviations,  $\pm 1\sigma$  errors, and 95% upper and lower bounds are computed from the 100 Patchy mocks; then, the means and standard deviations of them are shown. Values in parentheses are the input values for the Patchy mocks. Results are shown for two redshift bins at  $z = 0.38$  and  $0.61$  in combination with the NGC and SGC samples. Also shown are the results for the joint analysis with the 3PCF assuming GR. The  $\chi_{\text{min}}^2$  and  $p$  values corresponding to this table are shown in the NGC+SGC column of Table 13.

MultiDark-Patchy mocks						
Negative $F_g$ and $F_t$ allowed						
	$\langle\sigma_8\rangle_{\text{mean}}$	$\langle\sigma_8\rangle_{\text{std}}$	$\langle\sigma_8\rangle_{-1\sigma}$	$\langle\sigma_8\rangle_{+1\sigma}$	$\langle\sigma_8\rangle_{>95\%}$	$\langle\sigma_8\rangle_{<95\%}$
GR ( $z_{\text{eff}} = 0.38$ )	$1.204 (0.691) \pm 0.429$	$0.628 \pm 0.109$	$-0.771 \pm 0.184$	$0.499 \pm 0.263$	$0.151 \pm 0.269$	$2.409 \pm 0.568$
GR ( $z_{\text{eff}} = 0.61$ )	$1.004 (0.615) \pm 0.441$	$0.584 \pm 0.156$	$-0.750 \pm 0.198$	$0.374 \pm 0.260$	$0.072 \pm 0.176$	$2.140 \pm 0.719$

**Table 18.** Same as Table 17, except that a prior with negative  $F_g$  and  $F_t$  allowed is adopted.

BOSS DR12						
	$(\sigma_8)_{\text{mean}}$	$(\sigma_8)_{\text{std}}$	$(\sigma_8)_{-1\sigma}$	$(\sigma_8)_{+1\sigma}$	$(\sigma_8)_{>95\%}$	$(\sigma_8)_{<95\%}$
GR ( $z_{\text{eff}} = 0.38$ )	0.702	0.451	-0.576	0.221	0.000	1.563
GR ( $z_{\text{eff}} = 0.61$ )	0.568	0.404	-0.547	0.144	0.000	1.323
GR ( $z_{\text{eff}} = 0.38$ [rescaled])	0.692	0.459	-0.591	0.209	0.000	1.568

**Table 19.** Means, standard deviations,  $\pm 1\sigma$  errors, and 95% upper and lower bounds for  $\sigma_8$  obtained in the joint analysis of the 2PCF and 3PCF using the BOSS DR12 galaxies, assuming GR. Results are shown for two redshifts at  $z = 0.38$  and  $0.61$  using the NGC and SGC samples. Also shown are the results at  $z = 0.38$  for the analysis using the rescaled covariance matrix (8.3) to give an acceptable  $p$ -value. The  $\chi_{\text{min}}^2$  and  $p$  values corresponding to this table are shown in the NGC+SGC column of Tables 9 and 14.

shows that the mean values for  $\sigma_8$  are 1.204 at  $z = 0.38$  and 1.004 at  $z = 0.61$ , which are about 1.5 times larger than the input values, 0.691 at  $z = 0.38$  and 0.615 at  $z = 0.61$ , in the Patchy mocks. Thus, if we allow negative values of  $F_g$  and  $F_t$ , we cannot estimate the correct value of  $\sigma_8$ . We have no theoretical basis for explaining this fact, but as a result of numerical experiments, we conclude that it is reasonable to impose the conditions  $F_g \geq 0$  and  $F_t \geq 0$  in our analysis.

## 9.6 $\sigma_8$ constraints from the BOSS DR12 galaxies in GR

Table 19 summarises the results for the  $\sigma_8$  constraints obtained from the BOSS galaxies under the GR assumption. The ‘‘GR ( $z = 0.38$ ) [rescaled]’’ refers to the results obtained using the rescaled covariance matrix (Section 8.5). Figure 20 plots the marginalized one- and two-dimensional posteriors of  $f\sigma_8$  and  $\sigma_8$ .

Similar to the results for the  $f\sigma_8$  constraint in Section 9.3, the results for the  $\sigma_8$  constraint remain almost the same whether the covariance matrix is rescaled or not. Adopting the result using the rescaled covariance matrix as the final result, the  $\sigma_8$  constraints at the  $1\sigma$  level are

$$\begin{aligned} \sigma_8 &= 0.692_{-0.591}^{+0.209} \quad \text{at } z = 0.38, \\ \sigma_8 &= 0.568_{-0.547}^{+0.144} \quad \text{at } z = 0.61, \end{aligned} \quad (9.3)$$

Also, as expected from the results of the Patchy mocks, the 95%

lower bounds for  $\sigma_8$  reach 0, so at the 95% level, we get only the upper bounds:

$$\begin{aligned} \sigma_8 &< 1.568 \text{ (95\% CL)} \quad \text{at } z = 0.38, \\ \sigma_8 &< 1.323 \text{ (95\% CL)} \quad \text{at } z = 0.61. \end{aligned} \quad (9.4)$$

These results are consistent with the  $\sigma_8$  values, ( $\sigma_8 = 0.681, 0.606$  at  $z = 0.38, 0.61$ ), calculated from the cosmological parameters in a flat  $\Lambda$ CDM model given by Planck 2018 (Section 1).

The ratio of the standard deviation to the mean for  $\sigma_8$  is  $(\sigma_8)_{\text{std}}/(\sigma_8)_{\text{mean}} = 0.66$  at  $z = 0.38$  and  $0.71$  at  $z = 0.61$ , indicating that the galaxy sample at  $z = 0.38$  provides a better constraint on  $\sigma_8$ . This result is consistent with the Fisher analysis in Section 7.3.

## 9.7 $\xi_f$ constraints from the BOSS DR12 galaxies in Horndeski and DHOST theories

Table 20 summarises the constraint results for the parameter  $\xi_f$ , defined as  $\xi_f = \ln_{\Omega_m}(E_f) = \ln_{\Omega_m}(f/\kappa_\delta)$  (3.27), characterising the time evolution of the amplitude of the linear velocity field. In GR and Horndeski theories,  $\xi_f$  corresponds to the well-known parameter  $\gamma$  since  $\kappa_\delta = 1$ ; in GR,  $\xi_f = \gamma = 6/11$  (3.28).

BOSS DR12						
	$(\xi_f)_{\text{mean}}$	$(\xi_f)_{\text{std}}$	$(\xi_f)_{-1\sigma}$	$(\xi_f)_{+1\sigma}$	$(\xi_f)_{>95\%}$	$(\xi_f)_{<95\%}$
Horndeski ( $z_{\text{eff}} = 0.38$ )	0.206	1.016	-0.777	1.176	-1.906	2.201
Horndeski ( $z_{\text{eff}} = 0.61$ )	1.142	1.671	-1.431	1.862	-2.302	4.480
Horndeski ( $z_{\text{eff}} = 0.38, 0.61$ )	0.562	0.818	-0.703	0.913	-1.079	2.226
Horndeski ( $z_{\text{eff}} = 0.38$ [rescaled])	0.202	1.043	-0.833	1.201	-1.921	2.287
Horndeski ( $z_{\text{eff}} = 0.38$ [rescaled], 0.61)	0.485	0.839	-0.708	0.967	-1.216	2.175
DHOST ( $z_{\text{eff}} = 0.38$ )	0.458	1.013	-0.790	1.188	-1.564	2.474
DHOST ( $z_{\text{eff}} = 0.61$ )	1.248	1.722	-1.372	1.981	-2.318	4.630
DHOST ( $z_{\text{eff}} = 0.38, 0.61$ )	0.834	0.829	-0.686	0.963	-0.814	2.484
DHOST ( $z_{\text{eff}} = 0.38$ [rescaled])	0.129	1.131	-0.895	1.078	-2.096	2.473
DHOST ( $z_{\text{eff}} = 0.38$ [rescaled], 0.61)	0.791	0.830	-0.691	0.963	-0.907	2.447

**Table 20.** Means, standard deviations,  $\pm 1\sigma$  errors, and 95% upper and lower bounds for  $\xi_f$  obtained in the joint analysis of the 2PCF and 3PCF using the BOSS DR12 galaxies, assuming Horndeski or DHOST theories. The results for the two redshifts,  $z = 0.38$  and  $0.61$ , and their combined case are shown. Both NGC and SGC samples are used for all cases. Also shown are the results at  $z = 0.38$  for the analysis using the rescaled covariance matrix (8.3) to give acceptable  $p$ -values. The  $\chi^2_{\text{min}}$  and  $p$  values corresponding to this table are shown in the NGC+SGC column of Tables 9 and 14.

BOSS DR12						
	$(\xi_t)_{\text{mean}}$	$(\xi_t)_{\text{std}}$	$(\xi_t)_{-1\sigma}$	$(\xi_t)_{+1\sigma}$	$(\xi_t)_{>95\%}$	$(\xi_t)_{<95\%}$
Horndeski ( $z_{\text{eff}} = 0.38$ )	4.221	4.693	-5.982	5.710	-3.380	-
Horndeski ( $z_{\text{eff}} = 0.61$ )	11.118	7.354	-7.204	9.639	-1.256	-
Horndeski ( $z_{\text{eff}} = 0.38, 0.61$ )	5.298	4.257	-4.023	6.092	-1.865	-
Horndeski ( $z_{\text{eff}} = 0.38$ [rescaled])	4.129	4.704	-5.968	5.268	-3.485	-
Horndeski ( $z_{\text{eff}} = 0.38$ [rescaled], 0.61)	5.151	4.300	-4.016	6.112	-2.098	-
DHOST ( $z_{\text{eff}} = 0.38$ )	4.288	4.589	-6.002	5.348	-3.103	-
DHOST ( $z_{\text{eff}} = 0.61$ )	11.361	7.387	-6.785	10.112	-1.183	-
DHOST ( $z_{\text{eff}} = 0.38, 0.61$ )	5.349	4.217	-3.980	5.915	-1.688	-
DHOST ( $z_{\text{eff}} = 0.38$ [rescaled])	3.745	4.732	-6.165	5.262	-3.921	-
DHOST ( $z_{\text{eff}} = 0.38$ [rescaled], 0.61)	5.414	4.211	-3.734	6.007	-1.655	-

**Table 21.** Same as Table 20, except that the results for  $\xi_t$  are shown.

BOSS DR12						
	$(\xi_s)_{\text{mean}}$	$(\xi_s)_{\text{std}}$	$(\xi_s)_{-1\sigma}$	$(\xi_s)_{+1\sigma}$	$(\xi_s)_{>95\%}$	$(\xi_s)_{<95\%}$
DHOST ( $z_{\text{eff}} = 0.38$ )	5.232	3.495	-2.948	4.904	-0.744	-
DHOST ( $z_{\text{eff}} = 0.61$ )	8.791	6.841	-6.984	8.889	-2.653	-
DHOST ( $z_{\text{eff}} = 0.38, 0.61$ )	5.407	3.360	-2.988	4.664	-0.275	-
DHOST ( $z_{\text{eff}} = 0.38$ [rescaled])	5.307	3.519	-2.854	5.063	-0.740	-
DHOST ( $z_{\text{eff}} = 0.38$ [rescaled], 0.61)	5.378	3.438	-2.777	4.993	-0.504	-

**Table 22.** Same as Table 20, except the results for  $\xi_s$  that varies in DHOST theories are shown.

Using all the four galaxy samples, at the  $1\sigma$  level, we obtain

$$\begin{aligned}\gamma &= 0.485_{-0.708}^{+0.967} && \text{in Horndeski,} \\ \xi_f &= 0.791_{-0.691}^{+0.963} && \text{in DHOST,}\end{aligned}\quad (9.5)$$

and at the 95% confidence level, we have

$$\begin{aligned}-1.216 < \gamma < 2.175 && (95\% \text{CL}) && \text{in Horndeski,} \\ -0.907 < \xi_f < 2.447 && (95\% \text{CL}) && \text{in DHOST.}\end{aligned}\quad (9.6)$$

All results in Table 20 are consistent with GR within the  $1\sigma$  level.

Note that the  $\gamma$  constraints in Horndeski theories obtained here are not directly comparable to those obtained from existing studies by, e.g., Gil-Marín et al. (2017b). The reason is that we simultaneously vary the  $\xi_t$  parameter characterising the tidal term in the non-linear velocity field in Horndeski theories, while Gil-Marín et al. (2017b) use the bispectrum model assuming GR.

### 9.8 $\xi_t$ constraints from the BOSS DR12 galaxies in Horndeski and DHOST theories

Table 21 summarises the constraint results for the  $\xi_t$  parameter, defined as  $\xi_t = \ln_{\Omega_m}(E_t) = \ln_{\Omega_m}(\lambda_\theta/\kappa_\delta)$  (3.27), characterising the time evolution of the tidal term in the second-order velocity field. In GR,  $\xi_t = 15/1144$  (3.28), and if  $\xi_t$  deviates from the GR value, it is evidence for Horndeski or DHOST theories.

Using all the four galaxy samples, at the  $1\sigma$  level, we obtain

$$\begin{aligned}\xi_t &= 5.151_{-4.016}^{+6.112} && \text{in Horndeski,} \\ \xi_t &= 5.414_{-3.734}^{+6.007} && \text{in DHOST,}\end{aligned}\quad (9.7)$$

and at the 95% confidence level, we have

$$\begin{aligned}-2.098 < \xi_t < 2.175 && (95\% \text{CL}) && \text{in Horndeski,} \\ -1.655 < \xi_t < 2.447 && (95\% \text{CL}) && \text{in DHOST.}\end{aligned}\quad (9.8)$$

Eqs. (9.7) and (9.8) are one of the main results in this paper. Since the 95% upper bounds of  $\xi_t$  obtained in this analysis reach the upper bounds set by the flat prior distribution (Section 7.5), we present only the 95% lower bounds here.

All results in Table 21 are consistent with GR within the 95% level.

### 9.9 $\xi_s$ constraints from the BOSS DR12 galaxies in DHOST theories

Table 22 summarises the constraint results for  $\xi_s$ , defined as  $\xi_s = \ln_{\Omega_m}(E_s) = \ln_{\Omega_m}(\kappa_\theta/\kappa_\delta)$  (3.27), characterising the time evolution of the shift term in the second-order velocity field. In GR or Horndeski theories,  $\xi_s = 0$  (3.28) because  $\kappa_\delta = \kappa_\theta = 1$ . If  $\xi_s \neq 0$ , then it is the specific signal appearing in DHOST theories. Note that  $\xi_s \neq 0$  is a sufficient condition for detecting DHOST theories because there can be DHOST theories satisfying  $\kappa_\delta = \kappa_\theta$  (see Section 3.4).

Using all the four galaxy samples, at the  $1\sigma$  level, we obtain

$$\xi_s = 5.378_{-2.777}^{+4.993},\quad (9.9)$$

and at the 95% confidence level, we have

$$-0.504 < \xi_s < 2.175, \quad (9.10)$$

where we show only the lower limit of  $\xi_s$  for the same reason as for  $\xi_t$ . Eqs. (9.9) and (9.10) are the other main results of this paper in addition to Eqs. (9.7) and (9.8).

All results in Table 22 are consistent with GR within the 95% level.

For all the results obtained from Tables 20, 21, and 22, the standard deviations of  $\xi_{f,s,t}$  obtained by combining the samples  $z = 0.38$  and  $z = 0.61$  are smaller than those obtained at  $z = 0.38$  and  $z = 0.61$ , respectively. Therefore, future galaxy surveys with more redshift bins should improve our  $\xi_{f,s,t}$  constraints.

Similar to the  $f\sigma_8$  and  $\sigma_8$  results in GR, we confirm that the constraints of  $\xi_{f,s,t}$  are hardly affected by rescaling the covariance matrix by 15% – 25% at  $z = 0.38$ . This finding indicates that the results for  $\xi_{f,s,t}$  presented here will not change significantly even if future re-analysis from a better mock simulation gives acceptable  $p$ -values.

### 9.10 Joint analysis with the monopole 3PCF only

This subsection presents the results of a joint analysis of the monopole and quadrupole 2PCFs ( $\xi_0$  and  $\xi_2$ ) with only the monopole 3PCFs ( $\zeta_{000}$  and  $\zeta_{110}$ ) and compares them with our main results, revealing the importance of the information in the quadrupole 3PCFs ( $\zeta_{202}$  and  $\zeta_{112}$ ). In other words, we compare the results corresponding to Case 2 and Case 7 in Eq. 7.4. For simplicity, we focus here on the case where all four BOSS galaxy samples are used assuming DHOST theories and present a comparison of the results for  $\xi_f$ ,  $\xi_t$ , and  $\xi_s$ . For Case 2, as in Case 7, we determine the parameter priors according to the method described in Section 7.5, based on the results of the Fisher analysis.

The results of the joint analysis with the monopole 3PCFs are as follows:

$$\begin{aligned}(\xi_t)_{\text{mean}} \pm (\xi_t)_{\text{std}} &= 257.451 \pm 145.68, \\ (\xi_s)_{\text{mean}} \pm (\xi_s)_{\text{std}} &= 137.396 \pm 79.215.\end{aligned}\quad (9.11)$$

On the other hand, adding the quadrupole 3PCFs presents  $(\xi_t)_{\text{std}} = 4.211$  (Table 21) and  $(\xi_s)_{\text{std}} = 3.438$  (Table 22).

The addition of the quadrupole 3PCFs reduces the values of  $(\xi_t)_{\text{std}}$  and  $(\xi_s)_{\text{std}}$  by a factor of  $\sim 35$  and  $\sim 20$ , respectively. This improvement is consistent with the Fisher analysis result in Section 7 (see Eq. (7.6) and Table 5). Therefore, we conclude that the quadrupole component of the 3PCF should always be used to constrain  $\xi_t$  and  $\xi_s$ . Finally, the same should hold for testing other modified gravity theories through non-linear velocity fields.

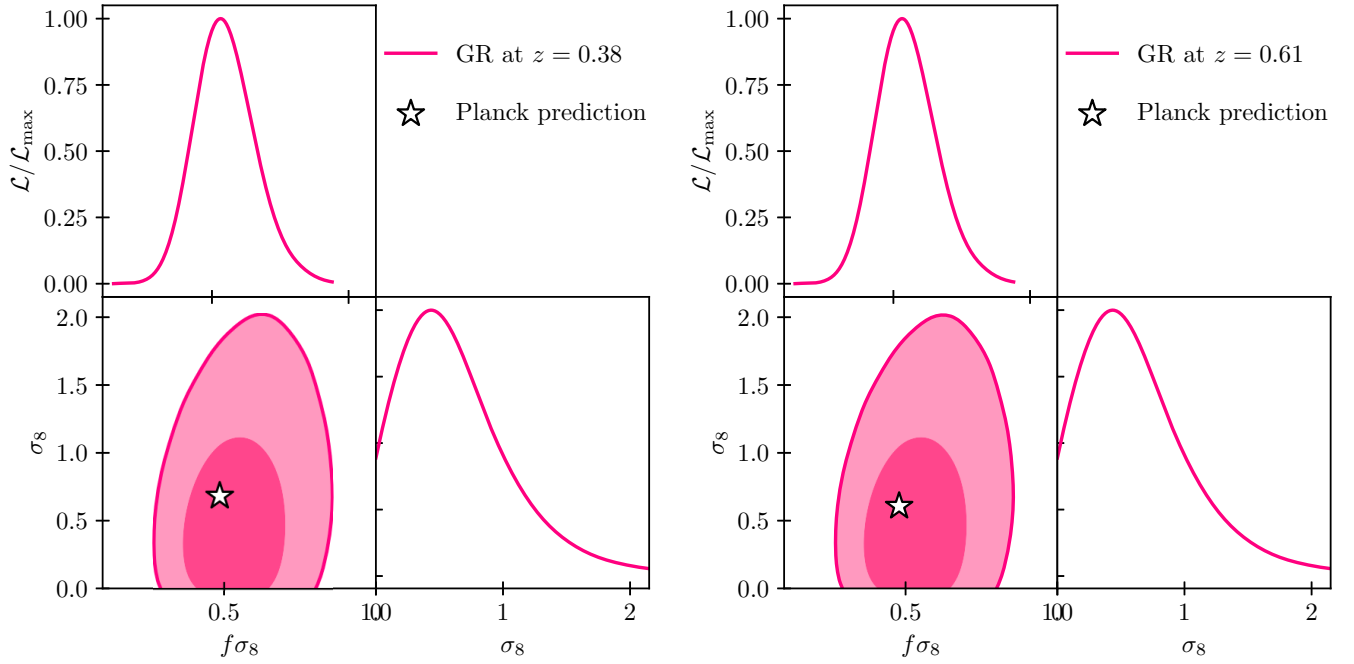
### 9.11 Consistency check with the Fisher analysis

This subsection discusses the consistency between the Fisher analysis results in Section 7 and our final results from MCMC in this section. For this purpose, We compare the standard deviation of a parameter  $\theta$  computed from the Fisher analysis,  $\sigma_{\text{fisher}}(\theta)$ , with that estimated from MCMC,  $(\theta)_{\text{std}}$ , where the parameters of interest are  $\theta = \xi_f, \xi_t, \xi_s$ , which are the main target of this paper.

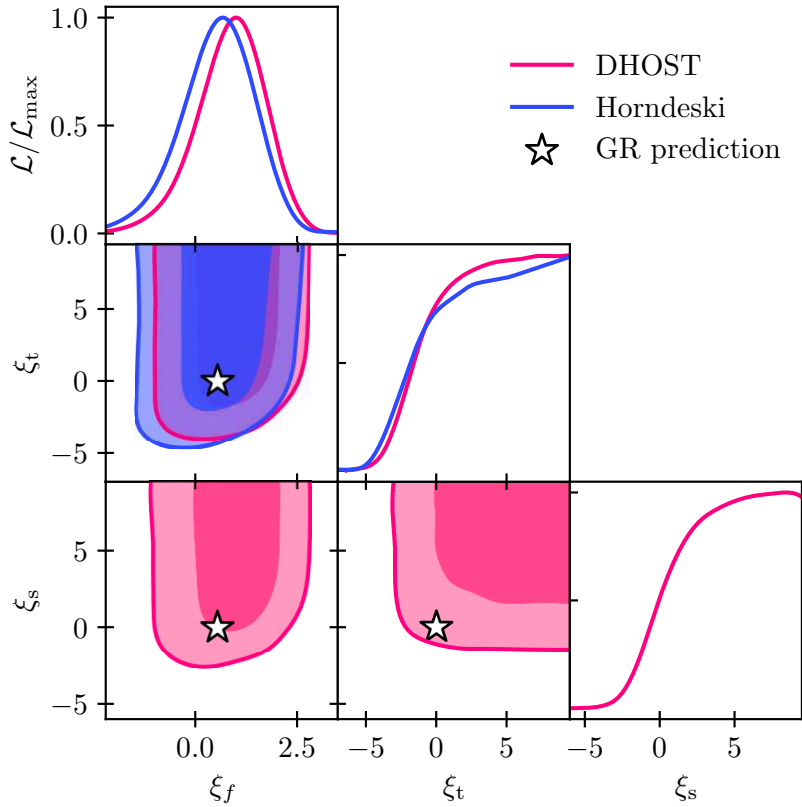
Table 23 summarises the cases for each redshift bin of  $z = 0.38$  and  $z = 0.61$  and for using both redshift bins, assuming DHOST theories. The values shown in this table are given from Tables 7, 20, 21, and 22. When combining the results for the different galaxy samples in Table 7, we use the standard error combination formula, assuming that each galaxy sample is independent.

Table 23 shows that the MCMC results satisfy  $(\theta)_{\text{std}} \gtrsim \sigma_{\text{fisher}}(\theta)$ , indicating that the MCMC results are consistent with the Fisher analysis results, as expected. This result reinforces the validity of our main results shown in Tables 20, 21, and 22.





**Figure 20.** Marginalized two- and one-dimensional posteriors of  $f\sigma_8$  and  $\sigma_8$  for BOSS DR12. The contours indicate 68.27% and 95.45% confidence levels. Asterisks indicate predictions by Planck. The left and right panels show the cases at  $z = 0.38$  and  $z = 0.61$ . The NGC and SGC samples are always combined to obtain this result. The rescaled 3PCF covariance matrix (Section 8.5) at  $z = 0.38$  is used.



**Figure 21.** Marginalized two- and one-dimensional posteriors of  $\xi_f$ ,  $\xi_t$ , and  $\xi_s$  for BOSS DR12. DHOST theories (red) vary these all three parameters, while Horndeski theories (blue) fix  $\xi_s$  to  $\xi_s = 0$ . The contours indicate 68.27% and 95.45% confidence levels. Asterisks indicate predictions by GR:  $\xi_f = 6/11$ ,  $\xi_t = 15/1144$ , and  $\xi_s = 0$ . The NGC and SGC samples at  $z = 0.38$  and  $0.61$  are combined to obtain this result. The rescaled 3PCF covariance matrix (Section 8.5) at  $z = 0.38$  is used.

DHOST		
	$(\xi_f)_{\text{std}}$	$\sigma_{\text{fisher}}(\xi_f)$
$z_{\text{eff}} = 0.38$	1.131	0.967
$z_{\text{eff}} = 0.61$	1.722	1.782
$z_{\text{eff}} = 0.38, 0.61$	0.830	0.850
	$(\xi_t)_{\text{std}}$	$\sigma_{\text{fisher}}(\xi_t)$
$z_{\text{eff}} = 0.38$	4.732	3.577
$z_{\text{eff}} = 0.61$	7.387	6.834
$z_{\text{eff}} = 0.38, 0.61$	4.211	3.169
	$(\xi_s)_{\text{std}}$	$\sigma_{\text{fisher}}(\xi_s)$
$z_{\text{eff}} = 0.38$	3.519	3.147
$z_{\text{eff}} = 0.61$	6.841	5.906
$z_{\text{eff}} = 0.38, 0.61$	3.438	2.778

**Table 23.** Comparison of the standard deviations,  $\sigma_{\text{fisher}}(\theta)$  and  $(\theta)_{\text{std}}$ , obtained from the Fisher analysis and MCMC for  $\theta = \xi_f, \xi_t, \xi_s$ . The results are shown for each redshift of  $z = 0.38$  and  $z = 0.61$  and the combined case of the two redshifts. In all cases shown here, the NGC and SGC samples are used; the MCMC results at  $z = 0.38$  use the rescaled covariance matrix (Section 8.5). All the values summarised here are those already given in Tables 7, 20, 21, and 22. When combining the results for the different galaxy samples in Table 7, we use the standard error composition formula, assuming that each galaxy sample is independent.

## 9.12 Comments on bias effects on shift terms

DHOST theories change the shift term of the non-linear density fluctuation from GR, which may introduce a new bias effect in the shift term, i.e., the shift bias parameter. Since  $E_{f,s,t}$  are the parameters that cancel the  $\sigma_8$ -dependence using the coefficients of the shift term of the density fluctuation, when the shift bias appears,  $E_{f,s,t}$  will also be contaminated by the bias effect. Furthermore, the shift bias may induce bias effects in linear and non-linear velocity fields. In such cases, we cannot use the parameterisation  $E_{f,s,t} = \Omega_m^{\xi_{f,s,t}}$  adopted in this paper to characterise the time dependence of  $E_{f,s,t}$  because the time dependence of the bias parameter is uncertain.

If we assume the presence of the shift bias effect, we propose simultaneously constraining all the six parameters  $(F_g\sigma_8)$ ,  $(F_s\sigma_8)$ ,  $(F_t\sigma_8)$ ,  $(G_g\sigma_8)$ ,  $(G_s\sigma_8)$  and  $(G_t\sigma_8)$  (3.15) that characterise the growth, shift, and tidal terms in the density and velocity fields in each galaxy sample as a more general test of modified gravity theories. In such an analysis, we should remove the relation  $G_g = G_s - (2/3)G_t$  imposed in DHOST theories. In particular, the  $E_s$  parameter, which represents the ratio of the coefficients of the shift terms of the non-linear density and velocity fields:  $E_s = (G_s\sigma_8)/(F_s\sigma_8)$ , is always  $E_s = 1$  in GR and Horndeski theories. Therefore, testing whether  $E_s = 1$  in each galaxy sample verifies the theory of varying the shift term, such as DHOST-like theories. In other words, it should provide a means to test the LSS consistency relation, which DHOST-like theories violate (Section 1), using the galaxy 3PCF (or bispectrum).

## 10 CONCLUSIONS

This paper presents a joint analysis of the anisotropic two-point and three-point correlation functions measured from the publicly available BOSS DR12 galaxy data to test cosmological modified gravity theories. This paper has two important implications. First, it is the first work to extract cosmological information from actual

galaxy data using the anisotropic component of the galaxy three-point correlation function induced by the RSD effect. Second, this analysis is the first attempt to constrain the non-linear effects of modified gravity theories from the galaxy three-point statistics.

We consider DHOST theories and their subclass, Horndeski theories, which are the candidates for modified gravity theories (see Section 2.1). They are quite general theoretical frameworks of scalar-tensor theories. Since the time evolution equation of the linear density fluctuations in these theories is scale-independent (2.6), the difference with GR appears only in the linear growth rate  $f$  in the linear theory (Hirano et al. 2019a). On the other hand, the non-linear gravitational effect causes a difference in the scale-dependence of the density fluctuation, which allows us to examine the deviation from GR more clearly. Specifically, Horndeski theories change the tidal term of the second-order density fluctuation from GR, while DHOST theories change both the shift and tidal terms (2.10 and 3.16) (Hirano et al. 2018). However, since non-linear bias parameters contaminate the density fluctuations, Yamauchi & Sugiyama (2022) have pointed out that one should investigate supposedly unbiased non-linear velocity fields induced by the RSD effect (see Section 3.4 for a review). Specifically, they have suggested that one should constrain the parameters  $\xi_t$  and  $\xi_s$ , which characterise the time evolution of the tidal and shift terms of the second-order velocity field:  $\xi_t = 15/1144$  in GR and  $\xi_s = 0$  in GR and Horndeski theories. Therefore, if  $\xi_s \neq 0$ , then it is the signal specific to DHOST theories; they have also pointed out that in DHOST theories, the parameter  $\gamma = \ln_{\Omega_m}(f)$ , which characterises the time dependence of the linear growth rate  $f$ , is extended to  $\xi_f = \ln_{\Omega_m}(f/\kappa)$  with  $\kappa$  being the time-dependent function appearing in the shift term of the density fluctuation. To this end, we test DHOST and Horndeski theories by constraining these parameters  $\xi_f$ ,  $\xi_t$ , and  $\xi_s$  using the joint analysis method of the anisotropic 2PCF and 3PCF, established by Sugiyama et al. (2021).

The following is a summary of the details of the analysis methodology and the findings obtained.

(i) Following Sugiyama et al. (2019), we apply the TripoSH decomposition method to the 3PCF to extract information about the anisotropic, i.e., *quadrupole*, component of the 3PCF (see Sections 3.1 and 4.2). To simplify the data analysis, we then use only two monopole components ( $\zeta_{000}$  and  $\zeta_{110}$ ) and two quadrupole components ( $\zeta_{202}$  and  $\zeta_{112}$ ) from the decomposed 3PCF. For the 2PCF, we adopt the commonly used Legendre decomposition method and use the monopole and quadrupole components: i.e.,  $\xi_0$  and  $\xi_2$ . It is worth noting that  $\zeta_{202}$  includes only the  $M = 0$  mode that appears in Scoccimarro et al. (1999)'s decomposition formalism, while  $\zeta_{112}$  includes  $M \neq 0$  modes in addition to the  $M = 0$  mode. Furthermore, the TripoSH-decomposed 3PCF allows a quantitative evaluation and detailed study of the survey window effect present in the measured 3PCFs (see Section 4.3). Thus, this work is the first to extract information on the  $M \neq 0$  modes from actual galaxy data, taking into account the window effect.

(ii) We only use data at large scales of  $80 h^{-1} \text{Mpc} \leq r \leq 150 h^{-1} \text{Mpc}$ , where higher-order non-linear corrections, called loop corrections, are not expected to contribute much to the 2PCF and 3PCF. In order to test modified gravity theories consistently using smaller scales, it is necessary to construct a model that includes the non-linear effects of modified gravity theories so that they are also included in the loop corrections. To our knowledge, only one such analysis has been performed so far for the case of the power spectrum in  $f(R)$  gravity (Song et al. 2015a). However, it is known

that various uncertainties arise in the non-linear power spectrum in DHOST theories, such as IR cancellation breaking (Crisostomi et al. 2020; Lewandowski 2020) and UV divergence (Hirano et al. 2020). These theoretical uncertainties should also appear in the bispectrum. Therefore, focusing only on large scales is necessary to remove the theoretical uncertainties and safely constrain the non-linear effects of modified gravity theories. Our analysis is thus the second example of a consistent analysis incorporating the non-linear effects of modified gravity from spectroscopic galaxy surveys, and the first to use the galaxy three-point statistic.

(iii) As a theoretical model for the 3PCF, we use the IR-resummed model (3.12) proposed by Sugiyama et al. (2021) (see Section 3.2). This model can describe the BAO damping effect while keeping the shape of the 3PCF in the tree-level solution. For this model, we have investigated how the three decomposed non-linear effects, i.e., the growth, shift, and tidal terms, affect the 3PCF multipoles (see Figures 1 and 2 in Section 3.3). For example, in the quadrupole components ( $\zeta_{202}$  and  $\zeta_{112}$ ), the dominant term is the product of the linear density fluctuation and the linear velocity field that appears during the coordinate transformation from real space to redshift space; otherwise, the non-linear effects of the density and velocity fields contribute to the quadrupole component to the same extent. Figures 12–19 in Section 9.1 show the  $\zeta_{000}$ ,  $\zeta_{110}$ ,  $\zeta_{202}$ , and  $\zeta_{112}$  measured from the four BOSS galaxy samples and the corresponding theoretical models calculated using the best-fit parameters.

(iv) We have used the 2048 publicly available Patchy mocks to compute the covariance matrices of the 2PCF and 3PCF in Section 5. In our analysis, we ensure that the number of data bins in the 2PCF and 3PCF is sufficiently smaller than the number of the 2048 mocks. In particular, the parameter  $M_2$  (5.5), which represents the impact of a finite number of mocks on the final parameter error, is at most  $M_2 \sim 1.1$  (see Section 6.4).

(v) To understand the nature of the covariance matrix, we have calculated the cumulative S/N of the 2PCF and the 3PCF in Section 5.4. The results show that the cumulative S/N of the 3PCF has different characteristics from that of the 2PCF. In the case of the 2PCF, the galaxy sample at  $z = 0.61$  with a larger volume has a smaller covariance matrix than the sample at  $z = 0.38$ , resulting in a larger S/N at  $z = 0.61$ . On the other hand, for the 3PCF, the S/N at  $z = 0.38$  is comparable to the S/N at  $z = 0.61$ . Therefore, the difference in survey volume cannot explain the relationship between the S/N of the 3PCF at  $z = 0.38$  and  $0.61$ . A possible explanation for this 3PCF S/N behaviour is that the covariance matrix of the 3PCF depends strongly on the number density of the galaxies (see Sugiyama et al. 2020): the BOSS sample at  $z = 0.38$  has a higher number density than the sample at  $z = 0.61$ , even with a smaller survey volume (Table 1). We interpret this higher number density as why the S/N at  $z = 0.38$  is as high as that at  $z = 0.61$ .

(vi) We have investigated the extent to which higher-order terms in the TripoSH decomposition of the 3PCF contain cosmological information by Fisher analysis (see Section 7.2). The results show that  $\zeta_{202}$  is the main cosmological information in the quadrupole 3PCF, while other information is contained in the higher-order term  $\zeta_{112}$  in addition to  $\zeta_{202}$ . Since  $\zeta_{112}$  contains the  $M \neq 0$  modes in Scoccimarro et al. (1999)’s decomposition formalism but not in  $\zeta_{202}$ , this result indicates the importance of the  $M \neq 0$  modes.

(vii) In Section 8, we have reported that at large scales ( $\geq 80 h^{-1} \text{Mpc}$ ), there can be statistically significant differences be-

tween the 3PCFs measured from the BOSS galaxies and the corresponding theoretical models, regardless of whether we assume GR, Horndeski or DHOST theories. For example, the  $p$ -value obtained from the SGC sample at  $z = 0.38$  is less than 0.01, and the  $p$ -value obtained from the combined sample of the four BOSS samples is 0.001 (see Section 8.1). This result means that the discrepancies between the galaxy data and the theoretical models cannot be explained within the framework of scalar-tensor theory, even if they are due to unknown physical effects. Other results show that the discrepancy is mainly due to the monopole component of the 3PCF rather than the quadrupole component (see Section 8.2) and that this discrepancy cannot be explained even if the prior distribution of the parameters is changed (see Section 8.3). Finally, we have repeated the same analysis for the 100 Patchy mocks as for the BOSS sample in Section 8.4. The results show a statistically significant difference of more than  $5\sigma$  between the  $p$ -values of the Patchy mocks and the BOSS galaxies. Therefore, the statistical variability of the Patchy mock galaxies cannot explain the low  $p$ -values ( $p \sim 0.001$ ) obtained from the BOSS galaxies.

(viii) In this paper, we assume that the discrepancy between the BOSS galaxy sample and the theoretical model is due to an inappropriate 3PCF covariance matrix computed from the Patchy mocks. We then take a conservative approach by artificially rescaling the 3PCF covariance matrix at  $z = 0.38$  by 15% for NGC and 25% for SGC, resulting in acceptable  $p$ -values (see Section 8.5). To confirm the validity of this method, we have presented in Section 9 the results of constraining the parameters of interest with and without rescaling the covariance matrix and have confirmed that there is no significant difference in the final results obtained in these two cases. We interpret this result as being due to a more significant degeneracy effect between the parameters than the  $\sim 20\%$  difference in the 3PCF covariance matrix. Therefore, we do not expect that calculating the covariance matrix from simulation data that better reproduces the distribution of the BOSS galaxies will significantly change the results of the present paper.

(ix) We have constrained  $f\sigma_8$  from the BOSS galaxies assuming GR in Section 9.3. There, we have shown that adding isotropic and anisotropic 3PCF components ( $\zeta_{000}$ ,  $\zeta_{110}$ ,  $\zeta_{202}$ , and  $\zeta_{112}$ ) does little to improve the results compared to the 2PCF-only analysis. Nevertheless, the analysis using the Patchy mocks shows that the 3PCF information does help to reduce the bias of the mean value of  $f\sigma_8$  (see Section 9.2). Finally, we obtain  $f\sigma_8 = 0.549_{-0.122}^{+0.097}$  at  $z = 0.38$  and  $f\sigma_8 = 0.394_{-0.099}^{+0.088}$  at  $z = 0.61$  in the joint analysis of the anisotropic 2PCF and 3PCF assuming GR (9.2). These  $f\sigma_8$  results are not as competitive as existing constraints (e.g., Alam et al. 2017; Ivanov et al. 2020; Lange et al. 2022; Kobayashi et al. 2022) because we only use large-scale information ( $r \geq 80 h^{-1} \text{Mpc}$ ).

One may think that adding the 3PCF information does not improve the  $f\sigma_8$  results due to the focus on large scales only ( $r \geq 80 h^{-1} \text{Mpc}$ ). To test this concern, we have performed a Fisher analysis that includes small scales ( $30 h^{-1} \text{Mpc} \leq r \leq 150 h^{-1} \text{Mpc}$ ) and find that even if we extend the used scales to  $30 h^{-1} \text{Mpc}$ , there is no improvement in the  $f\sigma_8$  results (see Section 7.4). However, note that we use the IR-resummed tree-level model of the 3PCF in this Fisher analysis. Therefore, if we use a theoretical model with various loop corrections applicable down to small scales, parameter degeneracy may break, and it may still be possible to obtain improved  $f\sigma_8$  constraints through a joint analysis of the 2PCF and 3PCF.

(x) We have constrained  $\sigma_8$  from the BOSS galaxies assuming

GR in Section 9.6. Thus, while the 3PCF information does not improve the  $f\sigma_8$  constraints, it helps to break the degeneracy between parameters by providing information on  $\sigma_8$ : e.g., it allows us to constrain  $f$ . We have obtained  $\sigma_8 = 0.692^{+0.209}_{-0.591}$  at  $z = 0.38$  and  $\sigma_8 = 0.568^{+0.144}_{-0.547}$  at  $z = 0.61$  at the  $1\sigma$  level. These results are consistent with  $\sigma_8 = 0.681, 0.606$  at  $z = 0.38, 0.61$  calculated from the cosmological parameters in a flat  $\Lambda$ CDM model given by Planck 2018. The ratio of the standard deviation to the mean for  $\sigma_8$  is  $(\sigma_8)_{\text{std}}/(\sigma_8)_{\text{mean}} = 0.66$  at  $z = 0.38$  and  $0.71$  at  $z = 0.61$ , indicating that the galaxy sample at  $z = 0.38$  provides a better constraint on  $\sigma_8$ . This result can be attributed to the higher number density of the sample at  $z = 0.38$  compared to that at  $z = 0.61$ , similar to the argument of the cumulative S/N in Section 5.4.

(xi) Our main results, the constraints on the  $\xi_f, \xi_t$ , and  $\xi_s$  parameters in DHOST theories, are summarised in Sections 9.7, 9.8, and 9.9. There, we obtain  $\xi_f = 0.791^{+0.963}_{-0.691}$  (9.5),  $\xi_t = 5.414^{+6.007}_{-3.734}$  (9.7), and  $\xi_s = 5.378^{+4.993}_{-2.777}$  (9.9) at the  $1\sigma$  level; we also have  $-0.907 < \xi_f < 2.447$  (9.6),  $-1.655 < \xi_t$  (9.8), and  $-0.504 < \xi_s$  (9.10) at the 95% confidence level. Since we cannot detect the signal of the tidal and shift terms in the second-order velocity field in the present analysis, we can only present the 95% lower bounds of the  $\xi_t$  and  $\xi_s$  parameters. These results are consistent with the GR predictions  $\xi_f = \gamma = 6/11$ ,  $\xi_t = 15/1144$ , and  $\xi_s = 0$  (see Figure 21). Moreover, we have checked the consistency of the estimated results from the BOSS galaxy sample with the Fisher analysis for the constraints on the  $\xi_{f,t,s}$  parameters in DHOST theories in Section 9.11.

In Horndeski theories, we obtain  $\xi_f = \gamma = 0.485^{+0.967}_{-0.708}$  and  $\xi_t = 5.151^{+6.112}_{-4.016}$  at the  $1\sigma$  level, and  $-1.216 < \gamma < 2.175$  and  $-2.098 < \xi_t$  at the 95% confidence level. The  $\gamma$  constraint in Horndeski theories obtained here is not directly comparable to those obtained from existing studies by, e.g., Gil-Marín et al. (2017b) because we simultaneously vary the  $\xi_t$  parameter in Horndeski theories.

(xii) We have shown that the anisotropic component of the 3PCF contributes significantly to the constraints on the shape of the non-linear velocity field in Section 9.10. In particular, the constraints on the parameters  $\xi_t$  and  $\xi_s$  are  $\sim 35$  and  $\sim 20$  times better when the anisotropic component is added than when only the isotropic component is considered. This result strongly supports the main claim of this paper that the anisotropic three-point statistics should be considered to test the non-linearity of modified gravity theories.

Below is a summary of some of the concerns and future enhancements to the results of this paper.

(i) In order to encourage the future development of the anisotropic 3PCF analysis, we comment on the situation beyond the assumptions used to derive the non-linear effects of DHOST theories that we focus on in this paper (see Section 2.2). First, our analysis can be applied to other modified gravity theories, such as  $f(R)$  gravity models and brane-world models. In addition, it should also be possible to constrain effects such as the CDM-baryon relative velocity and massive neutrinos, which give rise to characteristic non-linear behaviour. The calculations of DHOST theories in this paper assume minimal coupling between the metric field and the scalar field, Gaussianity of the initial conditions, and the quasi-static limit, but we need additional correction terms if these assumptions are removed. In addition, since DHOST theories modify the shift term from GR, we cannot exclude the possibility of shift bias, which we do not consider in a  $\Lambda$ CDM model. In the presence of shift bias, we cannot use the  $\xi_s$  and  $\xi_t$  parameters to constrain DHOST theories, but we expect the

$E_s$  and  $E_t$  parameters constrained at each redshift to remain valid (Section 9.12).

(ii) We also comment on some improvements in our analysis of the anisotropic 3PCF (see Section 3.5). First, as more mock catalogues are created in the future, increasing the number of multipoles in the 3PCF to be considered should improve the results of this work (e.g., Byun & Krause 2022). Second, as shown in Figure 10, we can dramatically improve the current parameter constraints by using the theoretical model of the 3PCF, which is applicable to small scales (see Section 7.4). Third, although we have used the shape of the linear power spectrum calculated by an  $\Lambda$ CDM model in a high- $z$  region in this work, it needs to be calculated in the framework of DHOST theories in the future (e.g., Hiramatsu & Yamauchi 2020). Fourth, we have calculated the Gaussian function describing the damping effect of the BAO signal for a  $\Lambda$ CDM model, but we also need to constrain this function itself. Finally, we have neglected the Alcock-Paczyński (AP) effect in this work; the analysis method of the anisotropic 3PCF that includes the AP effect has been established by Sugiyama et al. (2021) using the Patchy mock and should be straightforward to apply to actual galaxy data. We hope that addressing these issues will further improve our results.

Finally, in Appendix A we provide the software package that can reproduce all the results obtained in this paper, HITOMI. The aim of HITOMI is to make available all the programs we have used to complete the anisotropic 3PCF analysis, from downloading the SDSS DR12 galaxy data, measuring the 2PCFs and 3PCFs, computing the theoretical models, calculating the covariance matrices, the window function corrections, MCMC analysis, and producing figures and tables. This makes it easier for any user to see how partial improvements to HITOMI, e.g. improved 3PCF model calculations, feed through to the final parameter constraints. Furthermore, by replacing the BOSS galaxy data used in HITOMI, our analysis can be easily applied to future galaxy surveys such as DESI (DESI Collaboration et al. 2016), Euclid (Laureijs et al. 2011), and PFS (Takada et al. 2014).

## ACKNOWLEDGEMENTS

NSS acknowledges financial support from JSPS KAKENHI Grant Number 19K14703. Numerical computations were carried out on Cray XC50 at Center for Computational Astrophysics, National Astronomical Observatory of Japan. The work of SH was supported by JSPS KAKENHI Grants No. JP21H01080. The work of TK was supported by JSPS KAKENHI Grant No. JP20K03936 and MEXT-JSPS Grant-in-Aid for Transformative Research Areas (A) ‘‘Extreme Universe’’, No. JP21H05182 and No. JP21H05189. The work of DY was supported in part by JSPS KAKENHI Grants No. 19H01891, No. 22K03627. SS acknowledges the support for this work from NSF-2219212. SS is supported in part by World Premier International Research Center Initiative (WPI Initiative), MEXT, Japan. H-JS is supported by the U.S. Department of Energy, Office of Science, Office of High Energy Physics under DE-SC0019091 and DE-SC0023241. This project has received funding from the European Research Council (ERC) under the European Union’s Horizon 2020 research and innovation program (grant agreement 853291). FB is a University Research Fellow.



## DATA AVAILABILITY

The data underlying this article are available at the SDSS data base (<https://www.sdss.org/dr12/>).

## REFERENCES

- Abbott B. P., et al., 2017a, *Phys. Rev. Lett.*, 119, 161101
- Abbott B. P., et al., 2017b, *Astrophys. J. Lett.*, 848, L13
- Agarwal N., Desjacques V., Jeong D., Schmidt F., 2021, *J. Cosmology Astropart. Phys.*, 2021, 021
- Aghanim N., et al., 2020, *Astron. Astrophys.*, 641, A6
- Alam S., et al., 2015, *Astrophys. J. Suppl.*, 219, 12
- Alam S., et al., 2017, *Mon. Not. Roy. Astron. Soc.*, 470, 2617
- Alam S., et al., 2021a, *Phys. Rev. D*, 103, 083533
- Alam S., et al., 2021b, *J. Cosmology Astropart. Phys.*, 2021, 050
- Albrecht A., Steinhardt P. J., 1982, *Phys. Rev. Lett.*, 48, 1220
- Alcock C., Paczyński B., 1979, *Nature*, 281, 358
- Alvarez M., et al., 2014, arXiv e-prints, p. arXiv:1412.4671
- Amendola L., Kunz M., Saltas I. D., Sawicki I., 2018, *Phys. Rev. Lett.*, 120, 131101
- Amendola L., Bettoni D., Pinho A. M., Casas S., 2020, *Universe*, 6, 20
- Anderson L., et al., 2014, *Mon. Not. Roy. Astron. Soc.*, 441, 24
- Arai S., Nishizawa A., 2018, *Phys. Rev. D*, 97, 104038
- Arai S., et al., 2022, arXiv e-prints, p. arXiv:2212.09094
- Audren B., Lesgourgues J., Benabed K., Prunet S., 2013, *JCAP*, 1302, 001
- Aviles A., Rodriguez-Meza M. A., De-Santiago J., Cervantes-Cota J. L., 2018, *JCAP*, 11, 013
- Babichev E., Deffayet C., 2013, *Class. Quant. Grav.*, 30, 184001
- Babichev E., Lehébel A., 2018, *JCAP*, 12, 027
- Babichev E., Koyama K., Langlois D., Saito R., Sakstein J., 2016, *Class. Quant. Grav.*, 33, 235014
- Baker T., Bellini E., Ferreira P. G., Lagos M., Noller J., Sawicki I., 2017, *Phys. Rev. Lett.*, 119, 251301
- Baker T., et al., 2021, *Rev. Mod. Phys.*, 93, 015003
- Baldauf T., Seljak U., Desjacques V., McDonald P., 2012, *Phys. Rev. D*, 86, 083540
- Baldauf T., Mirbabayi M., Simonović M., Zaldarriaga M., 2015a, *Phys. Rev. D*, 92, 043514
- Baldauf T., Mercolli L., Mirbabayi M., Pajer E., 2015b, *J. Cosmology Astropart. Phys.*, 2015, 007
- Barreira A., Li B., Baugh C., Pascoli S., 2014, *JCAP*, 08, 059
- Barreira A., Sánchez A. G., Schmidt F., 2016, *Phys. Rev. D*, 94, 084022
- Barriga J., Gaztañaga E., 2002, *MNRAS*, 333, 443
- Barriga J., Gaztañaga E., 2002, *Mon. Not. Roy. Astron. Soc.*, 333, 443
- Bartolo N., Bellini E., Bertacca D., Matarrese S., 2013, *JCAP*, 03, 034
- Baumgart D. J., Fry J. N., 1991, *ApJ*, 375, 25
- Bean A. J., Ellis R. S., Shanks T., Efstathiou G., Peterson B. A., 1983, *MNRAS*, 205, 605
- Bellini E., Zumalacarregui M., 2015, *Phys. Rev. D*, 92, 063522
- Bellini E., Jimenez R., Verde L., 2015, *JCAP*, 05, 057
- Bellini E., Cuesta A. J., Jimenez R., Verde L., 2016, *JCAP*, 02, 053
- Beltran Jimenez J., Piazza F., Velten H., 2016, *Phys. Rev. Lett.*, 116, 061101
- Ben Achour J., Crisostomi M., Koyama K., Langlois D., Noui K., Tasinato G., 2016a, *JHEP*, 12, 100
- Ben Achour J., Langlois D., Noui K., 2016b, *Phys. Rev. D*, 93, 124005
- Bereziani L., Khoury J., 2014, *JCAP*, 09, 018
- Bernardeau F., Brax P., 2011, *J. Cosmology Astropart. Phys.*, 2011, 019
- Bernardeau F., Colombi S., Gaztanaga E., Scoccimarro R., 2002, *Phys. Rept.*, 367, 1
- Bernardeau F., Van de Rijt N., Vernizzi F., 2012, *Phys. Rev. D*, 85, 063509
- Bernardeau F., Van de Rijt N., Vernizzi F., 2013, *Phys. Rev. D*, 87, 043530
- Beutler F., et al., 2014, *MNRAS*, 443, 1065
- Beutler F., Blake C., Koda J., Marin F., Seo H.-J., Cuesta A. J., Schneider D. P., 2016, *Mon. Not. Roy. Astron. Soc.*, 455, 3230
- Beutler F., et al., 2017, *Mon. Not. Roy. Astron. Soc.*, 466, 2242
- Bharadwaj S., Mazumdar A., Sarkar D., 2020, *MNRAS*, 493, 594
- Bianchi D., Gil-Marín H., Ruggeri R., Percival W. J., 2015, *MNRAS*, 453, L11
- Blas D., Lesgourgues J., Tram T., 2011, *JCAP*, 07, 034
- Blas D., Garny M., Konstandin T., 2013, *JCAP*, 09, 024
- Blas D., Garny M., Ivanov M. M., Sibiryakov S., 2016a, *JCAP*, 07, 028
- Blas D., Garny M., Ivanov M. M., Sibiryakov S., 2016b, *JCAP*, 07, 052
- Bolton A. S., et al., 2012, *Astron. J.*, 144, 144
- Borisov A., Jain B., 2009, *Phys. Rev. D*, 79, 103506
- Bose B., Koyama K., 2016, *JCAP*, 08, 032
- Bose B., Taruya A., 2018, *JCAP*, 10, 019
- Bose B., Koyama K., Hellwing W. A., Zhao G.-B., Winther H. A., 2017, *Phys. Rev. D*, 96, 023519
- Bose B., Koyama K., Lewandowski M., Vernizzi F., Winther H. A., 2018, *JCAP*, 04, 063
- Bose B., Byun J., Lacasa F., Moradinezhad Dizgah A., Lombriser L., 2020a, *JCAP*, 02, 025
- Bose B., Cataneo M., Tröster T., Xia Q., Heymans C., Lombriser L., 2020b, *Mon. Not. Roy. Astron. Soc.*, 498, 4650
- Bouchet F. R., Juszkiewicz R., Colombi S., Pellat R., 1992, *Astrophys. J. Lett.*, 394, L5
- Bouchet F. R., Colombi S., Hivon E., Juszkiewicz R., 1995, *A&A*, 296, 575
- Brinckmann T., Lesgourgues J., 2019, *Physics of the Dark Universe*, 24, 100260
- Burrage C., Dombrowski J., Saadeh D., 2019, *JCAP*, 10, 023
- Byun J., Krause E., 2022, *MNRAS*,
- Cabass G., Ivanov M. M., Philcox O. H. E., Simonović M., Zaldarriaga M., 2022a, *Phys. Rev. D*, 106, 043506
- Cabass G., Ivanov M. M., Philcox O. H. E., Simonović M., Zaldarriaga M., 2022b, *Phys. Rev. Lett.*, 129, 021301
- Calles J., Castiblanco L., Noreña J., Stahl C., 2020, *JCAP*, 07, 033
- Capozziello S., Francaviglia M., 2008, *Gen. Rel. Grav.*, 40, 357
- Carlstrom J., et al., 2019, in Bulletin of the American Astronomical Society, p. 209 (arXiv:1908.01062)
- Castiblanco L., Gannouji R., Noreña J., Stahl C., 2019, *JCAP*, 07, 030
- Cataneo M., Rapetti D., 2018, *Int. J. Mod. Phys. D*, 27, 1848006
- Cataneo M., Lombriser L., Heymans C., Mead A., Barreira A., Bose S., Li B., 2019, *Mon. Not. Roy. Astron. Soc.*, 488, 2121
- Chiang C.-T., Wagner C., Sánchez A. G., Schmidt F., Komatsu E., 2015, *J. Cosmology Astropart. Phys.*, 2015, 028
- Chiba T., Chibana F., Yamaguchi M., 2020, *JCAP*, 06, 003
- Chibana F., Kimura R., Yamaguchi M., Yamauchi D., Yokoyama S., 2019, *JCAP*, 10, 049
- Child H. L., Slepian Z., Takada M., 2018, arXiv e-prints, p. arXiv:1811.12396
- Clarkson C., de Weerd E. M., Jolicoeur S., Maartens R., Umeh O., 2019, *MNRAS*, 486, L101
- Coulton W. R., et al., 2023, *ApJ*, 943, 178
- Creminelli P., Vernizzi F., 2017, *Phys. Rev. Lett.*, 119, 251302
- Creminelli P., Zaldarriaga M., 2004, *JCAP*, 10, 006
- Creminelli P., Noreña J., Simonović M., Vernizzi F., 2013, *JCAP*, 12, 025
- Creminelli P., Gleyzes J., Simonović M., Vernizzi F., 2014a, *JCAP*, 02, 051
- Creminelli P., Gleyzes J., Hui L., Simonović M., Vernizzi F., 2014b, *J. Cosmology Astropart. Phys.*, 2014, 009
- Creminelli P., Lewandowski M., Tambalo G., Vernizzi F., 2018, *JCAP*, 12, 025
- Creminelli P., Tambalo G., Vernizzi F., Yingcharoenrat V., 2019, *JCAP*, 10, 072
- Crisostomi M., Koyama K., 2018, *Phys. Rev. D*, 97, 021301
- Crisostomi M., Koyama K., Tasinato G., 2016, *JCAP*, 04, 044
- Crisostomi M., Lewandowski M., Vernizzi F., 2019, *Phys. Rev. D*, 100, 024025
- Crisostomi M., Lewandowski M., Vernizzi F., 2020, *Phys. Rev. D*, 101, 123501
- Crocce M., Scoccimarro R., 2008, *Phys. Rev. D*, 77, 023533
- Cusin G., Lewandowski M., Vernizzi F., 2018a, *JCAP*, 04, 005
- Cusin G., Lewandowski M., Vernizzi F., 2018b, *JCAP*, 04, 061
- D'Amico G., Lewandowski M., Senatore L., Zhang P., 2022a, arXiv e-prints, p. arXiv:2201.11518
- D'Amico G., Donath Y., Lewandowski M., Senatore L., Zhang P., 2022b, arXiv e-prints, p. arXiv:2206.08327



- DESI Collaboration et al., 2016, *arXiv e-prints*, p. [arXiv:1611.00036](https://arxiv.org/abs/1611.00036)
- Dalal N., Pen U.-L., Seljak U., 2010, *JCAP*, 11, 007
- Dawson K. S., et al., 2013, *Astron. J.*, 145, 10
- Dawson K. S., et al., 2016, *Astron. J.*, 151, 44
- Deffayet C., Gao X., Steer D. A., Zahariade G., 2011, *Phys. Rev. D*, 84, 064039
- Desjacques V., Seljak U., 2010, *Classical and Quantum Gravity*, 27, 124011
- Desjacques V., Jeong D., Schmidt F., 2018a, *JCAP*, 12, 035
- Desjacques V., Jeong D., Schmidt F., 2018b, *Phys. Rept.*, 733, 1
- Desjacques V., Jeong D., Schmidt F., 2018c, *J. Cosmology Astropart. Phys.*, 2018, 035
- Dima A., Vernizzi F., 2018, *Phys. Rev. D*, 97, 101302
- Dinda B. R., 2018, *JCAP*, 06, 017
- Dodelson S., Schneider M. D., 2013, *Phys. Rev.*, D88, 063537
- Doi M., et al., 2010, *Astron. J.*, 139, 1628
- Doré O., et al., 2014, *arXiv e-prints*, p. [arXiv:1412.4872](https://arxiv.org/abs/1412.4872)
- Dvali G. R., Gabadadze G., Porrati M., 2000, *Phys. Lett. B*, 485, 208
- Efstathiou G., Jędrzejewski R. I., 1994, *Adv. Space Res.*, 3, 379
- Eggemeier A., Scoccimarro R., Smith R. E., 2019, *Phys. Rev. D*, 99, 123514
- Eggemeier A., Scoccimarro R., Smith R. E., Crocce M., Pezzotta A., Sánchez A. G., 2021, *Phys. Rev. D*, 103, 123550
- Eisenstein D. J., Hu W., 1998, *Astrophys. J.*, 496, 605
- Eisenstein D. J., Seo H.-j., White M. J., 2007a, *Astrophys. J.*, 664, 660
- Eisenstein D. J., Seo H.-j., Sirko E., Spergel D., 2007b, *Astrophys. J.*, 664, 675
- Eisenstein D. J., et al., 2011, *Astron. J.*, 142, 72
- Esposito A., Hui L., Scoccimarro R., 2019, *Phys. Rev. D*, 100, 043536
- Ezquiaga J. M., Zumalacárregui M., 2017, *Phys. Rev. Lett.*, 119, 251304
- Feldman H. A., Kaiser N., Peacock J. A., 1994, *ApJ*, 426, 23
- Feldman H. A., Frieman J. A., Fry J. N., Scoccimarro R., 2001, *Phys. Rev. Lett.*, 86, 1434
- Ferreira P. G., 2019, *Ann. Rev. Astron. Astrophys.*, 57, 335
- Fosalba P., Gaztanaga E., 1998, *Mon. Not. Roy. Astron. Soc.*, 301, 503
- Fosalba P., Pan J., Szapudi I., 2005, *ApJ*, 632, 29
- Frieman J. A., Gaztañaga E., 1999, *ApJ*, 521, L83
- Frieman J. A., Gaztanaga E., 1994, *ApJ*, 425, 392
- Frieger M., Johnson S. G., 2005, *Proceedings of the IEEE*, 93, 216
- Frusciante N., Perenon L., 2020, *Phys. Rept.*, 857, 1
- Fry J. N., 1984, *ApJ*, 279, 499
- Fry J. N., 1994, *Phys. Rev. Lett.*, 73, 215
- Fry J. N., Peebles P. J. E., 1980, *ApJ*, 238, 785
- Fry J. N., Scherrer R. J., 1994, *Astrophys. J.*, 429, 36
- Fry J. N., Seldner M., 1982, *ApJ*, 259, 474
- Fujita T., Vlah Z., 2020, *J. Cosmology Astropart. Phys.*, 2020, 059
- Fukugita M., Ichikawa T., Gunn J. E., Doi M., Shimasaku K., Schneider D. P., 1996, *Astron. J.*, 111, 1748
- Gagrani P., Samushia L., 2017, *MNRAS*, 467, 928
- Ganz A., Noui K., 2020, *arXiv e-prints*, p. [arXiv:2007.01063](https://arxiv.org/abs/2007.01063)
- Gaztañaga E., Scoccimarro R., 2005, *MNRAS*, 361, 824
- Gaztañaga E., Norberg P., Baugh C. M., Croton D. J., 2005, *MNRAS*, 364, 620
- Gaztañaga E., Cabré A., Castander F., Crocce M., Fosalba P., 2009, *MNRAS*, 399, 801
- Gelman A., Rubin D. B., 1992, *Statistical Science*, 7, 457
- Gil-Marín H., Schmidt F., Hu W., Jimenez R., Verde L., 2011, *J. Cosmology Astropart. Phys.*, 2011, 019
- Gil-Marín H., Wagner C., Fragkoudi F., Jimenez R., Verde L., 2012, *J. Cosmology Astropart. Phys.*, 2012, 047
- Gil-Marín H., Wagner C., Noreña J., Verde L., Percival W., 2014, *J. Cosmology Astropart. Phys.*, 2014, 029
- Gil-Marín H., Noreña J., Verde L., Percival W. J., Wagner C., Manera M., Schneider D. P., 2015a, *MNRAS*, 451, 539
- Gil-Marín H., et al., 2015b, *MNRAS*, 452, 1914
- Gil-Marín H., Percival W. J., Verde L., Brownstein J. R., Chuang C.-H., Kitaura F.-S., Rodríguez-Torres S. A., Olmstead M. D., 2017a, *MNRAS*, 465, 1757
- Gil-Marín H., Percival W. J., Verde L., Brownstein J. R., Chuang C.-H., Kitaura F.-S., Rodríguez-Torres S. A., Olmstead M. D., 2017b, *Mon. Not. Roy. Astron. Soc.*, 465, 1757
- Gleyzes J., Langlois D., Piazza F., Vernizzi F., 2015a, *JCAP*, 02, 018
- Gleyzes J., Langlois D., Piazza F., Vernizzi F., 2015b, *Phys. Rev. Lett.*, 114, 211101
- Goldstein S., Esposito A., Philcox O. H. E., Hui L., Hill J. C., Scoccimarro R., Abitbol M. H., 2022, *Phys. Rev. D*, 106, 123525
- Goroff M. H., Grinstein B., Rey S. J., Wise M. B., 1986, *ApJ*, 311, 6
- Gott J. R. I., Gao B., Park C., 1991, *ApJ*, 383, 90
- Greig B., Komatsu E., Wyithe J. S. B., 2013, *MNRAS*, 431, 1777
- Groth E. J., Peebles P. J. E., 1977, *Astrophys. J.*, 217, 385
- Gualdi D., Verde L., 2020, *J. Cosmology Astropart. Phys.*, 2020, 041
- Gunn J. E., et al., 1998, *Astron. J.*, 116, 3040
- Gunn J. E., et al., 2006, *Astron. J.*, 131, 2332
- Guo H., Jing Y. P., 2009, *ApJ*, 698, 479
- Guo H., Li C., Jing Y. P., Börner G., 2014, *ApJ*, 780, 139
- Guth A. H., 1981, *Phys. Rev.*, D23, 347
- Hahn T., 2005, *Computer Physics Communications*, 168, 78
- Hale-Sutton D., Fong R., Metcalfe N., Shanks T., 1989, *MNRAS*, 237, 569
- Hamilton A. J. S., 1997, in *Ringberg Workshop on Large Scale Structure Ringberg, Germany, September 23-28, 1996.* ([arXiv:astro-ph/9708102](https://arxiv.org/abs/astro-ph/9708102)), doi:10.1007/978-94-011-4960-0\_17
- Hamilton A. J. S., 2000, *MNRAS*, 312, 257
- Hand N., Li Y., Slepian Z., Seljak U., 2017, *J. Cosmology Astropart. Phys.*, 2017, 002
- Hartlap J., Simon P., Schneider P., 2007, *A&A*, 464, 399
- Hashimoto I., Rasera Y., Taruya A., 2017, *Phys. Rev. D*, 96, 043526
- Heavens A. F., Sellentin E., de Mijolla D., Vianello A., 2017, *MNRAS*, 472, 4244
- Hellwing W. A., Li B., Frenk C. S., Cole S., 2013, *Mon. Not. Roy. Astron. Soc.*, 435, 2806
- Hernández-Aguayo C., Hou J., Li B., Baugh C. M., Sánchez A. G., 2019, *Mon. Not. Roy. Astron. Soc.*, 485, 2194
- Hiramatsu T., 2022, *J. Cosmology Astropart. Phys.*, 2022, 035
- Hiramatsu T., Yamauchi D., 2020, *Phys. Rev. D*, 102, 083525
- Hirano S., Kobayashi T., Tashiro H., Yokoyama S., 2018, *Phys. Rev. D*, 97, 103517
- Hirano S., Kobayashi T., Yamauchi D., Yokoyama S., 2019a, *Phys. Rev. D*, 99, 104051
- Hirano S., Kobayashi T., Yamauchi D., 2019b, *Phys. Rev. D*, 99, 104073
- Hirano S., Kobayashi T., Yamauchi D., Yokoyama S., 2020, *Phys. Rev. D*, 102, 103505
- Hivon E., Bouchet F. R., Colombi S., Juszkiewicz R., 1995, *A&A*, 298, 643
- Hockney R. W., Eastwood J. W., 1981, *Computer Simulation Using Particles*
- Hoffmann K., Bel J., Gaztañaga E., Crocce M., Fosalba P., Castander F. J., 2015, *MNRAS*, 447, 1724
- Hoffmann K., Gaztañaga E., Scoccimarro R., Crocce M., 2018, *MNRAS*, 476, 814
- Horndeski G. W., 1974, *Int. J. Theor. Phys.*, 10, 363
- Hu W., Sawicki I., 2007, *Phys. Rev. D*, 76, 064004
- Ishak M., 2019, *Living Rev. Rel.*, 22, 1
- Ivanov M. M., Sibiryakov S., 2018, *JCAP*, 07, 053
- Ivanov M. M., Simonović M., Zaldarriaga M., 2020, *J. Cosmology Astropart. Phys.*, 2020, 042
- Ivanov M. M., Philcox O. H. E., Nishimichi T., Simonović M., Takada M., Zaldarriaga M., 2022, *Phys. Rev. D*, 105, 063512
- Ivanov M. M., Philcox O. H. E., Cabass G., Nishimichi T., Simonović M., Zaldarriaga M., 2023, *Phys. Rev. D*, 107, 083515
- Jain B., Bertschinger E., 1996, *Astrophys. J.*, 456, 43
- Jain R. K., Kouvaris C., Nielsen N. G., 2016, *Phys. Rev. Lett.*, 116, 151103
- Jing Y. P., 2005, *ApJ*, 620, 559
- Jing Y. P., Boerner G., 1997, *A&A*, 318, 667
- Jing Y. P., Börner G., 1998, *Astrophys. J.*, 503, 37
- Jing Y. P., Börner G., 2004, *ApJ*, 607, 140
- Jing Y.-P., Zhang J.-L., 1989, *ApJ*, 342, 639
- Jing Y. P., Mo H. J., Boerner G., 1991, *A&A*, 252, 449
- Jolicoeur S., Umeh O., Maartens R., Clarkson C., 2017, *J. Cosmology Astropart. Phys.*, 2017, 040
- Jolicoeur S., Umeh O., Maartens R., Clarkson C., 2018, *J. Cosmology Astropart. Phys.*, 2018, 036

- Kaiser N., 1987, *Mon. Not. Roy. Astron. Soc.*, 227, 1
- Kamalinejad F., Slepian Z., 2020, arXiv e-prints, p. [arXiv:2011.00899](https://arxiv.org/abs/2011.00899)
- Karagiannis D., Lazanu A., Liguori M., Raccanelli A., Bartolo N., Verde L., 2018, *MNRAS*, 478, 1341
- Karagiannis D., Maartens R., Randrianjanahary L. F., 2022, *J. Cosmology Astropart. Phys.*, 2022, 003
- Kase R., Tsujikawa S., 2019, *Int. J. Mod. Phys. D*, 28, 1942005
- Kase R., Tsujikawa S., 2020a, *JCAP*, 11, 032
- Kase R., Tsujikawa S., 2020b, *Phys. Rev. D*, 101, 063511
- Kayo I., et al., 2004, *PASJ*, 56, 415
- Kehagias A., Riotto A., 2013, *Nucl. Phys. B*, 873, 514
- Kimura R., Kobayashi T., Yamamoto K., 2012, *Phys. Rev. D*, 85, 024023
- Kimura R., Suyama T., Yamaguchi M., Yamauchi D., Yokoyama S., 2018, *Publ. Astron. Soc. Jap.*, 70, Publications of the Astronomical Society of Japan, Volume 70, Issue 5, 1 October 2018, L5, <https://doi.org/10.1093/pasj/psy083>
- Kitaura F.-S., et al., 2016, *Mon. Not. Roy. Astron. Soc.*, 456, 4156
- Klypin A., Yepes G., Gottlober S., Prada F., Hess S., 2016, *Mon. Not. Roy. Astron. Soc.*, 457, 4340
- Kobayashi T., 2019, *Rept. Prog. Phys.*, 82, 086901
- Kobayashi T., Yamaguchi M., Yokoyama J., 2011, *Prog. Theor. Phys.*, 126, 511
- Kobayashi T., Watanabe Y., Yamauchi D., 2015, *Phys. Rev. D*, 91, 064013
- Kobayashi Y., Nishimichi T., Takada M., Miyatake H., 2022, *Phys. Rev. D*, 105, 083517
- Koyama K., 2016, *Rept. Prog. Phys.*, 79, 046902
- Koyama K., Sakstein J., 2015, *Phys. Rev. D*, 91, 124066
- Koyama K., Taruya A., Hiramatsu T., 2009, *Phys. Rev. D*, 79, 123512
- Koyama K., Umeh O., Maartens R., Bertacca D., 2018, *JCAP*, 07, 050
- Kreisch C. D., Komatsu E., 2018, *JCAP*, 12, 030
- Kulkarni G. V., Nichol R. C., Sheth R. K., Seo H.-J., Eisenstein D. J., Gray A., 2007, *MNRAS*, 378, 1196
- Kuruwilla J., Porciani C., 2020, *J. Cosmology Astropart. Phys.*, 2020, 043
- Lange J. U., Hearin A. P., Leauthaud A., van den Bosch F. C., Guo H., DeRose J., 2022, *MNRAS*, 509, 1779
- Langlois D., 2017, in *52nd Rencontres de Moriond on Gravitation*, pp 221–228 ([arXiv:1707.03625](https://arxiv.org/abs/1707.03625))
- Langlois D., 2019, *Int. J. Mod. Phys. D*, 28, 1942006
- Langlois D., Noui K., 2016, *JCAP*, 02, 034
- Langlois D., Mancarella M., Noui K., Vernizzi F., 2017, *JCAP*, 05, 033
- Langlois D., Saito R., Yamauchi D., Noui K., 2018, *Phys. Rev. D*, 97, 061501
- Langlois D., Noui K., Roussille H., 2020, arXiv e-prints, p. [arXiv:2012.10218](https://arxiv.org/abs/2012.10218)
- Laureijs R., et al., 2011, arXiv e-prints, p. [arXiv:1110.3193](https://arxiv.org/abs/1110.3193)
- Lazanu A., Liguori M., 2018, *J. Cosmology Astropart. Phys.*, 2018, 055
- Lazanu A., Giannantonio T., Schmittfull M., Shellard E. P. S., 2016, *Phys. Rev. D*, 93, 083517
- Lazeyras T., Wagner C., Baldauf T., Schmidt F., 2016, *J. Cosmology Astropart. Phys.*, 2016, 018
- Levi M., Vlah Z., 2016, arXiv e-prints, p. [arXiv:1605.09417](https://arxiv.org/abs/1605.09417)
- Lewandowski M., 2020, *JCAP*, 08, 044
- Lewandowski M., Senatore L., 2017, *JCAP*, 08, 037
- Lewandowski M., Senatore L., 2020, *JCAP*, 03, 018
- Lewandowski M., Perko A., Senatore L., 2015, *JCAP*, 05, 019
- Liguori M., Sefusatti E., Fergusson J. R., Shellard E. P. S., 2010, *Advances in Astronomy*, 2010, 980523
- Linde A. D., 1982, *Phys. Lett.*, B108, 389
- Lombriser L., Lima N. A., 2017, *Phys. Lett. B*, 765, 382
- Lombriser L., Taylor A., 2016, *JCAP*, 03, 031
- Ma C.-P., Fry J. N., 2000, *ApJ*, 543, 503
- Maldacena J. M., 2003, *JHEP*, 05, 013
- Marín F., 2011, *Astrophys. J.*, 737, 97
- Marín F. A., Wechsler R. H., Frieman J. A., Nichol R. C., 2008, *ApJ*, 672, 849
- Marín F. A., et al., 2013, *Mon. Not. Roy. Astron. Soc.*, 432, 2654
- Martin J., 2012, *Comptes Rendus Physique*, 13, 566
- Matarrese S., Verde L., Heavens A. F., 1997, *Mon. Not. Roy. Astron. Soc.*, 290, 651
- Matsubara T., 2004, *ApJ*, 615, 573
- Matsubara T., 2008, *Phys. Rev.*, D77, 063530
- Mazumdar A., Bharadwaj S., Sarkar D., 2020, *MNRAS*, 498, 3975
- McBride C. K., Connolly A. J., Gardner J. P., Scranton R., Newman J. A., Scoccimarro R., Zehavi I., Schneider D. P., 2011a, *ApJ*, 726, 13
- McBride C. K., Connolly A. J., Gardner J. P., Scranton R., Scoccimarro R., Berlind A. A., Marín F., Schneider D. P., 2011b, *ApJ*, 739, 85
- McCullagh N., Jeong D., Szalay A. S., 2016, *MNRAS*, 455, 2945
- McDonald P., 2009, *JCAP*, 11, 026
- Melville S., Noller J., 2020, *Phys. Rev. D*, 101, 021502
- Moradinezhad Dizgah A., Biagetti M., Sefusatti E., Desjacques V., Noreña J., 2021, *J. Cosmology Astropart. Phys.*, 2021, 015
- Moresco M., et al., 2017b, *A&A*, 604, A133
- Moresco M., et al., 2017a, *Astron. Astrophys.*, 604, A133
- Moresco M., Veropalumbo A., Marulli F., Moscardini L., Cimatti A., 2021, *ApJ*, 919, 144
- Mueller E.-M., Percival W., Linder E., Alam S., Zhao G.-B., Sánchez A. G., Beutler F., Brinkmann J., 2018, *Mon. Not. Roy. Astron. Soc.*, 475, 2122
- Munshi D., McEwen J. D., 2020, *Mon. Not. Roy. Astron. Soc.*, 498, 5299
- Munshi D., Regan D., 2017, *J. Cosmology Astropart. Phys.*, 2017, 042
- Munshi D., McEwen J. D., Kitching T., Fosalba P., Teyssier R., Stadel J., 2020a, *JCAP*, 05, 043
- Munshi D., Namikawa T., Kitching T. D., McEwen J. D., Takahashi R., Bouchet F. R., Taruya A., Bose B., 2020b, *Mon. Not. Roy. Astron. Soc.*, 493, 3985
- Namikawa T., Bouchet F. R., Taruya A., 2018, *Phys. Rev. D*, 98, 043530
- Namikawa T., Bose B., Bouchet F. R., Takahashi R., Taruya A., 2019, *Phys. Rev. D*, 99, 063511
- Nan Y., Yamamoto K., Hikage C., 2018, *J. Cosmology Astropart. Phys.*, 2018, 038
- Narikawa T., Kobayashi T., Yamauchi D., Saito R., 2013, *Phys. Rev. D*, 87, 124006
- Nichol R. C., et al., 2006, *MNRAS*, 368, 1507
- Nishimichi T., Kayo I., Hikage C., Yahata K., Taruya A., Jing Y. P., Sheth R. K., Suto Y., 2007, *PASJ*, 59, 93
- Nojiri S., Odintsov S. D., 2011, *Phys. Rep.*, 505, 59
- Nojiri S., Odintsov S. D., Oikonomou V. K., 2017, *Phys. Rep.*, 692, 1
- Noller J., 2020, *Phys. Rev. D*, 101, 063524
- Noller J., Nicola A., 2019, *Phys. Rev. D*, 99, 103502
- Noller J., Nicola A., 2020, *Phys. Rev. D*, 102, 104045
- Oddo A., Sefusatti E., Porciani C., Monaco P., Sánchez A. G., 2020, *J. Cosmology Astropart. Phys.*, 2020, 056
- Oddo A., Rizzo F., Sefusatti E., Porciani C., Monaco P., 2021, *J. Cosmology Astropart. Phys.*, 2021, 038
- Okada H., Totani T., Tsujikawa S., 2013, *Phys. Rev. D*, 87, 103002
- Ostrogradsky M., 1850, *Mem. Acad. St. Petersburg*, 6, 385
- Pace F., Battye R. A., Bellini E., Lombriser L., Vernizzi F., Bolliet B., 2021, *J. Cosmology Astropart. Phys.*, 2021, 017
- Pan J., Szapudi I., 2005, *MNRAS*, 362, 1363
- Pan J., Coles P., Szapudi I., 2007, *MNRAS*, 382, 1460
- Pardede K., Rizzo F., Biagetti M., Castorina E., Sefusatti E., Monaco P., 2022, *J. Cosmology Astropart. Phys.*, 2022, 066
- Peacock J. A., Nicholson D., 1991, *MNRAS*, 253, 307
- Pearson D. W., Samushia L., 2018, *MNRAS*, 478, 4500
- Peebles P. J. E., 1975, *ApJ*, 196, 647
- Peebles P. J. E., 1980, The large-scale structure of the universe
- Peebles P. J. E., Groth E. J., 1975, *ApJ*, 196, 1
- Peebles P. J. E., Yu J. T., 1970, *Astrophys. J.*, 162, 815
- Peirone S., Benevento G., Frusciante N., Tsujikawa S., 2019, *Phys. Rev. D*, 100, 063509
- Peloso M., Pietroni M., 2013, *JCAP*, 05, 031
- Peloso M., Pietroni M., 2014, *JCAP*, 04, 011
- Percival W. J., White M., 2009, *Mon. Not. Roy. Astron. Soc.*, 393, 297
- Percival W. J., et al., 2014, *Mon. Not. Roy. Astron. Soc.*, 439, 2531
- Percival W. J., Friedrich O., Sellentin E., Heavens A., 2022, *MNRAS*, 510, 3207
- Peronon L., Bel J., Maartens R., de la Cruz-Dombriz A., 2019, *JCAP*, 06, 020
- Perlmutter S., et al., 1999, *Astrophys. J.*, 517, 565
- Philcox O. H. E., Ivanov M. M., 2022, *Phys. Rev. D*, 105, 043517

- Philcox O. H. E., Ivanov M. M., Cabass G., Simonović M., Zaldarriaga M., Nishimichi T., 2022, *Phys. Rev. D*, **106**, 043530
- Pollack J. E., Smith R. E., Porciani C., 2012, *MNRAS*, **420**, 3469
- Predehl P., et al., 2021, *A&A*, **647**, A1
- Rampf C., Wong Y. Y. Y., 2012, *J. Cosmology Astropart. Phys.*, **2012**, 018
- Raveri M., 2020, *Phys. Rev. D*, **101**, 083524
- Reid B., et al., 2016, *Mon. Not. Roy. Astron. Soc.*, **455**, 1553
- Riess A. G., et al., 1998, *Astron. J.*, **116**, 1009
- Rizzo F., Moretti C., Pardede K., Eggemeier A., Oddo A., Sefusatti E., Porciani C., Monaco P., 2023, *J. Cosmology Astropart. Phys.*, **2023**, 031
- Rodríguez-Torres S. A., et al., 2016, *MNRAS*, **460**, 1173
- Ross A. J., et al., 2012, *Mon. Not. Roy. Astron. Soc.*, **424**, 564
- Ruggeri R., Castorina E., Carbone C., Sefusatti E., 2018, *J. Cosmology Astropart. Phys.*, **2018**, 003
- Saito S., Takada M., Taruya A., 2009, *Phys. Rev. D*, **80**, 083528
- Saito S., Baldauf T., Vlah Z., Seljak U., Okumura T., McDonald P., 2014, *Phys. Rev. D*, **90**, 123522
- Saito R., Yamauchi D., Mizuno S., Gleyzes J., Langlois D., 2015, *JCAP*, **06**, 008
- Sakstein J., 2015a, *Phys. Rev. D*, **92**, 124045
- Sakstein J., 2015b, *Phys. Rev. Lett.*, **115**, 201101
- Sakstein J., Jain B., 2017, *Phys. Rev. Lett.*, **119**, 251303
- Sakstein J., Wilcox H., Bacon D., Koyama K., Nichol R. C., 2016, *JCAP*, **07**, 019
- Sakstein J., Kenna-Allison M., Koyama K., 2017a, *JCAP*, **03**, 007
- Sakstein J., Babichev E., Koyama K., Langlois D., Saito R., 2017b, *Phys. Rev. D*, **95**, 064013
- Saltas I. D., Christensen-Dalsgaard J., 2022, *A&A*, **667**, A115
- Saltas I. D., Lopes I., 2019, *Phys. Rev. Lett.*, **123**, 091103
- Saltas I. D., Sawicki I., Lopes I., 2018, *JCAP*, **05**, 028
- Salzano V., Mota D. F., Capozziello S., Donahue M., 2017, *Phys. Rev. D*, **95**, 044038
- Samushia L., Slepian Z., Villaescusa-Navarro F., 2021, *MNRAS*, **505**, 628
- Sato K., 1981, *Mon. Not. Roy. Astron. Soc.*, **195**, 467
- Schmittfull M., Baldauf T., Seljak U., 2015, *Phys. Rev. D*, **91**, 043530
- Scoccimarro R., 1997, *Astrophys. J.*, **487**, 1
- Scoccimarro R., 2000, *ApJ*, **544**, 597
- Scoccimarro R., 2015, *Phys. Rev. D*, **92**, 083532
- Scoccimarro R., Couchman H. M. P., 2001, *MNRAS*, **325**, 1312
- Scoccimarro R., Frieman J., 1996, *Astrophys. J. Suppl.*, **105**, 37
- Scoccimarro R., Frieman J. A., 1999, *ApJ*, **520**, 35
- Scoccimarro R., Colombi S., Fry J. N., Frieman J. A., Hivon E., Melott A., 1998, *Astrophys. J.*, **496**, 586
- Scoccimarro R., Couchman H. M. P., Frieman J. A., 1999, *Astrophys. J.*, **517**, 531
- Scoccimarro R., Feldman H. A., Fry J. N., Frieman J. A., 2001a, *Astrophys. J.*, **546**, 652
- Scoccimarro R., Sheth R. K., Hui L., Jain B., 2001b, *ApJ*, **546**, 20
- Scoccimarro R., Sefusatti E., Zaldarriaga M., 2004, *Phys. Rev. D*, **69**, 103513
- Scoccimarro R., Hui L., Manera M., Chan K. C., 2012, *Phys. Rev. D*, **85**, 083002
- Sebastiani L., Vagnozzi S., Myrzakulov R., 2017, *Adv. High Energy Phys.*, **2017**, 3156915
- Sefusatti E., 2009, *Phys. Rev. D*, **80**, 123002
- Sefusatti E., Komatsu E., 2007, *Phys. Rev. D*, **76**, 083004
- Sefusatti E., Crocce M., Pueblas S., Scoccimarro R., 2006, *Phys. Rev. D*, **74**, 023522
- Sefusatti E., Crocce M., Desjacques V., 2010, *MNRAS*, **406**, 1014
- Sefusatti E., Crocce M., Desjacques V., 2012, *MNRAS*, **425**, 2903
- Sellentin E., Heavens A. F., 2016, *MNRAS*, **456**, L132
- Senatore L., Trevisan G., 2018, *JCAP*, **05**, 019
- Senatore L., Zaldarriaga M., 2015, *JCAP*, **02**, 013
- Sharp N. A., Bonometto S. A., Lucchin F., 1984, *A&A*, **130**, 79
- Sherwin B. D., Zaldarriaga M., 2012, *Phys. Rev. D*, **85**, 103523
- Shirasaki M., Sugiyama N. S., Takahashi R., Kitaura F.-S., 2021, *Phys. Rev. D*, **103**, 023506
- Slepian Z., Eisenstein D. J., 2015, *MNRAS*, **454**, 4142
- Slepian Z., Eisenstein D. J., 2016, *MNRAS*, **455**, L31
- Slepian Z., Eisenstein D. J., 2017, *Mon. Not. Roy. Astron. Soc.*, **469**, 2059
- Slepian Z., Eisenstein D. J., 2018, *MNRAS*, **478**, 1468
- Slepian Z., et al., 2017a, *MNRAS*, **468**, 1070
- Slepian Z., et al., 2017b, *Mon. Not. Roy. Astron. Soc.*, **469**, 1738
- Slepian Z., et al., 2018, *Mon. Not. Roy. Astron. Soc.*, **474**, 2109
- Smee S. A., et al., 2013, *AJ*, **146**, 32
- Smith J. A., et al., 2002, *Astron. J.*, **123**, 2121
- Smith R. E., Sheth R. K., Scoccimarro R., 2008, *Phys. Rev. D*, **78**, 023523
- Song Y.-S., Percival W. J., 2009, *JCAP*, **10**, 004
- Song Y.-S., et al., 2015a, *Phys. Rev. D*, **92**, 043522
- Song Y.-S., Taruya A., Oka A., 2015b, *J. Cosmology Astropart. Phys.*, **2015**, 007
- Sotiriou T. P., Faraoni V., 2010, *Rev. Mod. Phys.*, **82**, 451
- Springel V., 2005, *MNRAS*, **364**, 1105
- Starobinsky A. A., 1980, *Phys. Lett.*, **B91**, 99
- Sugiyama N. S., Futamase T., 2013, *Astrophys. J.*, **769**, 106
- Sugiyama N. S., Spergel D. N., 2014, *JCAP*, **02**, 042
- Sugiyama N. S., Shiraishi M., Okumura T., 2018, *MNRAS*, **473**, 2737
- Sugiyama N. S., Saito S., Beutler F., Seo H.-J., 2019, *MNRAS*, **484**, 364
- Sugiyama N. S., Saito S., Beutler F., Seo H.-J., 2020, *MNRAS*, **497**, 1684
- Sugiyama N. S., Saito S., Beutler F., Seo H.-J., 2021, *Mon. Not. Roy. Astron. Soc.*, **501**, 2862
- Sunyaev R. A., Zeldovich Y. B., 1970, *Astrophys. Space Sci.*, **7**, 3
- Szapudi I., Postman M., Lauer T. R., Oegerle W., 2001, *ApJ*, **548**, 114
- Takada M., Hu W., 2013, *Phys. Rev. D*, **87**, 123504
- Takada M., Jain B., 2003, *MNRAS*, **340**, 580
- Takada M., et al., 2014, *Publ. Astron. Soc. Jap.*, **66**, R1
- Takahashi R., Nishimichi T., Namikawa T., Taruya A., Kayo I., Osato K., Kobayashi Y., Shirasaki M., 2020, *ApJ*, **895**, 113
- Takushima Y., Terukina A., Yamamoto K., 2014, *Phys. Rev. D*, **89**, 104007
- Takushima Y., Terukina A., Yamamoto K., 2015, *Phys. Rev. D*, **92**, 104033
- Taruya A., 2016, *Phys. Rev. D*, **94**, 023504
- Taruya A., Nishimichi T., Saito S., 2010, *Phys. Rev. D*, **82**, 063522
- Taruya A., Saito S., Nishimichi T., 2011, *Phys. Rev. D*, **83**, 103527
- Taruya A., Koyama K., Hiramatsu T., Oka A., 2014a, *Phys. Rev. D*, **89**, 043509
- Taruya A., Nishimichi T., Bernardeau F., Hiramatsu T., Koyama K., 2014b, *Phys. Rev. D*, **90**, 123515
- Taylor A., Joachimi B., 2014, *Mon. Not. Roy. Astron. Soc.*, **442**, 2728
- Taylor A., Joachimi B., Kitching T., 2013, *Mon. Not. Roy. Astron. Soc.*, **432**, 1928
- Tellarini M., Ross A. J., Tasinato G., Wands D., 2015, *J. Cosmology Astropart. Phys.*, **2015**, 004
- Tellarini M., Ross A. J., Tasinato G., Wands D., 2016, *J. Cosmology Astropart. Phys.*, **2016**, 014
- Toth G., Hollosi J., Szalay A. S., 1989, *ApJ*, **344**, 75
- Tram T., Fidler C., Crittenden R., Koyama K., Pettinari G. W., Wands D., 2016, *JCAP*, **05**, 058
- Traykova D., Bellini E., Ferreira P. G., 2019, *JCAP*, **08**, 035
- Tsedrik M., Moretti C., Carrilho P., Rizzo F., Pourtsidou A., 2023, *MNRAS*, **520**, 2611
- Tselikhovich D., Hirata C., 2010, *Phys. Rev. D*, **82**, 083520
- Umeh O., Koyama K., Maartens R., Schmidt F., Clarkson C., 2019, *JCAP*, **05**, 020
- Valageas P., Taruya A., Nishimichi T., 2017, *Phys. Rev. D*, **95**, 023504
- Valogiannis G., Bean R., 2019, *Phys. Rev. D*, **99**, 063526
- Valogiannis G., Bean R., Aviles A., 2020, *JCAP*, **01**, 055
- Verde L., Heavens A. F., Matarrese S., Moscardini L., 1998, *Mon. Not. Roy. Astron. Soc.*, **300**, 747
- Verde L., Wang L., Heavens A. F., Kamionkowski M., 2000, *MNRAS*, **313**, 141
- Verde L., et al., 2002, *MNRAS*, **335**, 432
- Wang Y., Yang X., Mo H. J., van den Bosch F. C., Chu Y., 2004, *MNRAS*, **353**, 287
- Weinberg S., 1989, *Rev. Mod. Phys.*, **61**, 1
- Welling Y., van der Woude D., Pajer E., 2016, *J. Cosmology Astropart. Phys.*, **2016**, 044



- Wilson M. J., Peacock J. A., Taylor A. N., de la Torre S., 2017, *MNRAS*, **464**, 3121
- Woodard R. P., 2015, *Scholarpedia*, **10**, 32243
- Yamamoto K., Nan Y., Hikage C., 2017, *Phys. Rev. D*, **95**, 043528
- Yamauchi D., Sugiyama N. S., 2022, *Phys. Rev. D*, **105**, 063515
- Yamauchi D., Yokoyama S., Takahashi K., 2017a, *Phys. Rev. D*, **95**, 063530
- Yamauchi D., Yokoyama S., Tashiro H., 2017b, *Phys. Rev. D*, **96**, 123516
- Yankelevich V., Porciani C., 2019, *MNRAS*, **483**, 2078
- Yoo J., Seljak U., 2013, *Phys. Rev. D*, **88**, 103520
- Yoo J., Dalal N., Seljak U., 2011, *JCAP*, **07**, 018
- Yoshikawa K., Tanaka S., Yoshida N., Saito S., 2020, *ApJ*, **904**, 159
- Yuan S., Garrison L. H., Eisenstein D. J., Wechsler R. H., 2022, *MNRAS*, **515**, 871
- Zel'Dovich Y. B., 1970, *A&A*, **500**, 13
- Zumalacárregui M., García-Bellido J., 2014, *Phys. Rev. D*, **89**, 064046
- d'Amico G., Gleyzes J., Kokron N., Markovic K., Senatore L., Zhang P., Beutler F., Gil-Marín H., 2020, *J. Cosmology Astropart. Phys.*, **2020**, 005
- de Carvalho E., Bernui A., Xavier H. S., Novaes C. P., 2020, *MNRAS*, **492**, 4469
- de Rham C., Matas A., 2016, *JCAP*, **06**, 041
- de Rham C., Melville S., 2018, *Phys. Rev. Lett.*, **121**, 221101
- de Weerd E. M., Clarkson C., Jolicœur S., Maartens R., Umeh O., 2020, *J. Cosmology Astropart. Phys.*, **2020**, 018

## APPENDIX A: HITOMI

In order to improve the reproducibility of the results of this paper, we publish the complete set of program codes we used under the name HITOMI. The languages used in it are `C++` and `PYTHON`. Users can download the source files from the following link: <https://github.com/naonori/hitomi.git>. In particular, to reproduce the results of this paper, refer to the DEMO section of the linked page. There, it explains how to measure the 2PCF and 3PCF from the BOSS DR12 data, compute the theoretical model including the window function correction, compute the covariance matrix from the Patchy mocks, combine them to perform the Fisher and MCMC analyses, and finally summarise the obtained results in figures and tables. To illustrate these things, we recorded a video of us running the program and uploaded it to YouTube. The text editor used for this is vim.

HITOMI requires several external programs such as `MONTEPYTHON` (Brinckmann & Lesgourgues 2019), `CLASS` (Blas et al. 2011), `CUBA` (Hahn 2005), `GSL`<sup>14</sup>, `FFTW` (Frigo & Johnson 2005), and `FFTLG` (Hamilton 2000). We have written a script with the code to install the external programs needed to run HITOMI on the Cray XC50 at the Center for Computational Astrophysics of the National Astronomical Observatory of Japan. A video recording of the use of this script is available at the following link: <https://www.youtube.com/watch?v=v1P7XIXZsUM>. Of course, users of other PC clusters will have to install HITOMI according to their environment. Nevertheless, our installation instructions will be helpful to users as a demonstration.

HITOMI not only reproduces the results of this paper but also offers various options. For example, it can measure both the power spectrum and the bispectrum. HITOMI also provides the codes to simplify the 3PCF and bispectrum measurements for simulations with periodic boundary conditions with a global line-of-sight direction. It is also possible to measure the 2PCF and 3PCF (power spectrum and bispectrum) after the reconstruction of the galaxy distribution and compute the corresponding reconstructed models (Eisenstein et al.

2007b; Shirasaki et al. 2021). Although not yet implemented, in the future, we plan to release a code to compute the bispectrum covariance matrix of galaxies based on perturbation theory, as was done by Sugiyama et al. (2020). We also plan to release a code that performs an anisotropic BAO analysis using the anisotropic 3PCF, as in Sugiyama et al. (2021).

It is possible to modify parts of the HITOMI code, e.g., the theoretical calculation of the 3PCF, to investigate how the results propagate to the final parameter constraint results. It is also possible to replace the BOSS DR12 galaxy data with data from other galaxies or galaxy clusters, e.g. PFS (Takada et al. 2014), DESI (DESI Collaboration et al. 2016), Euclid (Laureijs et al. 2011), SPHEREx (Doré et al. 2014), CMB-S4 (Carlstrom et al. 2019), and eROSITA (Predehl et al. 2021), to perform data analysis of the 3PCF or bispectrum.

This paper has been typeset from a  $\text{\TeX}/\text{\LaTeX}$  file prepared by the author.

<sup>14</sup> <http://www.gnu.org/software/gsl/>